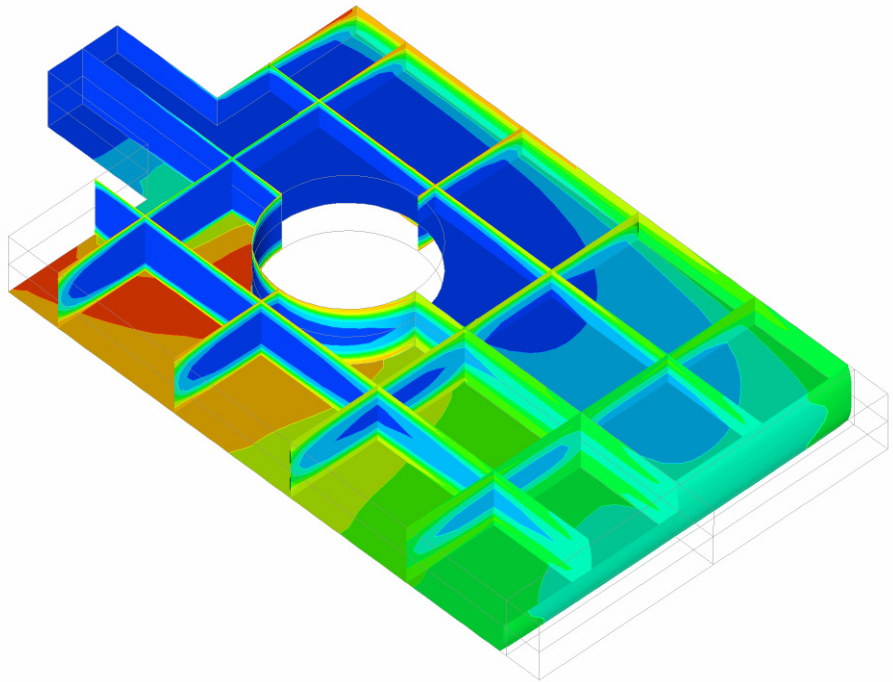




Rui Alexandre  
Aires da Trindade  
Igreja

**Numerical Simulation of the Filling and Curing  
Stages in Reaction Injection Moulding, using CFX**

**Simulação Numérica das Fases de Enchimento e  
Cura em *Reaction Injection Moulding*, usando o CFX**



This page was intentionally left blank



**Rui Alexandre  
Aires da Trindade  
Igreja**

**Numerical Simulation of the Filling and Curing  
Stages in Reaction Injection Moulding, using CFX**

**Simulação Numérica das Fases de Enchimento e  
Cura em *Reaction Injection Moulding*, usando o CFX**

Dissertação apresentada à Universidade de Aveiro para cumprimento dos requisitos necessários à obtenção do grau de Mestre em Engenharia Mecânica, realizada sob a orientação científica do Doutor Vítor António Ferreira da Costa, Professor Associado do Departamento de Engenharia Mecânica da Universidade de Aveiro

O trabalho conducente a esta dissertação foi realizado no âmbito do Projecto de Investigação POCTI/EMÉ/39247/2001, financiado pela Fundação para a Ciência e Tecnologia e co-financiado pelo FEDER.

## **o júri**

presidente

**Doutor Antonio Carlos Mendes de Sousa**

professor catedrático do Departamento de Engenharia Mecânica da Universidade de Aveiro

**Doutor António Manuel Gameiro Lopes**

professor auxiliar da Faculdade de Ciências e Tecnologia da Universidade de Coimbra

**Doutor Vítor António Ferreira da Costa**

professor associado do Departamento de Engenharia Mecânica da Universidade de Aveiro

**palavras-chave**

*Reaction Injection Moulding* (RIM), Enchimento de Moldes, Simulação Numérica, Escoamentos Bifásicos, (ANSYS) CFX.

**resumo**

Os métodos habitualmente utilizados para a simulação de injeção em moldes envolvem um número considerável de simplificações, originando reduções significativas do esforço computacional mas, nalguns casos também limitações. Neste trabalho são efectuadas simulações de *Reaction Injection Moulding* (RIM) com o mínimo de simplificações, através da utilização do software de CFD multi-objectivos CFX, concebido para a simulação numérica de escoamentos e transferência de calor e massa.

Verifica-se que o modelo homogéneo para escoamentos multifásicos do CFX, geralmente considerado o apropriado para a modelação de escoamentos de superfície livre em que as fases estão completamente estratificadas, é incapaz de modelar correctamente o processo de enchimento. Este problema é ultrapassado através da implementação do modelo não homogéneo juntamente com a condição de fronteira de escorregamento livre para o ar.

A reacção de cura é implementada no código como uma equação de transporte para uma variável escalar adicional, com um termo fonte. São testados vários esquemas transitórios e advectivos, com vista ao reconhecimento de quais os que produzem os resultados mais precisos.

Finalmente, as equações de conservação de massa, quantidade de movimento, cura e energia são implementadas conjuntamente para simular os processos simultâneos de enchimento e cura presentes no processo RIM. Os resultados numéricos obtidos reproduzem com boa fidelidade outros resultados numéricos e experimentais disponíveis, sendo necessários no entanto tempos de computação consideravelmente longos para efectuar as simulações.

**keywords**

Reaction Injection Moulding (RIM), Mould Filling, Numerical Simulation, Two-Phase Flow, (ANSYS) CFX.

**abstract**

Commonly used methods for injection moulding simulation involve a considerable number of simplifications, leading to a significant reduction of the computational effort but, in some cases also to limitations. In this work, Reaction Injection Moulding (RIM) simulations are performed with a minimum of simplifications, by using the general purpose CFD software package CFX, designed for numerical simulation of fluid flow and heat and mass transfer.

The CFX's homogeneous multiphase flow model, which is generally considered to be the appropriate choice for modelling free surface flows where the phases are completely stratified and the interface is well defined, is shown to be unable to model the filling process correctly. This problem is overcome through the implementation of the inhomogeneous model in combination with the free-slip boundary condition for the air phase.

The cure reaction is implemented in the code as a transport equation for an additional scalar variable, with a source term. Various transient and advection schemes are tested to determine which ones produce the most accurate results.

Finally, the mass conservation, momentum, cure and energy equations are implemented all together to simulate the simultaneous filling and curing processes present in the RIM process. The obtained numerical results show a good global accuracy when compared with other available numerical and experimental results, though considerably long computation times are required to perform the simulations.

# Table of contents

---

**Resumo**

**Abstract**

**Table of contents** i

**Nomenclature** iii

**1 Introduction** 1

1.1 Overview of the RIM process 1

1.2 Literature review 4

1.2.1 Injection moulding 4

1.2.2 Reaction Injection Moulding 5

1.3 The 2½D Hele-Shaw flow approach 6

1.4 Motivation and objectives 8

**2 Simulation of the filling process** 11

2.1 The homogeneous model 11

2.1.1 Physical model 11

2.1.2 Numerical model 12

2.1.3 Case study 16

2.2 The inhomogeneous model 28

2.2.1 Physical model 28

2.2.2 Numerical model 31

2.2.3 Case study 33

2.3 Conclusions 41

<b>3 Simulation of the curing process</b>	43
3.1 The cure reaction	43
3.2 Physical model	44
3.3 Numerical models	44
3.4 Case study	46
3.5 Conclusions	51
<b>4 Simulation of the RIM filling and curing stages</b>	53
4.1 The energy equation	53
4.1.1 Physical model	53
4.1.2 Numerical model	54
4.2 Case study 1	55
4.2.1 Case description	55
4.2.2 Numerical issues	57
4.2.3 Results	61
4.3 Case study 2	73
4.3.1 Case description and numerical issues	73
4.3.2 Results	75
4.4 Case studies 3 and 4	80
4.4.1 Cases description	80
4.4.2 Numerical issues	81
4.4.3 Results	83
4.5 Conclusions	91
<b>5 Conclusions</b>	93
<b>References</b>	99



# Nomenclature

---

## Symbols:

A	Area	[m <sup>2</sup> ]
A	Constant in the viscosity equation	[-]
A <sub>αβ</sub>	Interfacial area per unit volume	[m <sup>-1</sup> ]
A <sub>μ</sub>	Pre-exponential factor in the viscosity equation	[kg/(m·s)]
A <sub>1</sub>	Pre-exponential factor in the cure equation	[s <sup>-1</sup> ]
A <sub>2</sub>	Pre-exponential factor in the cure equation	[s <sup>-1</sup> ]
B	Constant in the viscosity equation	[-]
cs	Control volume	
cs	Surface of the control volume	
C	Degree of cure	[-]
C <sub>D</sub>	Drag coefficient	[-]
C <sub>g</sub>	Solidification (gel) point	[-]
C <sub>p</sub>	Specific heat at constant pressure	[J/(kg·K)]
Cr	Courant number	[-]
C <sub>v</sub>	Specific heat at constant volume	[J/(kg·K)]
d <sub>αβ</sub>	Interface length scale	[m]
D <sub>h</sub>	Hydraulic diameter	[m]
e	Specific internal energy	[J/kg]
E <sub>μ</sub>	Viscosity activation energy	[J/mol]
E <sub>1</sub>	Reaction activation energy	[J/mol]
E <sub>2</sub>	Reaction activation energy	[J/mol]
f	Face	
F	Force	[N]
$\vec{F}_g$	Gravity force vector	[N]
F <sub>w</sub>	Wall shear force	[N]

$\vec{g}$	Gravity acceleration vector	[m/s <sup>2</sup> ]
h	Mould half thickness	[m]
h	Specific enthalpy	[J/kg]
htot	Specific total enthalpy	[J/kg]
H	Mould thickness	[m]
k	Thermal conductivity	[W/(m·K)]
k <sub>1</sub>	Parameter in the cure equation	[s <sup>-1</sup> ]
k <sub>2</sub>	Parameter in the cure equation	[s <sup>-1</sup> ]
L	Mould length	[m]
L <sub>f</sub>	Position of the flow front	[m]
m	Constant in the cure reaction	[-]
m	Mass	[kg]
$\dot{m}$	Mass flow	[kg/s]
$\overline{M_{\alpha\beta}}$	Volumetric interface momentum transfer	[N/m <sup>3</sup> ]
n	Constant in the cure reaction	[-]
$\vec{n}$	Outward normal surface vector	[-]
N	Shape function	
P, p	Pressure	[Pa]
P	Perimeter	[m]
Q	Volumetric flow rate	[m <sup>3</sup> /s]
$\dot{Q}_R$	Volumetric heat generation rate	[W/m <sup>3</sup> ]
Q <sub>t</sub>	Total volumetric heat of reaction	[J/m <sup>3</sup> ]
r	Volume fraction	[-]
R	Universal gas constant	[J/(mol·K)]
$\vec{R}$	Vector from the upwind node to ip	[m]
Re	Reynolds number	[-]
S	Cross section	
S	Fluidity	[m·s]
S	Surface	

$S_C$	Rate of cure	$[s^{-1}]$
$S_{Cp}$	Linear source coefficient in the cure equation	$[s^{-1}]$
$S_{Cv}$	Source value in the cure equation	$[s^{-1}]$
$S_E$	Volumetric heat source	$[W/m^3]$
$S_{Ep}$	Linear source coefficient in the energy equation	$[W/(m^3 \cdot K)]$
$S_{Ev}$	Source value in the energy equation	$[W/m^3]$
$\overline{S_M}$	Volumetric momentum source	$[N/m^3]$
$t$	Time	$[s]$
$t_f$	Filling time	$[s]$
$t_R$	Time of residence	$[s]$
$T$	Period	$[s]$
$T$	Temperature	$[K]$
$T_i$	Initial temperature	$[K]$
$u$	Velocity x component	$[m/s]$
$\overline{U}$	Velocity vector	$[m/s]$
$v$	Velocity y component	$[m/s]$
$V$	Volume	$[m^3]$
$w$	Velocity z component	$[m/s]$
$W$	Mould width	$[m]$
$W_v$	Volumetric viscous work rate	$[W/m^3]$
$x$	x direction	$[m]$
$y$	y direction	$[m]$
$z$	z direction	$[m]$

**Greek symbols:**

$\beta$	Blend factor for the advection term discretization	$[-]$
$\gamma$	Shear rate	$[s^{-1}]$
$\delta$	Identity matrix	

$\Delta t$	Time step	[s]
$\Delta T_{ad}$	Adiabatic temperature rise	[K]
$\Delta x$	Length of the mesh elements	[m]
$\theta$	Quotient between the old and the new time step	[-]
$\mu$	Viscosity	[kg/(m·s)]
$\rho$	Density	[kg/m <sup>3</sup> ]
$\tau_w$	Wall shear stress	[N/m <sup>2</sup> ]
$\phi$	General variable	

**Subscripts:**

air	Air
in	Inlet
ip	Integration point
max	Maximum value
n	Node
out	Outlet
ref	Reference
resin	Resin
up	Upwind node
w	Wall
x	x component of the vector
y	y component of the vector
z	z component of the vector
$\alpha$	Phase $\alpha$
$\beta$	Phase $\beta$

**Superscripts:**

CFX	Results from CFX
hom	Homogeneous model
inhom	Inhomogeneous model
0	Old time level
00	Time before the old time level

**Operators:**

•	Inner product
⊗	Tensor product
∇	Nabla vector
$X^T$	Transpose of $X$

**Others:**

$\overline{X}$	Average value of $X$
----------------	----------------------



# 1 Introduction

---

## 1.1 Overview of the RIM process

The application of synthetic polymeric materials, which are nowadays commonly used in all of the major market sectors, experienced a dramatic expansion in the second half of the 20<sup>th</sup> century. Due to the continuous progress made in polymeric engineering, these materials can be synthesized to meet a wide range of mechanical, chemical, optical and electrical properties. Their low density, resulting in a relatively high specific strength and stiffness, their aptitude to be manufactured into complex shaped parts and, more important, their ability to be integrated in automatic mass production processes, which together with the relatively low cost of raw material, lead to the low cost of the final product, make these materials very attractive, specially from an economical point of view.

Amongst the various polymer processing techniques, injection moulding is certainly one of the most important, representing approximately one third of all manufactured polymeric parts [1, 2]. Extrusion represents approximately another third (32% and 36% of weight, respectively [1]).

Synthetic polymers can be classified in two major categories: thermoplastic polymers and thermosetting polymers. For thermoplastics, by far the largest volume (about 80% of the raw material used in injection moulding [3]), the long molecules are not chemically joined, and thus they can be melted by heating (typically 200-350 °C [3]), solidified by cooling and remelted repeatedly. Thermosets are initially made of short chain molecules, and upon heating or mixing with appropriate reagents, they undergo an irreversible chemical reaction which causes the short chain molecules to bond. This process leads to the formation of a rigid three-dimensional structure, which once formed will not remelt by heating [2, 4].

In Thermoplastics Injection Moulding (TIM), the hot polymer melt is pushed at high pressure into a cold cavity where it undergoes solidification by cooling down below the glass transition temperature. Although this process is extensively used for non-specific and undemanding applications, it presents some weaknesses which limit its use for more technical parts. Thermoplastics usually have lower mechanical properties than thermosetting polymers. Their relatively high viscosity (usually exceeding 100 kg/(m·s) [2]) requires high injection pressures (typically 50-200 MPa [3]), limiting the dimensions of parts to typically 1 m<sup>2</sup>. High viscosity also limits the use of reinforcements, which are necessary to meet more demanding requirements, and the production of parts with complex

shapes. In order to overcome these limitations, reactive moulding techniques have been developed for thermosetting polymers [2].

Reactive moulding is quite different from conventional TIM, since it uses polymerization in the mould, instead of cooling, to form the stiff solid parts.

Reaction Injection Moulding (RIM) is a process for rapid production of complex parts through the mixing and chemical reaction of two or more components. The liquid components, usually isocyanate and polyol, held in separated temperature controlled tanks, feed to metering units. When injection begins, the valves open and the components flow at moderate to high pressures, typically between 10 and 20 MPa, into a mixing chamber. The streams are intensively mixed by high velocity impingement and due to the shape of the mixing chamber, and the mixture begins to polymerize, or cure, as it flows into the mould cavity. As the mixture is initially at low viscosity, low pressures, less than 1 MPa, are needed to fill the mould, typically in less than five seconds. Inside the mould, cure occurs, forming the polymer, solidifying and building up enough stiffness and strength such that the mould can be opened and the part removed, often in less than one minute. Postcuring may be necessary [5, 6]. Fig. 1 [7] shows the diagram of a typical RIM process.

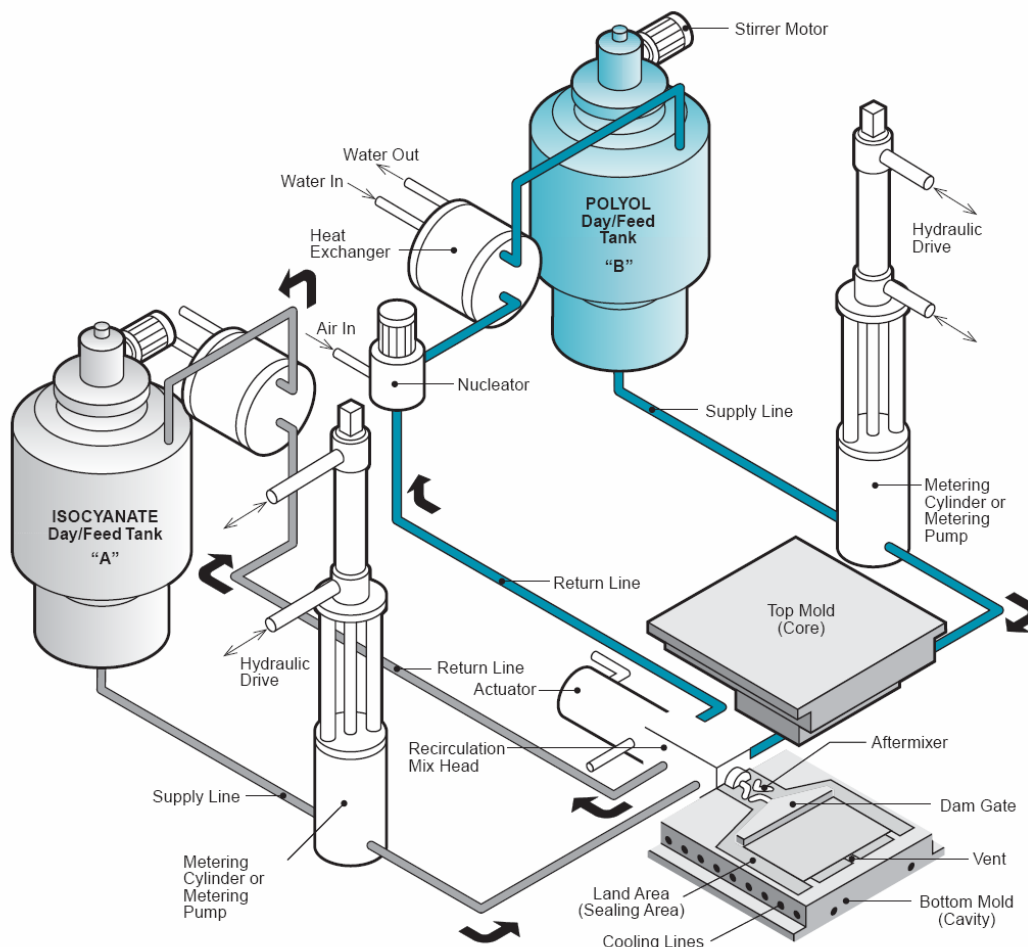


Fig. 1: Diagram of a typical RIM process [7].



During RIM's early years, its main use was for high density rigid polyurethane foam parts for the automotive industry, such as bumpers and fascia. Over the years it has developed uses in many different areas. The end use applications for RIM are nowadays so varied that polyurethane can be found in forms such as protective coatings, flexible foams, rigid foams and elastomers. Although polyurethanes comprise the majority in RIM processing, other types of chemical systems can be processed, for instance polyureas, nylons, dicyclopentadienes, polyesters, epoxies, acrylics and hybrid urethane systems [8].

Due to the low viscosity RIM liquids, ranging from 0.1 to 1 kg/(m·s), large parts can be manufactured with relatively small metering machines, complex shapes, with multiple inserts, can be fabricated and low pressures can be used to fill the moulds, and these may be constructed from light-weight materials often at lower costs than for TIM. Mould clamping forces are much lower, requiring lower cost presses. This opens up short production runs, and even prototype applications [5]. Low viscosity also opens options in reinforcement as Structural Reaction Injection Moulding (SRIM), and Reinforced Reaction Injection Moulding (RRIM) [8].

RIM temperatures are typically lower than those for TIM, with less energy demands [5]. However, handling of reactive, and often hazardous liquids, requires special equipments and procedures. As some components freeze at room temperature, a temperature controlled environment is required for their shipping and storage, increasing the costs. Due to the low viscosity, it is difficult to seal moulds, increasing leakage and flash. As low viscosity liquids penetrate mould surfaces, there is the need for release agents, which has been a major problem for high RIM production.

If flow into the mould is too rapid, air may be entrained and large bubbles appear in the final part, which is perhaps the greatest cause of scrap. Also, due to low pressure during filling, it is difficult to remove air from pockets formed behind inserts and from corners. Thus, vent location becomes extremely important. Some of these problems can be prevented if moulds are filled slowly, but this can lead to short shots.

As asserted by [9], "Successful moulders must use RIM long enough to learn all the peculiarities of chemical manipulation, mould manufacture, and processing parameters. These typically differ for each project, resulting in a long learning curve for the few companies that choose to offer RIM-produced products". This is why a better understanding of the injection and curing processes is important. Numerical simulations of these processes may be helpful to choose the chemical components, to design the mould, its position and vents location, and to design the process itself: shot time and inlet and mould temperatures.

## 1.2 Literature review

### 1.2.1 Injection moulding

As mentioned in [3] and [10], the first attempts to study the filling stage in injection moulding were reported by Spencer and Gilmore [11]. They visually studied the filling of the mould and derived an empirical equation to determine the filling time. Other important early flow visualization and tracer studies include the contributions from [12] and [13].

Numerical simulations applied to injection moulding have basically started in the early 1970s. According to [2] and [14], these first developments were applied to the filling stage in simple geometries [15–23]. Only tubular, circular and rectangular shapes were considered, allowing the flow to be accurately assumed as unidirectional. The temperature field was two-dimensional, one coordinate in the flow direction and the other in the thickness direction, leading to the so-called 1½D approach. The injected polymer was assumed to be a Newtonian fluid, and finite difference techniques were used to numerically solve the set of balance equations.

In [15], one-dimensional flow analysis was coupled with a heat balance equation for a rectangular cavity. The work presented in [16, 17] dealt with the filling of a disc mould, using the assumption of a radial creeping flow, and [21] modelled one-dimensional tubular flow of polymer melts.

In order to expand the previous approaches to more realistic geometries, conformal mapping [24–26] or decomposition of complex shape cavities in a number of simple elements [27, 28] were used to extend the 1½D approach to more complex flow situations. However, these methods lack sufficient generality to be satisfactory and the solution accuracy strongly depends on how the geometry is partitioned, requiring astute judgment from the user.

The real breakthrough came with the development of a general 2½D approach, originally proposed in [29], combining finite elements along the midsurface of the cavity with finite differences along the thickness direction. The pressure field was solved in two dimensions by finite element method and the temperature and velocity fields were solved in three dimensions by means of a mixed finite element / finite difference method.

However, based on the Hele-Shaw approximation, the 2½D approach was unable to represent the complex flow kinematics of the flow front region, the so-called fountain flow, see Fig. 2 [30], first reported in [31]. The description of this phenomenon was addressed by many authors by means of experimental [32–36], analytical [37–39] and numerical [33, 40–45] methods, leading to approximate models able to capture its basic flow kinematics without resolving the complex 3D flow details.

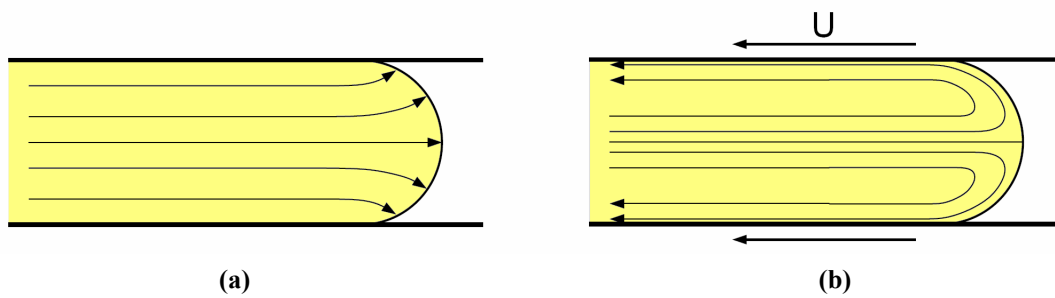


**Fig. 2: Kinematics of fountain flow.**

**(a) Reference frame of mould; (b) Reference frame of the moving flow front. [30]**

Different techniques have been used to handle the time-dependency of the flow domain during filling. One solution consisted in the use of the control volume method [46–48], while alternative solutions included the use of boundary fitted coordinates [49, 50] or the use of a front tracking and remeshing techniques [51–53].

To date several commercial and research three-dimensional simulation programs for injection moulding have been developed. In particular, [54] developed a three-dimensional finite-element code for predicting the velocity and pressure fields governed by the generalized Navier-Stokes equations, [55] analysed the three-dimensional mould filling of an incompressible fluid and the shape of the fountain flow front, [56, 57] incorporated the polymer compressibility, by treating its density as a function of temperature and pressure, in a three-dimensional mould filling process.

### 1.2.2 Reaction Injection Moulding

As both thermoplastics and reaction injection moulding are basically governed by the same flow kinematics, most of the developments made in the simulation of the filling stage of thermoplastics are applicable to reaction injection moulding.

Early studies were dedicated to the static analysis of heat transfer and cure, on the assumption that the curing stage could be decoupled from the filling stage [58, 59]. More realistic models were obtained by extending the 1½D approach to reaction injection moulding [39, 60–66]. The work of Castro and Macosko [39], presenting experimental and numerical results was of particular importance, it was considered by many authors as a benchmark solution (it is used also in this work, in Section 4.2 and Section 4.3, as a benchmark solution).

Extensions to the 2½D approach were only reported more recently [2, 67–71], and 3D simulations have already been reported in some works [72–76].

### 1.3 The 2½D Hele-Shaw flow approach

Despite many commercial codes' ability to perform 3D injection moulding simulations, the 2½-dimensional Hele-Shaw approach remains the standard numerical framework for simulation of injection moulding. Therefore, it becomes important to succinctly describe its assumptions and formulation, and to discuss its advantages and limitations relatively to a full three-dimensional approach.

Injection moulding is generally characterized by the part thickness being much smaller than its overall dimensions and by the high viscosity of the polymer (the latter is not entirely valid for RIM resins), resulting in low ratios of the inertia force to the viscous forces (characterized by low Reynolds numbers). In the Hele-Shaw flow formulation, the inertia effect and the velocity component and thermal convection in the gap-wise direction are neglected. Moreover, due to small thickness of the part, the velocity gradient in the gap-wise direction is considered to be much larger than in the other directions. Thus, denoting the planar coordinates by  $x$  and  $y$ , the gap-wise coordinate by  $z$ , and the velocity components by  $u$ ,  $v$  and  $w$ , respectively, the continuity and momentum equations are reduced to [77, 78]:

$$\frac{\partial \rho}{\partial t} + \frac{\partial(\rho \cdot u)}{\partial x} + \frac{\partial(\rho \cdot v)}{\partial y} = 0 \quad (1)$$

$$-\frac{\partial p}{\partial x} + \frac{\partial}{\partial z} \left( \mu \cdot \frac{\partial u}{\partial z} \right) = 0 \quad (2)$$

$$-\frac{\partial p}{\partial y} + \frac{\partial}{\partial z} \left( \mu \cdot \frac{\partial v}{\partial z} \right) = 0 \quad (3)$$

The boundary conditions for  $u$  and  $v$  are [77]:

$$u = v = 0 \quad \text{at } z = \pm h \quad (\text{on mold wall}) \quad (4)$$

$$\frac{\partial u}{\partial z} = \frac{\partial v}{\partial z} = 0 \quad \text{at } z = 0 \quad (\text{on middle plane}) \quad (5)$$

As the pressure is independent of the  $z$  direction, by integrating twice equations (2) and (3), and taking into account the boundary conditions, one arrives to:

$$u = -\frac{\partial p}{\partial x} \cdot \int_z^h \frac{z}{\mu} dz \quad (6)$$

$$v = -\frac{\partial p}{\partial y} \cdot \int_z^h \frac{z}{\mu} dz \quad (7)$$

By integrating equation (1) between  $z = 0$  and  $z = h$ , the continuity and momentum equations are merged into a single Poisson-like equation in terms of pressure and fluidity [14, 77]:

$$\frac{\partial}{\partial t} \left( \int_0^h \rho \, dz \right) - \frac{\partial}{\partial x} \left( S \cdot \frac{\partial p}{\partial x} \right) - \frac{\partial}{\partial y} \left( S \cdot \frac{\partial p}{\partial y} \right) = 0 \quad (8)$$

where  $S$  is the fluidity, expressed as [77]:

$$S = \int_0^h \rho \cdot \frac{z^2}{\mu} \, dz \quad (9)$$

The two above equations could be even further simplified if assuming constant polymer density.

The gap-wise direction averaged velocities may be obtained as:

$$\bar{u} = -\frac{\partial p}{\partial x} \cdot \frac{\int_0^h \frac{z^2}{\mu} \, dz}{h} \quad (10)$$

$$\bar{v} = -\frac{\partial p}{\partial y} \cdot \frac{\int_0^h \frac{z^2}{\mu} \, dz}{h} \quad (11)$$

Besides the velocity and heat convection in the gap-wise direction being omitted, the heat conduction in the flow directions is assumed to be negligible when compared with that in the gap-wise direction [14, 78]. The energy equation is then simplified to [77]:

$$\rho \cdot C_p \cdot \left( \frac{\partial T}{\partial t} + u \cdot \frac{\partial T}{\partial x} + v \cdot \frac{\partial T}{\partial y} \right) = \frac{\partial}{\partial z} \left( k \cdot \frac{\partial T}{\partial z} \right) + \mu \cdot \dot{\gamma}^2 + \dot{Q}_R \quad (12)$$

The term  $(\mu \cdot \dot{\gamma}^2)$  represents the heat generated by viscous dissipation, and  $\dot{Q}_R$  the rate of heat generation due to chemical reaction.  $\dot{\gamma}$  is the shear rate, which, according to the assumptions mentioned above, is expressed as [79]:

$$\dot{\gamma} = \sqrt{\left( \frac{\partial u}{\partial z} \right)^2 + \left( \frac{\partial v}{\partial z} \right)^2} \quad (13)$$

or:

$$\dot{\gamma} = \frac{z}{\mu} \cdot \sqrt{\left( \frac{\partial p}{\partial x} \right)^2 + \left( \frac{\partial p}{\partial y} \right)^2} \quad (14)$$

However, for typical RIM situations, the viscous dissipation term in the energy equation can be neglected when compared to the heat generation term due to the cure reaction [39, 80].

Equations (8) and (12) for pressure and temperature, are the basic equations of the Hele-Shaw approximation for mould filling in thin cavities [78]. Equation (8) is commonly solved by the finite-element method and equation (12) by the finite-difference method [14].

Due to the Hele-Shaw formulation assumptions and simplifications mentioned above, the usage of computational storage and CPU time can be considerably reduced when compared with the case of a full three-dimensional (unsteady) formulation. But, although its successful applications to the injection moulding process, it has its limitations mostly owing to those assumptions [14].

The inertia and three-dimensional effects may become significant enough to influence the flow, especially in complex thick parts, in situations of branching flow, where the part thickness changes abruptly, or in regions around special features such as bosses, corners and ribs. For the RIM process, because of resins small viscosities, the fluid inertia and the gravity force cannot be omitted [14].

At the filling front, the fluid moves away from the centre, spilling out like a fountain to the walls [5] (thus the designation “fountain flow”), and therefore the flow is as important in the transverse as in the planar directions. Simple fountain flow approximations have been implemented with the Hele-Shaw formulation. However, in view of its importance in RIM, since it determines the path and the location of each reactive fluid element during filling, a three-dimensional formulation is expected to provide more detailed and accurate information [14].

## **1.4 Motivation and objectives**

The core objective of this work is to assess the potential of the commercial general-purpose CFD software, CFX-5 (recently renamed ANSYS CFX), a fully implicit, unstructured, node centred, finite-volume based code, to simulate the complete three-dimensional behaviour of the RIM simultaneous filling and curing processes.

Because of the inherent RIM process and parts characteristics, such as resins’ low viscosities, common complex geometries possibly with the presence of inserts, together with the importance to accurately determine the flow behaviour at the flow front region, a full 3D approach seems to be much more valuable, relatively to the 2½D approach, than in simulations of the TIM process.

Despite the existence of commercial injection moulding software packages able to perform 3D mould filling analysis, the 2½D approach, as previously mentioned, is still the standard analysis in injection moulding simulations and, extremely little has been made regarding the simulation of this important kind of industrial process making use of general-purpose CFD software packages.

Although three-dimensional simulations for injection moulding are still notorious for their excessive computation time requirements, as computer performances increase they are anticipated to increase in the near future [14]. It is reported in [81] that in 2003 the same CFD problem could be run over 100 times faster than in 1996 (7 years before), a factor of 30 due to increase in processors speed (double every 18 months, as stated by the modern and most popular formulation of the Moore's law [82]), and the remaining due to enhancements in numerical methods and faster solver algorithms. Additionally, the possibility to run calculations on a network of PCs, something unavailable not too long ago, and improvements in parallel computing algorithms, will tend towards faster time solutions to many CFD problems [81] at relatively low hardware costs.

Commercial multi-purpose CFD software packages are usually cheaper than commercial specialized injection moulding packages, and are able to perform numerical simulations of many other varieties of processes, making them a much more versatile and valuable tool than the specialized packages usual in injection moulding.





## 2 Simulation of the filling process

---

### 2.1 The homogeneous model

#### 2.1.1 Physical model

The process of an enclosed volume being filled with a fluid  $A$  and displacing the original fluid  $B$ , usually air, is common in engineering practice. The filling of a mould is an example of it. This process on its own, even not considering the energy and the chemical reaction, is complex, as it is a transient two-phase free surface flow.

For this type of flows, where the phases are completely stratified and the interface is well defined, it makes sense to assume that both phases share a single velocity field [83]. Thus, choosing the homogeneous model of CFX, the flow is described by [83]:  
the equation of conservation of total mass:

$$\frac{\partial \rho}{\partial t} + \nabla \cdot (\rho \cdot \vec{U}) = 0 \quad (15)$$

the momentum equations:

x direction:

$$\begin{aligned} & \frac{\partial(\rho \cdot u)}{\partial t} + \frac{\partial(\rho \cdot u^2)}{\partial x} + \frac{\partial(\rho \cdot u \cdot v)}{\partial y} + \frac{\partial(\rho \cdot u \cdot w)}{\partial z} = \\ & -\frac{\partial p}{\partial x} + \frac{\partial}{\partial x} \left( 2\mu \cdot \frac{\partial u}{\partial x} \right) + \frac{\partial}{\partial y} \left[ \mu \cdot \left( \frac{\partial u}{\partial y} + \frac{\partial v}{\partial x} \right) \right] + \frac{\partial}{\partial z} \left[ \mu \cdot \left( \frac{\partial u}{\partial z} + \frac{\partial w}{\partial x} \right) \right] + S_{M_x} \end{aligned} \quad (16)$$

y direction:

$$\begin{aligned} & \frac{\partial(\rho \cdot v)}{\partial t} + \frac{\partial(\rho \cdot u \cdot v)}{\partial x} + \frac{\partial(\rho \cdot v^2)}{\partial y} + \frac{\partial(\rho \cdot v \cdot w)}{\partial z} = \\ & -\frac{\partial p}{\partial y} + \frac{\partial}{\partial x} \left[ \mu \cdot \left( \frac{\partial v}{\partial x} + \frac{\partial u}{\partial y} \right) \right] + \frac{\partial}{\partial y} \left( 2\mu \cdot \frac{\partial v}{\partial y} \right) + \frac{\partial}{\partial z} \left[ \mu \cdot \left( \frac{\partial v}{\partial z} + \frac{\partial w}{\partial y} \right) \right] + S_{M_y} \end{aligned} \quad (17)$$

z direction:

$$\begin{aligned} & \frac{\partial(\rho \cdot w)}{\partial t} + \frac{\partial(\rho \cdot u \cdot w)}{\partial x} + \frac{\partial(\rho \cdot v \cdot w)}{\partial y} + \frac{\partial(\rho \cdot w^2)}{\partial z} = \\ & -\frac{\partial p}{\partial z} + \frac{\partial}{\partial x} \left[ \mu \cdot \left( \frac{\partial w}{\partial x} + \frac{\partial u}{\partial z} \right) \right] + \frac{\partial}{\partial y} \left[ \mu \cdot \left( \frac{\partial w}{\partial y} + \frac{\partial v}{\partial z} \right) \right] + \frac{\partial}{\partial z} \left( 2\mu \cdot \frac{\partial w}{\partial z} \right) + S_{M_z} \end{aligned} \quad (18)$$

or, in general vector form:

$$\frac{\partial(\rho \cdot \bar{U})}{\partial t} + \nabla \bullet (\rho \cdot \bar{U} \otimes \bar{U}) = \nabla \bullet \left[ -p \cdot \delta + \mu \cdot \left( \nabla \otimes \bar{U} + (\nabla \otimes \bar{U})^T \right) \right] + \bar{S}_M \quad (19)$$

the conservation of mass of phase  $\alpha$ :

$$\frac{\partial(r_\alpha \cdot \rho_\alpha)}{\partial t} + \nabla \bullet (r_\alpha \cdot \rho_\alpha \cdot \bar{U}) = 0 \quad (20)$$

and the constraint that the two phases completely fill up the available volume:

$$r_\alpha + r_\beta = 1 \quad (21)$$

Therefore, the flow is characterized by 6 equations (5 of them partial differential equations) and 6 unknowns ( $p$ ,  $u$ ,  $v$ ,  $w$ ,  $r_\alpha$  and  $r_\beta$ ).

In these equations,  $\rho$  and  $\mu$  are the volume fraction weighted mixture density and viscosity evaluated as [83]:

$$\rho = \rho_\alpha \cdot r_\alpha + \rho_\beta \cdot r_\beta \quad (22)$$

$$\mu = \mu_\alpha \cdot r_\alpha + \mu_\beta \cdot r_\beta \quad (23)$$

$\bar{S}_M$  represents the source of momentum due to internal forces, the gravity in this case, and is given by [83]:

$$\bar{S}_M = (\rho - \rho_{\text{ref}}) \cdot \vec{g} \quad (24)$$

where  $\rho_{\text{ref}}$  is the reference density.

### 2.1.2 Numerical model

CFX is based on the Finite Volume Method (FVM), and each node in the mesh is at the centre of a finite control volume, Fig. 3.

The partial differential equations are integrated over all the control volumes, using Gauss' Divergence Theorem to convert volume integrals on to surface integrals:

$$\int_V \nabla \cdot \phi \, dV = \int_S \vec{n} \cdot \phi \, dS \quad (25)$$

where  $\vec{n}$  represents the outward normal surface vector.

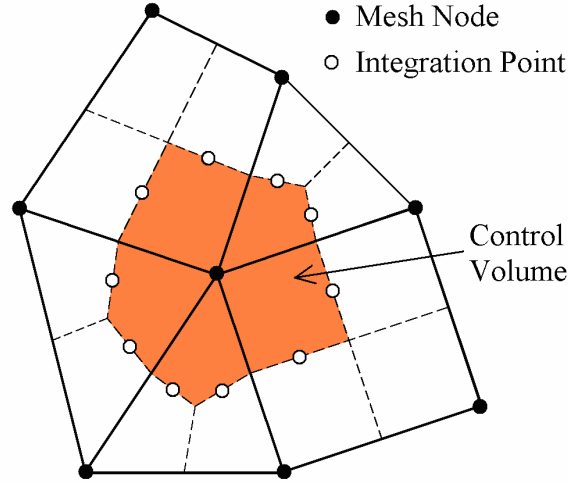


Fig. 3: Representation of the control volume associated with each mesh node.

As the control volume surface is composed by a series of surface segments, or faces, the surface integrals can be transformed into a sum of integrals over the faces [84]:

$$\int_S \vec{n} \cdot \phi \, dS = \sum_f \left( \int_f \vec{n} \cdot \phi \, dS \right) \quad (26)$$

These face integrals are then discretely represented at integration points, located at the centre of each face:

$$\sum_f \left( \int_f \vec{n} \cdot \phi \, dS \right) \approx \sum_{ip} \left( \vec{n}_{ip} \cdot A_{ip} \cdot \phi_{ip} \right) \quad (27)$$

$A_{ip}$  being the area of the face associated with the integration point.

According to this, the discrete forms of the governing equations are [83]:  
the equation of conservation of total mass:

$$\frac{\partial}{\partial t} \left( \int_V \rho \, dV \right) + \sum_{ip} \left( \rho \cdot \vec{U} \cdot \vec{n} \cdot A \right)_{ip} = 0 \quad (28)$$

the momentum equations:

x direction:

$$\begin{aligned} \frac{\partial}{\partial t} \left( \int_V \rho \cdot u \, dV \right) + \sum_{ip} \dot{m}_{ip} \cdot u_{ip} = & - \sum_{ip} (n_x \cdot A \cdot p)_{ip} + \\ & \sum_{ip} \left\{ \mu \cdot \left[ 2 \cdot \frac{\partial u}{\partial x} \cdot n_x + \left( \frac{\partial u}{\partial y} + \frac{\partial v}{\partial x} \right) \cdot n_y + \left( \frac{\partial u}{\partial z} + \frac{\partial w}{\partial x} \right) \cdot n_z \right] \cdot A \right\}_{ip} + \overline{S_{M_x}} \cdot V \end{aligned} \quad (29)$$

y direction:

$$\begin{aligned} \frac{\partial}{\partial t} \left( \int_V \rho \cdot v \, dV \right) + \sum_{ip} \dot{m}_{ip} \cdot v_{ip} = - \sum_{ip} (n_y \cdot A \cdot p)_{ip} + \\ \sum_{ip} \left\{ \mu \cdot \left[ \left( \frac{\partial v}{\partial x} + \frac{\partial u}{\partial y} \right) \cdot n_x + 2 \cdot \frac{\partial v}{\partial y} \cdot n_y + \left( \frac{\partial v}{\partial z} + \frac{\partial w}{\partial y} \right) \cdot n_z \right] \cdot A \right\}_{ip} + \overline{S_{M_y}} \cdot V \end{aligned} \quad (30)$$

z direction:

$$\begin{aligned} \frac{\partial}{\partial t} \left( \int_V \rho \cdot w \, dV \right) + \sum_{ip} \dot{m}_{ip} \cdot w_{ip} = - \sum_{ip} (n_z \cdot A \cdot p)_{ip} + \\ \sum_{ip} \left\{ \mu \cdot \left[ \left( \frac{\partial w}{\partial x} + \frac{\partial u}{\partial z} \right) \cdot n_x + \left( \frac{\partial w}{\partial y} + \frac{\partial v}{\partial z} \right) \cdot n_y + 2 \cdot \frac{\partial w}{\partial z} \cdot n_z \right] \cdot A \right\}_{ip} + \overline{S_{M_z}} \cdot V \end{aligned} \quad (31)$$

and the mass conservation equation of phase  $\alpha$  [85]:

$$\frac{\partial}{\partial t} \left( \int_V \rho_\alpha \cdot r_\alpha \, dV \right) + \sum_{ip} (r_\alpha \cdot \rho_\alpha \cdot \overline{U} \cdot \vec{n} \cdot A)_{ip} = 0 \quad (32)$$

$\dot{m}_{ip}$  being the discrete mass flow rate through a face of the finite volume, obtained from the preceding iteration as [86]:

$$\dot{m}_{ip} = (\rho \cdot \overline{U} \cdot \vec{n} \cdot A)_{ip} \quad (33)$$

$n_x$ ,  $n_y$  and  $n_z$  are the Cartesian components of the outward normal surface vector, and  $V$  the volume of the control volume.

Choosing the second order backward Euler scheme, the transient term on the equation of conservation of total mass (28) is approximated as [87]:

$$\frac{\partial}{\partial t} \left( \int_V \rho \, dV \right) \approx \frac{V}{\Delta t} \cdot \left\{ \frac{1}{\theta \cdot (1+\theta)} \cdot \left[ (2+\theta) \cdot \theta \cdot \rho - (1+\theta)^2 \cdot \rho^0 + \rho^{00} \right] \right\} \quad (34)$$

and, on the momentum equations (29), (30) and (31) as:

$$\begin{aligned} \frac{\partial}{\partial t} \left( \int_V \rho \cdot U_i \, dV \right) \approx \\ \frac{V}{\Delta t} \cdot \left\{ \frac{1}{\theta \cdot (1+\theta)} \cdot \left[ (2+\theta) \cdot \theta \cdot \rho \cdot U_i - (1+\theta)^2 \cdot \rho^0 \cdot U_i^0 + \rho^{00} \cdot U_i^{00} \right] \right\} \end{aligned} \quad (35)$$

where  $U_i$  represents the  $i$  component of the velocity vector,  $^0$  denotes the old time level,  $^{00}$  the time before the old time level, and  $\theta$  is the quotient between the old and the new time step:

$$\theta = \frac{\Delta t^0}{\Delta t} = \frac{t^0 - t^{00}}{t - t^0} \quad (36)$$

At this point, the values of the variables and of the derivatives at the integration points must be obtained from the values of the variables stored at the mesh nodes. The value of the pressure  $p$  at ip is evaluated using finite element shape functions (linear in terms of parametric coordinates) [83]:

$$p_{ip} = \sum_n \left[ (N_n)_{ip} \cdot p_n \right] \quad (37)$$

where  $N_n$  is the shape function for node  $n$ , and  $p_n$  the value of  $p$  at the node  $n$ . For the diffusion terms, the derivatives at the integration points are also evaluated making use of shape functions. For example, the derivative of  $\phi$  in the  $x$  direction at ip is obtained as [83]:

$$\left( \frac{\partial \phi}{\partial x} \right)_{ip} = \sum_n \left[ \left( \frac{\partial N_n}{\partial x} \right)_{ip} \cdot \phi_n \right] \quad (38)$$

On the advection terms, a variable  $\phi$  at the integration points is obtained as:

$$\phi_{ip} = \phi_{up} + \beta \cdot (\nabla \phi \cdot \bar{\mathbf{R}}) \quad (39)$$

where  $\phi_{up}$  is the value of  $\phi$  at the upwind node,  $\nabla \phi$  is the upwind gradient of  $\phi$ ,  $\bar{\mathbf{R}}$  is the position vector from the upwind node to ip, and  $\beta$  is a blend factor. Different values of  $\beta$  produce different advection schemes. If  $\beta = 0$  the scheme is a first order Upwind Differencing Scheme (UDS), if  $\beta = 1$ , the scheme is a Second Order Upwind (SOU) biased scheme. Here, the advection scheme chosen for the total mass and momentum equations is based on that of [88], the high resolution scheme, where  $\beta$  is variable and locally computed to be as close as possible to 1 without violating boundedness principles.

However, for free surface applications, this scheme still causes too much numerical diffusion to the volume fraction equation. Instead, in order to keep the interface sharp, and as the order of accuracy is not the most important when the solutions are inherently discontinuous, when the “free surface flow” option is selected, CFX uses a compressive differencing scheme for the advection term of the volume fraction equation. This is made allowing  $\beta > 1$ , but reducing it as much as necessary to still maintain boundedness [85]. A

compressive transient scheme is also used for the transient term in the volume fraction equation.

### 2.1.3 Case study

A simple test case, the filling of a space between two parallel plates with a resin with constant density and viscosity, as shown in Fig. 4, was simulated. The width of the plates is considered to be infinite, so a two-dimensional approach is performed.

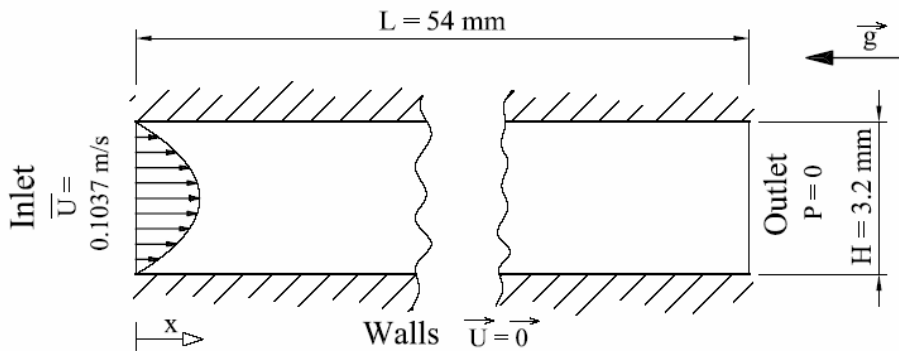


Fig. 4: Geometry of the simulated test case.

As CFX does not have a 2D solver, a three-dimensional simulation, with an one-element-thick mesh and symmetry boundary conditions imposed on the “front” and “back” faces, has to be performed. This applies whenever a two-dimensional simulation is mentioned in this work.

The properties of the filling fluid were chosen to be similar to those of the common RIM resins: density  $1000 \text{ kg/m}^3$  and viscosity  $0.05 \text{ kg/(m}\cdot\text{s)}$ . The space between the plates is initially filled with air, whose density and viscosity, taken as constant, are  $1.185 \text{ kg/m}^3$  and  $1.831 \times 10^{-5} \text{ kg/m}\cdot\text{s}$ , respectively.

The imposed boundary conditions are: a parabolic velocity profile with an average velocity of  $0.1037 \text{ m/s}$  at the inlet, pressure equal to zero at the outlet, and the condition of no slip on the walls. The values for the inlet average velocity and for the thickness  $H$  were chosen to be the same used for the mould modelled in Section 4.2.

The Reynolds number may be obtained as:

$$\text{Re} = \frac{\rho \cdot \bar{U} \cdot D_h}{\mu} \quad (40)$$

where  $D_h$  is the hydraulic diameter defined as [89]:

$$D_h = \frac{4 \cdot A}{P} \quad (41)$$

which, for a rectangular cross section with infinite width  $W$ , takes the value:

$$D_h = \frac{4 \cdot W \cdot H}{2 \cdot (W + H)}, \quad D_h \underset{W \rightarrow \infty}{=} 2 \cdot H \quad (42)$$

Thus, the Reynolds number is approximately 13 for the resin and 43 for the air. The flow is therefore unquestionably laminar, and the parabolic velocity profile imposed at the inlet boundary makes sense as a fully developed laminar flow. The velocity profile of the air at the outlet boundary is also expected to be parabolic.

Considering the control volume surrounded by the dashed line represented in Fig. 5:

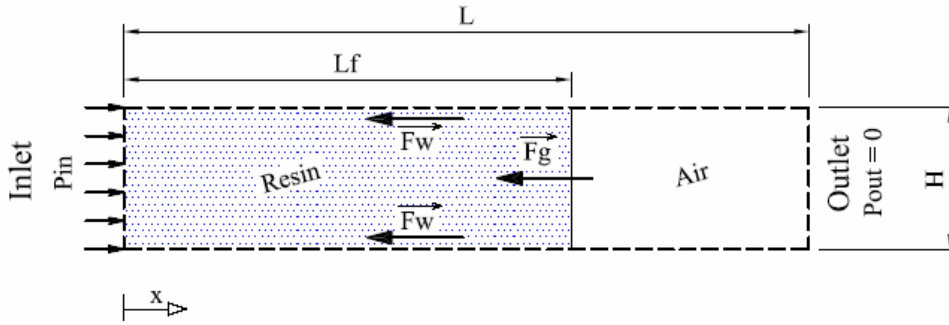


Fig. 5: Representation of the control volume and forces.

and applying the Newton's Second Law of motion in the  $x$  direction and an integral balance, one obtains [89]:

$$\sum F_x = \frac{d}{dt}(m \cdot u) = \frac{d}{dt} \left( \iiint_{cv} u \cdot \rho \, dV \right) + \iint_{cs} u \cdot \rho \cdot (\vec{U} \cdot \vec{n}) \, dA \quad (43)$$

where  $cv$  designates the control volume and  $cs$  its surface.

Being the velocity on the walls zero, and assuming that the velocity profile at the outlet is parabolic due to the flow being laminar, as at the inlet, the second term on the right side of equation (43) reduces to:

$$\begin{aligned} \iint_{cs} u \cdot \rho \cdot (\vec{U} \cdot \vec{n}) \, dA &= \iint_{outlet} \rho \cdot u^2 \, dA - \iint_{inlet} \rho \cdot u^2 \, dA \\ &= -\frac{6}{5} \cdot \bar{U}^2 \cdot H \cdot W \cdot (\rho_{resin} - \rho_{air}) \end{aligned} \quad (44)$$

where  $W$  indicates the width of the control volume.

Assuming a flat flow front, the density is constant on each cross section. Thus, the first term on the right side of equation (43) may be rewritten as:

$$\frac{d}{dt} \left( \iiint_{cv} \mathbf{u} \cdot \rho \, dV \right) = \frac{d}{dt} \left[ \int_0^L \rho \cdot \left( \iint_S \mathbf{u} \, dA \right) dx \right] \quad (45)$$

where S indicates a cross section. But, because of conservation of mass, and as the fluids are considered incompressible, the volume flow rate is constant:

$$\iint_S \mathbf{u} \, dA = \bar{U}_{in} \cdot A_{in} = \bar{U} \cdot H \cdot W \quad (\text{constant}) \quad (46)$$

Then, equation (45) may be simplified as:

$$\frac{d}{dt} \left( \iiint_{cv} \mathbf{u} \cdot \rho \, dV \right) = H \cdot W \cdot \frac{d}{dt} \left\{ \bar{U} \cdot [Lf \cdot \rho_{resin} + (L - Lf) \cdot \rho_{air}] \right\} \quad (47)$$

As the plates are parallel and therefore the cross section area is constant, the position of the flow front, Lf, may be obtained by integrating the inlet velocity over the time:

$$Lf = \int_0^t \bar{U} \, dt \quad (48)$$

leading finally to:

$$\begin{aligned} \frac{d}{dt} \left( \iiint_{cv} \mathbf{u} \cdot \rho \, dV \right) = H \cdot W \cdot \left\{ \frac{d\bar{U}}{dt} \cdot [Lf \cdot (\rho_{resin} - \rho_{air}) + L \cdot \rho_{air}] \right. \\ \left. + \bar{U}^2 \cdot (\rho_{resin} - \rho_{air}) \right\} \end{aligned} \quad (49)$$

If the inlet velocity is constant, the derivative on the right side of the above equation is zero, and the sum of forces is therefore:

$$\sum F_x = P_{in} \cdot A_{in} - \underbrace{P_{out}}_{=0} \cdot A_{out} - F_g - F_w = -\frac{1}{5} \cdot \bar{U}^2 \cdot H \cdot W \cdot (\rho_{resin} - \rho_{air}) \quad (50)$$

The gravity force, F<sub>g</sub>, is achieved by integrating (ρ·g) over the control volume, which considering again that the density is constant on each cross section, and that the cross section area is constant and equal to H·W, leads to:



$$F_g = \iiint_{cv} \rho \cdot g \, dV = g \cdot H \cdot W \cdot \int_0^L \rho \, dx = g \cdot H \cdot W \cdot [L_f \cdot (\rho_{resin} - \rho_{air}) + L \cdot \rho_{air}] \quad (51)$$

The wall shear stress is obtained, for Newtonian fluids, as:

$$\tau_w = \left[ \mu \cdot \frac{du}{dy} \right]_{@wall} \quad (52)$$

which, for a laminar flow with parabolic velocity profile may be reworked as:

$$\tau_w = \frac{6 \cdot \mu \cdot \bar{U}}{H} \quad (53)$$

and the walls shear force,  $F_w$ , is obtained by integrating  $\tau_w$  over the walls:

$$\begin{aligned} F_w &= \iint_{walls} \tau_w \, dA = 2 \times \int_0^L \frac{6 \cdot \mu \cdot \bar{U}}{H} \cdot W \, dx = \frac{12 \cdot \bar{U} \cdot H \cdot W}{H^2} \cdot \int_0^L \mu \, dx \\ &= \frac{12 \cdot \bar{U} \cdot H \cdot W}{H^2} \cdot [L_f \cdot (\mu_{resin} - \mu_{air}) + L \cdot \mu_{air}] \end{aligned} \quad (54)$$

Note that, due to the fountain flow, the velocity profile at the flow front region is not parabolic, and therefore there is an error on the above expression for  $F_w$ . However, as the flow front region is small compared with the total length  $L$ , this error may be neglected.

Finally, inserting the expressions of equations (51) and (54) into equation (50), the inlet pressure,  $P_{in}$ , is obtained as:

$$\begin{aligned} P_{in} &= g \cdot [L_f \cdot (\rho_{resin} - \rho_{air}) + L \cdot \rho_{air}] \\ &+ \frac{12 \cdot \bar{U}}{H^2} \cdot [L_f \cdot (\mu_{resin} - \mu_{air}) + L \cdot \mu_{air}] - \frac{1}{5} \cdot \bar{U}^2 \cdot (\rho_{resin} - \rho_{air}) \end{aligned} \quad (55)$$

On this last equation, the density and viscosity of the air could be fairly neglected, as they are considerably smaller than those of the resin:  $\rho_{air}/\rho_{resin} \cong 0.12\%$  and  $\mu_{air}/\mu_{resin} \cong 0.04\%$ .

$$P_{in} \cong g \cdot L_f \cdot \rho_{resin} + \frac{12 \cdot \bar{U}}{H^2} \cdot L_f \cdot \mu_{resin} - \frac{1}{5} \cdot \bar{U}^2 \cdot \rho_{resin} \quad (56)$$

The errors caused by this simplification would be, for  $L_f = 0.1L$ , 1 % on the first term of the right side of the equation, 0.3 % on the second term and 0.12 % on the last term. For  $L_f = 0.5L$ , the errors would be 0.12 %, 0.04 % and 0.12 %, respectively.

On the CFX model, the buoyancy reference density,  $\rho_{ref}$ , was set to the air density. This is interpreted as a momentum source on equation (19) equal to:

$$\overline{S}_M = \bar{g} \cdot (\rho - \rho_{\text{ref}}) = \bar{g} \cdot (\rho - \rho_{\text{air}}) \quad (57)$$

which means that the air hydrostatic pressure effect is omitted. Consequently, to obtain the inlet pressure according to the CFX homogeneous model,  $P_{\text{in}}^{\text{hom}}$ , the term  $L \cdot \rho_{\text{air}}$  shall be withdrawn from the first term of the right side of equation (55):

$$P_{\text{in}}^{\text{hom}} = g \cdot Lf \cdot (\rho_{\text{resin}} - \rho_{\text{air}}) + \frac{12 \cdot \bar{U}}{H^2} \cdot [Lf \cdot (\mu_{\text{resin}} - \mu_{\text{air}}) + L \cdot \mu_{\text{air}}] - \frac{1}{5} \cdot \bar{U}^2 \cdot (\rho_{\text{resin}} - \rho_{\text{air}}) \quad (58)$$

This causes an error of 1.2 % on the first term of the right side of this last equation, for  $Lf = 0.1L$ , and 0.24 % for  $Lf = 0.5L$ . The last term on equations (55) and (58) corresponds only to 2.1 Pa.

To calculate the value of the pressure at each position  $x$ , the velocity profile is considered to be parabolic at each cross section, which is valid for the whole domain except at the vicinity of the flow front. The same previous analysis is performed, except that this time the control volume is considered to comprise only the region between a cross section at the position  $x$  and the outlet. Thus the pressure depends on  $x$  as:

$$P(x) = \begin{cases} g \cdot [(Lf - x) \cdot \rho_{\text{resin}} + (L - Lf) \cdot \rho_{\text{air}}] + \frac{12 \cdot \bar{U}}{H^2} \cdot [(Lf - x) \cdot \mu_{\text{resin}} + (L - Lf) \cdot \mu_{\text{air}}] & (\text{for } x < Lf) \\ -\frac{1}{5} \cdot \bar{U}^2 \cdot (\rho_{\text{resin}} - \rho_{\text{air}}) & \\ g \cdot (L - x) \cdot \rho_{\text{air}} + \frac{12 \cdot \bar{U}}{H^2} \cdot (L - x) \cdot \mu_{\text{air}} & (\text{for } x > Lf) \end{cases} \quad (59)$$

and the pressure according to the CFX homogeneous model as:

$$P^{\text{hom}}(x) = \begin{cases} g \cdot (Lf - x) \cdot (\rho_{\text{resin}} - \rho_{\text{air}}) + \frac{12 \cdot \bar{U}}{H^2} \cdot [(Lf - x) \cdot \mu_{\text{resin}} + (L - Lf) \cdot \mu_{\text{air}}] & (\text{for } x < Lf) \\ -\frac{1}{5} \cdot \bar{U}^2 \cdot (\rho_{\text{resin}} - \rho_{\text{air}}) & \\ \frac{12 \cdot \bar{U}}{H^2} \cdot (L - x) \cdot \mu_{\text{air}} & (\text{for } x > Lf) \end{cases} \quad (60)$$

On these two last equations there is a discontinuity at  $x = L_f$ . This is due to the assumptions of a flat flow front and of a parabolic velocity profile at every cross section, which is not true at the flow front region. However, this discontinuity represents only 2.1 Pa.

The derivative of the pressure along  $x$  is then:

$$\frac{dP(x)}{dx} = \begin{cases} -\left(g \cdot \rho_{\text{resin}} + \frac{12 \cdot \bar{U} \cdot \mu_{\text{resin}}}{H^2}\right) & (\text{for } x < L_f) \\ -\left(g \cdot \rho_{\text{air}} + \frac{12 \cdot \bar{U} \cdot \mu_{\text{air}}}{H^2}\right) & (\text{for } x > L_f) \end{cases} \quad (61)$$

and:

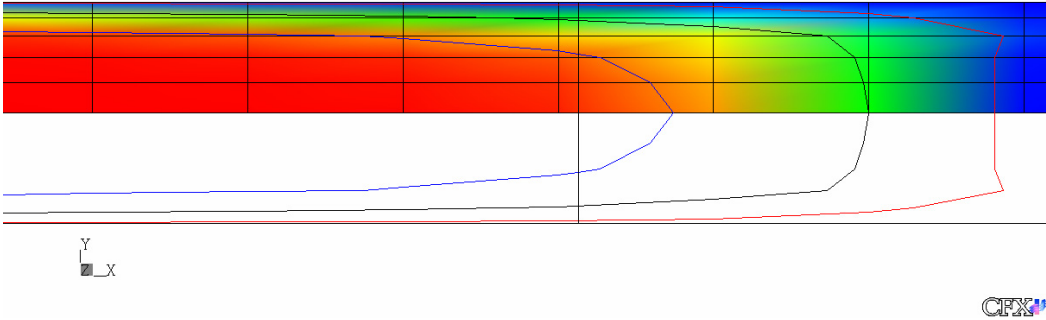
$$\frac{dP^{\text{hom}}(x)}{dx} = \begin{cases} -\left[g \cdot (\rho_{\text{resin}} - \rho_{\text{air}}) + \frac{12 \cdot \bar{U} \cdot \mu_{\text{resin}}}{H^2}\right] & (\text{for } x < L_f) \\ -\frac{12 \cdot \bar{U} \cdot \mu_{\text{air}}}{H^2} & (\text{for } x > L_f) \end{cases} \quad (62)$$

Due to symmetry, only half of the geometry was modelled. The simulations were performed with four different meshes: mesh1 with 24 elements on the longitudinal direction by 5 on the transversal direction, mesh2 with 48 by 5 elements, mesh3 with 24 by 20 elements, and mesh4 with 48 by 20 elements.

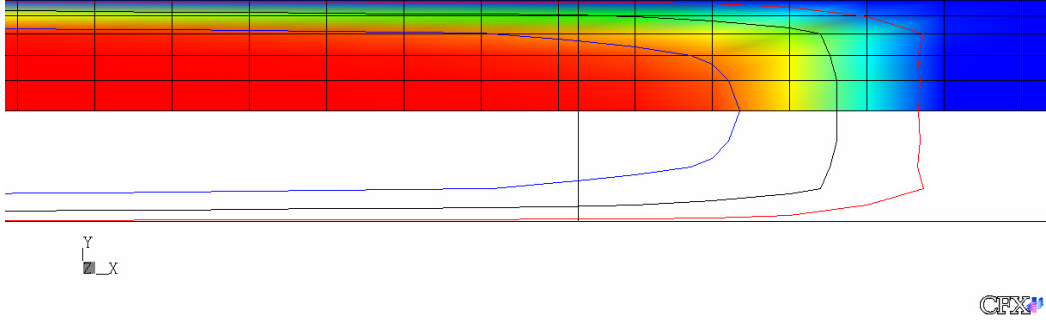
The position of the resin-air interface after 0.35 s is represented in Fig. 6a-6d. The three contour lines denote the resin volume fractions of 0.9, 0.5 and 0.1. The vertical line indicates the theoretical position of the flow front, obtained with equation (48), which for  $t = 0.35$  s results in  $L_f = 36.3$  mm.

It is noticeable that, for the four meshes, the interface is captured within two mesh elements, proving the efficiency of the compressive discretization schemes. Increasing the number of elements on the longitudinal direction improves its definition in that direction, but does not change its position. By increasing the number of elements on the transverse direction, the interface position gets closer to its theoretical position, though it is always ahead.

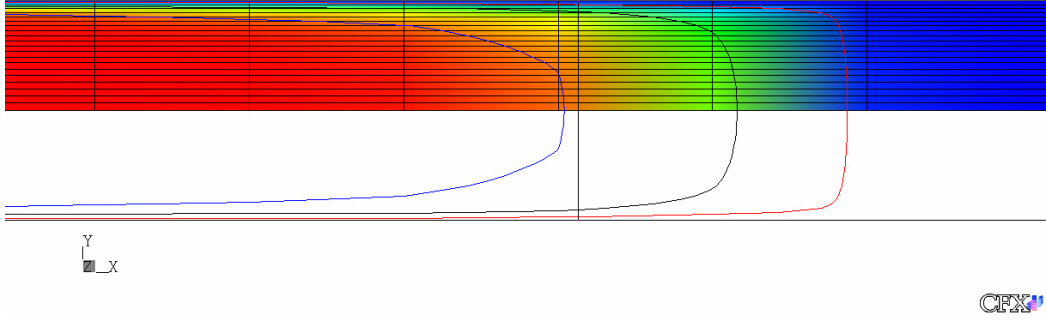
However, the most important conclusion from these simulations is that the interface does not touch the walls, there existing a layer of air between the resin and the walls. This is clearly not in accordance with reality. The volume of resin which is ahead of the theoretical position of the flow front (the vertical line) shall correspond to the volume of resin lacking near the walls.



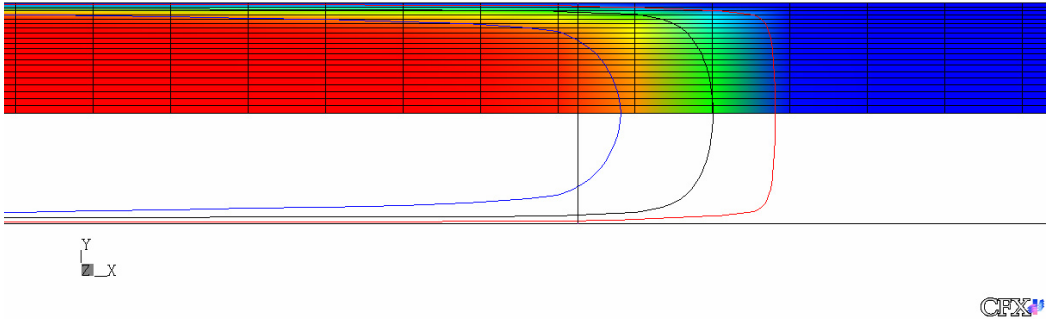
(a)



(b)



(c)



(d)

**Fig. 6: Position of the resin-air interface for  $t = 0.35$  s. Contour lines denote the resin volume fractions 0.9, 0.5 and 0.1. (a) mesh1:  $24 \times 5$  elements; (b) mesh2:  $48 \times 5$  elements; (c) mesh3:  $24 \times 20$  elements; (d) mesh4:  $48 \times 20$  elements.**

In Fig. 7a-7d, the value of the resin volume fraction along the transverse direction, at midway between the inlet and the theoretical position of the flow front, is represented.

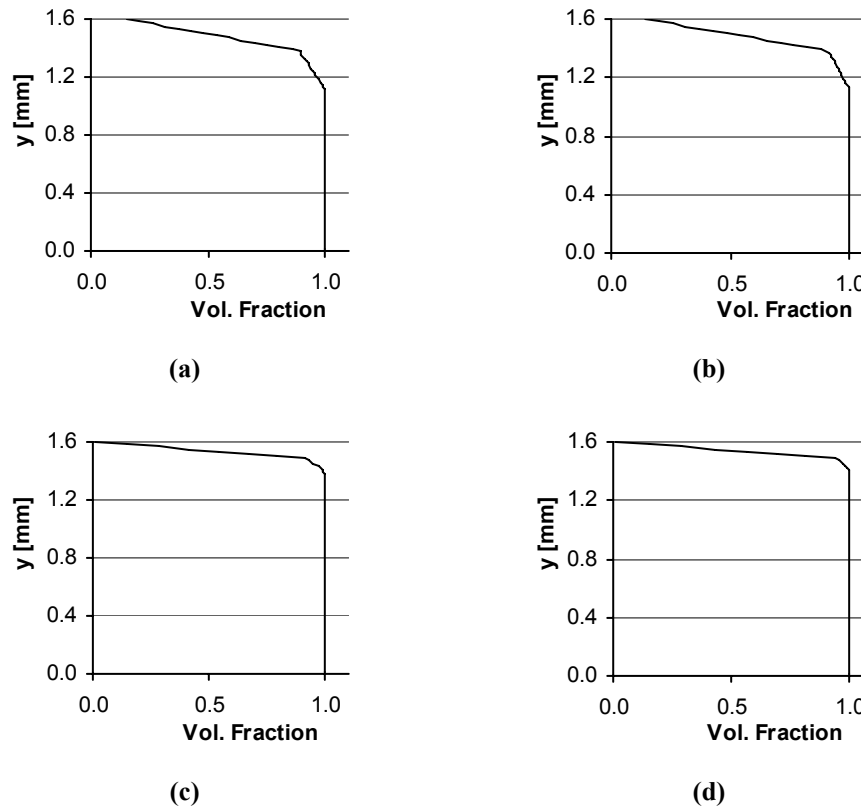


**Fig. 7: Resin volume fraction along the transverse direction, at  $x = \frac{1}{2} L_f$ , for  $t = 0.35$  s. (a) mesh1, average volume fraction = 0.925; (b) mesh2, average volume fraction = 0.928; (c) mesh3, average volume fraction = 0.960; (d) mesh4, average volume fraction = 0.962.**

From this last figure, one concludes that increasing the number of mesh elements on the longitudinal direction does not change this behaviour, while increasing the number of elements on the transverse direction causes the average volume fraction to increase but the volume fraction on the wall nodes to decrease.

The viscosity is obtained as the volume fraction weighted phases' viscosities by equation (23). Because the resin volume fraction on the walls is close to zero, the computed viscosity on the walls nodes will be much smaller than its actual value, resulting in a higher velocity gradient on the transverse direction next to the walls and consequently a wrong velocity profile. When solving the cure and energy equations, this will cause an error on the advection terms of those equations, which will possibly lead to completely wrong final results.

Also due to the lower computed values of the viscosity on the walls nodes, the wall shear stress, which is obtained by equation (52), will be lower than its real value, leading to a lower value of the viscous effect contribution to pressure. This is of major importance, as

injection pressure is one of the most important parameters to be predicted by numerical simulation.

Comparing, for  $t = 0.35$  s, the inlet pressure obtained from CFX with mesh1 (the coarsest mesh), 536 Pa, and the theoretical pressure obtained with equations (58) or (60), 574 Pa, the pressure obtained with CFX is just 6.5% lower. However, the error caused by the lower shear stress on the walls is masked by an increase of the gravity effect in pressure due to the fact that the flow front is ahead of its theoretical position.

The pressure due to the gravity effect may be evaluated from the hydrostatic law as [89]:

$$\frac{dP(\text{grav})}{dx} = -\rho \cdot g \quad (63)$$

or:

$$\frac{dP^{\text{hom}}(\text{grav})}{dx} = -(\rho - \rho_{\text{air}}) \cdot g \quad (64)$$

which, considering the pressure at the outlet as zero, leads to:

$$P(\text{grav}) = \int_x^L \rho \cdot g \, dx \quad (65)$$

or:

$$P^{\text{hom}}(\text{grav}) = \int_x^L (\rho - \rho_{\text{air}}) \cdot g \, dx \quad (66)$$

The pressure due to the viscous effect may be regarded as the difference between the whole pressure and the pressure due to the gravity effect:  $P - P(\text{grav})$ , or  $P^{\text{hom}} - P^{\text{hom}}(\text{grav})$ . This is not completely true, as there is also a small contribution from the rate of change of linear momentum, 2.1 Pa, and thereby it is not designated here by  $P(\text{visc})$ .

Thus, the comparison will be done between  $P^{\text{hom}} - P^{\text{hom}}(\text{grav})$ , which is obtained as:

$$\left( \begin{array}{c} P^{\text{hom}}(x) - \\ P^{\text{hom}}(\text{grav})(x) \end{array} \right) = \begin{cases} \frac{12 \cdot \bar{U}}{H^2} \cdot [(Lf - x) \cdot \mu_{\text{resin}} + (L - Lf) \cdot \mu_{\text{air}}] & (\text{for } x < Lf) \\ -\frac{1}{5} \cdot \bar{U}^2 \cdot (\rho_{\text{resin}} - \rho_{\text{air}}) & \\ \frac{12 \cdot \bar{U}}{H^2} \cdot (L - x) \cdot \mu_{\text{air}} & (\text{for } x > Lf) \end{cases} \quad (67)$$

and the pressure obtained from CFX,  $P^{CFX}$ , minus its gravity contribution:

$$P^{CFX} - P^{CFX}(\text{grav}) = P^{CFX} - \left( \int_x^L (\rho - \rho_{\text{air}}) \cdot g \, dx \right)_{CFX} \quad (68)$$

In this equation, the integration is done along the centre line where the flow front has its most advanced position.

The comparison between the results obtained from the simulations and the theoretical ones are represented in Fig. 8a-8d. The four graphics, obtained with the four different meshes, are quite similar.

The derivative of  $(P^{CFX} - P^{CFX}(\text{grav}))$  is compared with theoretical values in Fig. 9a-9d. It is possible to observe the error induced in  $(P^{CFX} - P^{CFX}(\text{grav}))$ . The derivative should be constant for each phase, from equation (67) it should take the value -6076 Pa/m for the resin and -2.2 Pa/m for the air. Instead, a nearly ramp function is observed.

In Table 1, the results obtained at the inlet are presented and compared with the theoretical ones. It is interesting to notice that when increasing, the number of mesh elements on the transverse direction by a factor of 4, from mesh1 to mesh3 and from mesh2 to mesh4, the error of the obtained pressure,  $P^{CFX}$ , which is always negative, increases, in absolute value, from 6.7 % to 9.0 % and from 6.3 % to 8.5 %, respectively. At a first glance this might look somehow unexpected, but the reason is that the error of the gravity contribution to pressure,  $P^{CFX}(\text{grav})$ , which is always positive, decreased from 10.9 % to 5.4 % and from 10.3 % to 5.0 %, respectively. This was already observed in Fig. 6a-6d, the interface positions obtained with mesh3 and mesh4, though always ahead, are closer to the theoretical position than the obtained with mesh1 and mesh2.

**Table 1: Comparison between the theoretical pressures and the pressures obtained from the simulations, at  $x = 0$  (inlet), at  $t = 0.35$  s. The errors relative to the theoretical values are presented inside brackets.**

	$P^{\text{hom}}$	$P^{\text{hom}}(\text{grav})$	$P^{\text{hom}} - P^{\text{hom}}(\text{grav})$
Theory	573.7	355.3	218.4
	$P^{CFX}$	$P^{CFX}(\text{grav})$	$P^{CFX} - P^{CFX}(\text{grav})$
mesh1: 24×5 elem.	535.2 (-6.7 %)	394.0 (+10.9 %)	141.1 (-35.4 %)
mesh2: 48×5 elem.	537.3 (-6.3 %)	391.7 (+10.3 %)	145.7 (-33.3 %)
mesh3: 24×20 elem.	522.1 (-9.0 %)	374.3 (+5.4 %)	147.8 (-32.4 %)
mesh4: 48×20 elem.	524.9 (-8.5 %)	372.9 (+5.0 %)	152.0 (-30.4 %)

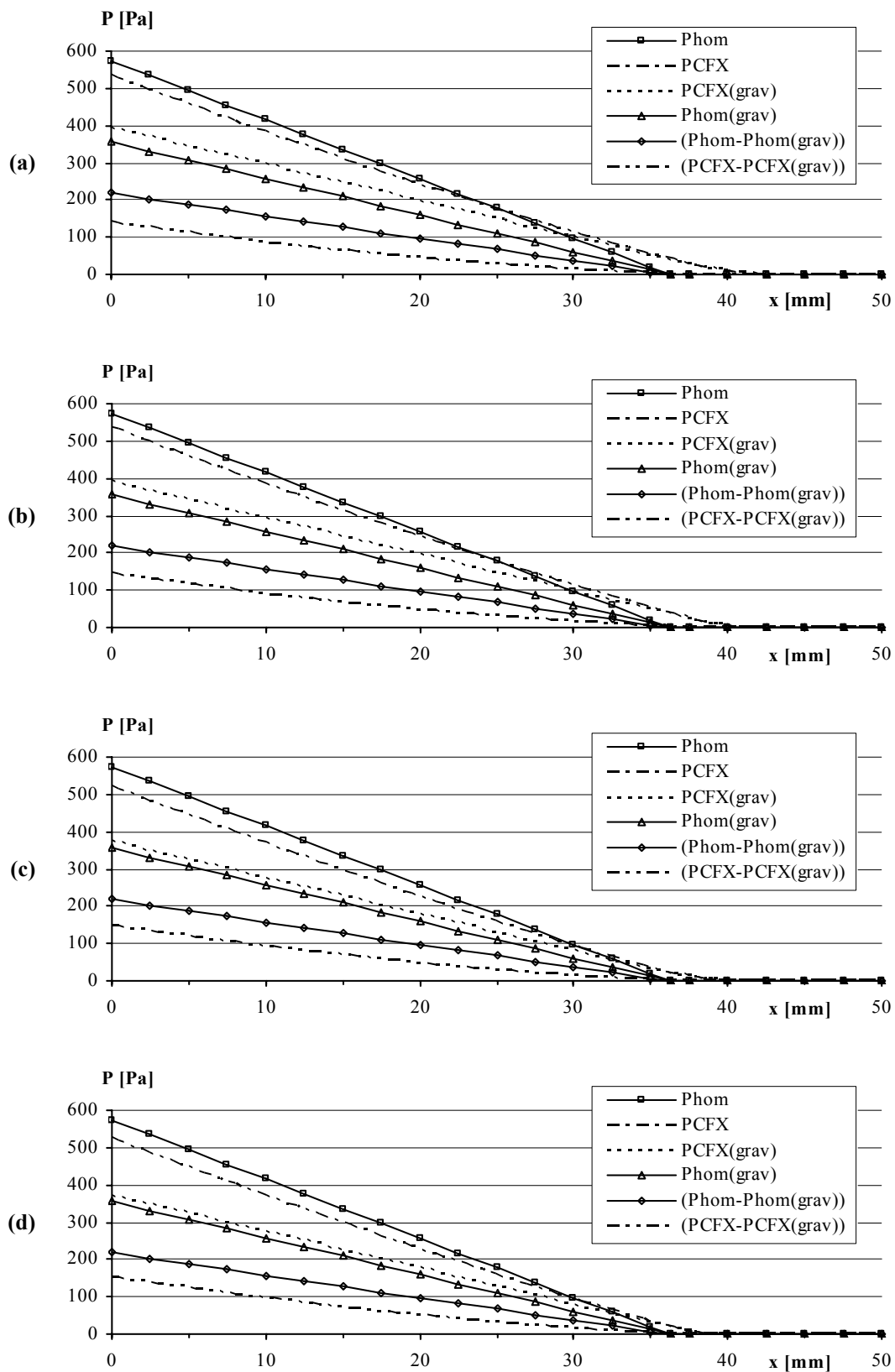


**Fig. 8: Comparison between the pressures obtained from simulations and theoretical values, for  $t = 0.35$  s. (a) mesh1; (b) mesh2; (c) mesh3; (d) mesh 4.**



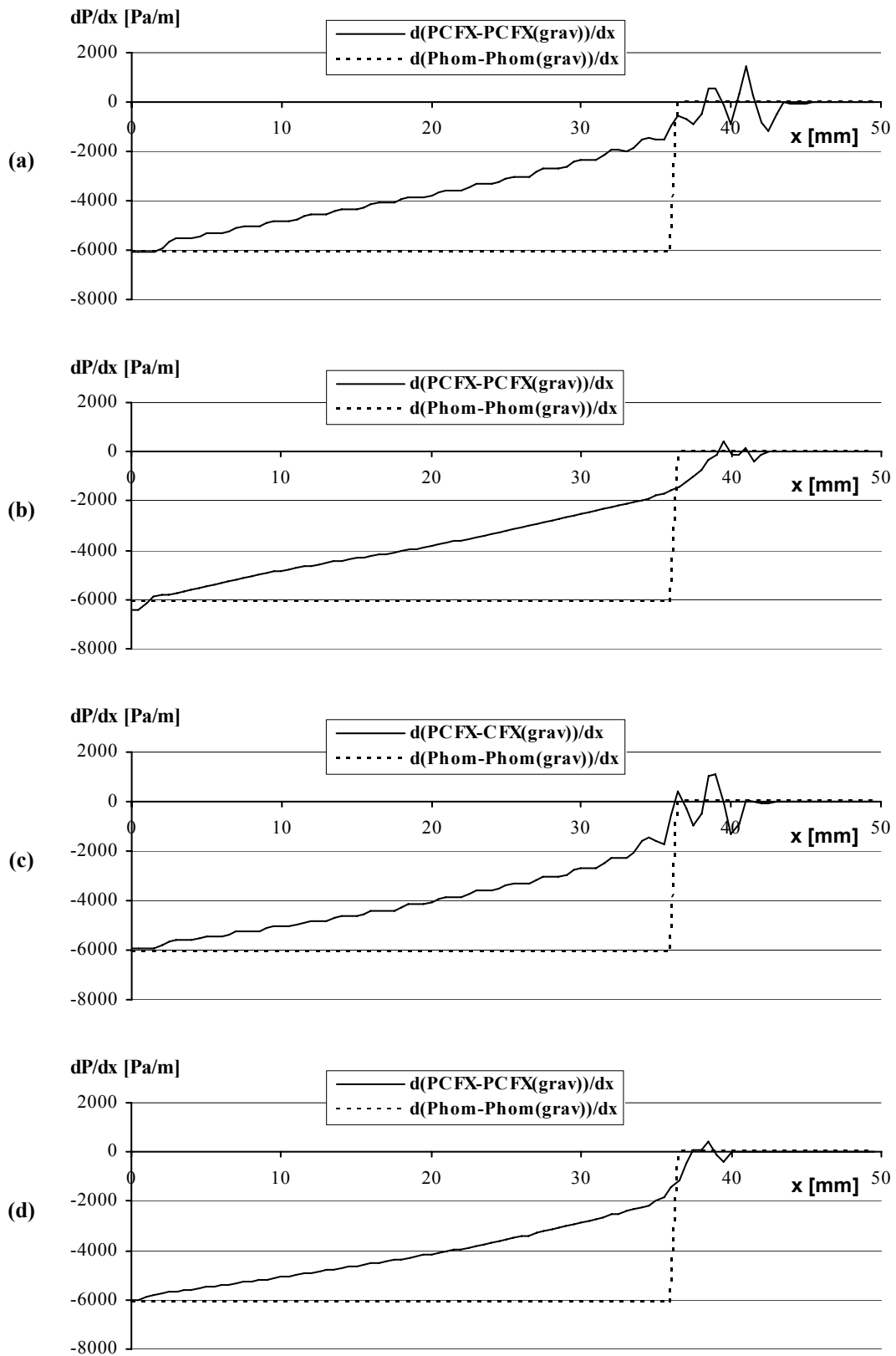


**Fig. 9:** Comparison between the derivative of ( $P^{CFX-PCFX(grav)}$ ) and theoretical values, for  $t = 0.35$  s. (a) mesh1; (b) mesh2; (c) mesh3; (d) mesh 4.

The error of ( $P^{CFX} - P^{CFX}(\text{grav})$ ), in absolute value, shows only a tiny decrease when increasing the number of mesh elements. Mesh4 has 8 times the number of mesh elements of mesh1, and the error only decreased from 35.4 % to 30.4 %. Thus, it seems that increasing the number of mesh elements, at least within reasonable limits, is not the cure for the problem.

The computing time, for each mesh, to complete 0.47 s of simulation is shown in Fig. 10. CFX was running in double precision, in a workstation PC with a Pentium® 4 2.5 MHz processor and 512 MB RAM memory, using Windows® 2000 operating system.

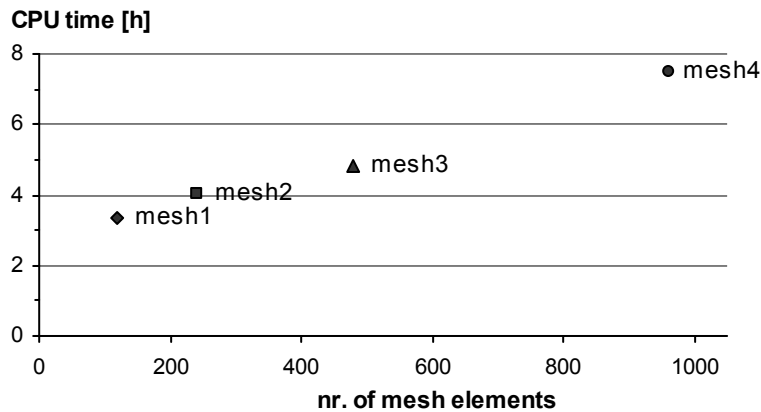


Fig. 10: Computing time for the simulations to complete 0.47 s.

This unwanted behaviour has although been mentioned by some authors, who claim that that in filling simulations the no-slip condition on mould walls should be imposed only on the filled portion of the mould, as a no-slip boundary condition in the air will prevent the flow front from touching the walls [14, 56].

## 2.2 The inhomogeneous model

### 2.2.1 Physical model

Despite the physical model described in the previous sub-section being theoretically correct, it is unable to produce satisfactory results with the also physically correct no-slip boundary condition on the walls.

CFX does not allow the implementation of conditional boundary conditions: it is not possible to define a wall boundary condition as no-slip if the volume fraction of the liquid phase is above a certain value, 0.5 for instance, and as free-slip if it is below. Therefore, the only way to prescribe a no-slip boundary condition on the filled portion of

the mould and a free-slip boundary condition in the empty portion is by using the CFX's inhomogeneous multiphase flow model. In the inhomogeneous model, each phase has its own flow field and they interact via interphase transfer terms [83]. According to the assumption made by this model, the flow is described by:

the equations of conservation of mass of each phase:

$$\frac{\partial(r_\alpha \cdot \rho_\alpha)}{\partial t} + \nabla \cdot (r_\alpha \cdot \rho_\alpha \cdot \overline{U}_\alpha) = 0 \quad (69)$$

$$\frac{\partial(r_\beta \cdot \rho_\beta)}{\partial t} + \nabla \cdot (r_\beta \cdot \rho_\beta \cdot \overline{U}_\beta) = 0 \quad (70)$$

the momentum equations for phase  $\alpha$ :

x direction:

$$\begin{aligned} & \frac{\partial(r_\alpha \cdot \rho_\alpha \cdot u_\alpha)}{\partial t} + \frac{\partial(r_\alpha \cdot \rho_\alpha \cdot u_\alpha^2)}{\partial x} + \frac{\partial(r_\alpha \cdot \rho_\alpha \cdot u_\alpha \cdot v_\alpha)}{\partial y} + \frac{\partial(r_\alpha \cdot \rho_\alpha \cdot u_\alpha \cdot w_\alpha)}{\partial z} = \\ & -r_\alpha \cdot \frac{\partial p}{\partial x} + \frac{\partial}{\partial x} \left( 2 \cdot r_\alpha \cdot \mu_\alpha \cdot \frac{\partial u_\alpha}{\partial x} \right) + \frac{\partial}{\partial y} \left[ r_\alpha \cdot \mu_\alpha \cdot \left( \frac{\partial u_\alpha}{\partial y} + \frac{\partial v_\alpha}{\partial x} \right) \right] + \\ & \frac{\partial}{\partial z} \left[ r_\alpha \cdot \mu_\alpha \cdot \left( \frac{\partial u_\alpha}{\partial z} + \frac{\partial w_\alpha}{\partial x} \right) \right] + S_{M\alpha_x} + M_{\alpha\beta_x} \end{aligned} \quad (71)$$

y direction:

$$\begin{aligned} & \frac{\partial(r_\alpha \cdot \rho_\alpha \cdot v_\alpha)}{\partial t} + \frac{\partial(r_\alpha \cdot \rho_\alpha \cdot u_\alpha \cdot v_\alpha)}{\partial x} + \frac{\partial(r_\alpha \cdot \rho_\alpha \cdot v_\alpha^2)}{\partial y} + \frac{\partial(r_\alpha \cdot \rho_\alpha \cdot v_\alpha \cdot w_\alpha)}{\partial z} = \\ & -r_\alpha \cdot \frac{\partial p}{\partial y} + \frac{\partial}{\partial x} \left[ r_\alpha \cdot \mu_\alpha \cdot \left( \frac{\partial v_\alpha}{\partial x} + \frac{\partial u_\alpha}{\partial y} \right) \right] + \frac{\partial}{\partial y} \left( 2 \cdot r_\alpha \cdot \mu_\alpha \cdot \frac{\partial v_\alpha}{\partial y} \right) + \\ & \frac{\partial}{\partial z} \left[ r_\alpha \cdot \mu_\alpha \cdot \left( \frac{\partial v_\alpha}{\partial z} + \frac{\partial w_\alpha}{\partial y} \right) \right] + S_{M\alpha_y} + M_{\alpha\beta_y} \end{aligned} \quad (72)$$

z direction:

$$\begin{aligned} & \frac{\partial(r_\alpha \cdot \rho_\alpha \cdot w_\alpha)}{\partial t} + \frac{\partial(r_\alpha \cdot \rho_\alpha \cdot u_\alpha \cdot w_\alpha)}{\partial x} + \frac{\partial(r_\alpha \cdot \rho_\alpha \cdot v_\alpha \cdot w_\alpha)}{\partial y} + \frac{\partial(r_\alpha \cdot \rho_\alpha \cdot w_\alpha^2)}{\partial z} = \\ & -r_\alpha \cdot \frac{\partial p}{\partial z} + \frac{\partial}{\partial x} \left[ r_\alpha \cdot \mu_\alpha \cdot \left( \frac{\partial w_\alpha}{\partial x} + \frac{\partial u_\alpha}{\partial z} \right) \right] + \frac{\partial}{\partial y} \left[ r_\alpha \cdot \mu_\alpha \cdot \left( \frac{\partial w_\alpha}{\partial y} + \frac{\partial v_\alpha}{\partial z} \right) \right] \\ & + \frac{\partial}{\partial x} \left( 2 \cdot r_\alpha \cdot \mu_\alpha \cdot \frac{\partial w_\alpha}{\partial z} \right) + S_{M\alpha_z} + M_{\alpha\beta_z} \end{aligned} \quad (73)$$

or, in general vector form:

$$\begin{aligned} \frac{\partial(\mathbf{r}_\alpha \cdot \rho_\alpha \cdot \overline{\mathbf{U}}_\alpha)}{\partial t} + \nabla \cdot (\mathbf{r}_\alpha \cdot \rho_\alpha \cdot \overline{\mathbf{U}}_\alpha \otimes \overline{\mathbf{U}}_\alpha) = \\ -\mathbf{r}_\alpha \cdot \nabla p + \nabla \cdot \left[ \mathbf{r}_\alpha \cdot \mu_\alpha \cdot \left( \nabla \otimes \overline{\mathbf{U}}_\alpha + (\nabla \otimes \overline{\mathbf{U}}_\alpha)^T \right) \right] + \overline{\mathbf{S}}_{M\alpha} + \overline{\mathbf{M}}_{\alpha\beta} \end{aligned} \quad (74)$$

the momentum equations for phase  $\beta$ , for which just the vector form is presented:

$$\begin{aligned} \frac{\partial(\mathbf{r}_\beta \cdot \rho_\beta \cdot \overline{\mathbf{U}}_\beta)}{\partial t} + \nabla \cdot (\mathbf{r}_\beta \cdot \rho_\beta \cdot \overline{\mathbf{U}}_\beta \otimes \overline{\mathbf{U}}_\beta) = \\ -\mathbf{r}_\beta \cdot \nabla p + \nabla \cdot \left[ \mathbf{r}_\beta \cdot \mu_\beta \cdot \left( \nabla \otimes \overline{\mathbf{U}}_\beta + (\nabla \otimes \overline{\mathbf{U}}_\beta)^T \right) \right] + \overline{\mathbf{S}}_{M\beta} + \overline{\mathbf{M}}_{\beta\alpha} \end{aligned} \quad (75)$$

and the constraint that the volume fractions sum to unity:

$$\mathbf{r}_\alpha + \mathbf{r}_\beta = 1 \quad (76)$$

By assuming a different velocity field for each phase, the flow is characterized by 9 equations (8 of them partial differential equations) and 9 unknowns ( $p$ ,  $\mathbf{u}_\alpha$ ,  $\mathbf{v}_\alpha$ ,  $\mathbf{w}_\alpha$ ,  $\mathbf{u}_\beta$ ,  $\mathbf{v}_\beta$ ,  $\mathbf{w}_\beta$ ,  $\mathbf{r}_\alpha$  and  $\mathbf{r}_\beta$ ).

As in the homogeneous model,  $\mathbf{S}_M$  represents the source of momentum due to the gravity force, and is given, for phase  $\alpha$  and  $\beta$ , respectively, by:

$$\overline{\mathbf{S}}_{M\alpha} = \mathbf{r}_\alpha \cdot (\rho_\alpha - \rho_{\text{ref}}) \cdot \vec{\mathbf{g}} \quad (77)$$

$$\overline{\mathbf{S}}_{M\beta} = \mathbf{r}_\beta \cdot (\rho_\beta - \rho_{\text{ref}}) \cdot \vec{\mathbf{g}} \quad (78)$$

$\mathbf{M}_{\alpha\beta}$  and  $\mathbf{M}_{\beta\alpha}$  are interphase momentum transfer terms, and they represent, respectively, the force per unit volume exerted by phase  $\beta$  on phase  $\alpha$ , and by phase  $\alpha$  on phase  $\beta$ . These interfacial forces are equal in absolute value and opposite in direction [83]:

$$\overline{\mathbf{M}}_{\alpha\beta} = -\overline{\mathbf{M}}_{\beta\alpha} \quad (79)$$

As both phases, resin and air, are continuous, there is not any implemented model in CFX for  $\mathbf{M}_{\alpha\beta}$ . It is simply defined as [83, 90]:

$$\overline{\mathbf{M}}_{\alpha\beta} = C_D \cdot \rho_{\alpha\beta} \cdot A_{\alpha\beta} \cdot |\overline{\mathbf{U}}_\beta - \overline{\mathbf{U}}_\alpha| \cdot (\overline{\mathbf{U}}_\beta - \overline{\mathbf{U}}_\alpha) \quad (80)$$

where  $C_D$  is a non-dimensional drag coefficient,  $\rho_{\alpha\beta}$  is the mixture density given by:

$$\rho_{\alpha\beta} = \rho_\alpha \cdot \mathbf{r}_\alpha + \rho_\beta \cdot \mathbf{r}_\beta \quad (81)$$

and  $A_{\alpha\beta}$  is the interfacial area per unit volume, given by:

$$A_{\alpha\beta} = \frac{r_\alpha \cdot r_\beta}{d_{\alpha\beta}} \quad (82)$$

where  $d_{\alpha\beta}$  is a user-specified interface length scale.

CFX requires the definition of  $C_D$  and  $d_{\alpha\beta}$ . However, substituting the expressions of equations (81) and (82) into equation (80), leads to:

$$\overline{M_{\alpha\beta}} = \frac{C_D}{d_{\alpha\beta}} \cdot r_\alpha \cdot r_\beta \cdot (\rho_\alpha \cdot r_\alpha + \rho_\beta \cdot r_\beta) \cdot |\overline{U_\beta} - \overline{U_\alpha}| \cdot (\overline{U_\beta} - \overline{U_\alpha}) \quad (83)$$

from which one concludes that what matters is the quotient  $C_D/d_{\alpha\beta}$  and not their individual values. This was checked by setting in CFX different values of  $C_D$  and  $d_{\alpha\beta}$  but keeping their quotient constant, and exactly the same results were obtained.

It is interesting to notice that as the volume fraction of one of the phases approximates zero, the term  $M_{\alpha\beta}$  vanishes. Therefore, as one would expect,  $M_{\alpha\beta}$  is only meaningful at the interface.

## 2.2.2 Numerical model

The discretization of the governing equations is done in the same way as for the homogeneous model. The discrete forms of the equations are therefore [91]:

the equations of conservation of mass of each phase:

$$\frac{\partial}{\partial t} \left( \int_V r_\alpha \cdot \rho_\alpha \, dV \right) + \sum_{ip} (r_\alpha \cdot \rho_\alpha \cdot \overline{U_\alpha} \cdot \vec{n} \cdot A)_{ip} = 0 \quad (84)$$

$$\frac{\partial}{\partial t} \left( \int_V r_\beta \cdot \rho_\beta \, dV \right) + \sum_{ip} (r_\beta \cdot \rho_\beta \cdot \overline{U_\beta} \cdot \vec{n} \cdot A)_{ip} = 0 \quad (85)$$

the momentum equations for phase  $\alpha$ :

in x direction:

$$\begin{aligned} & \frac{\partial}{\partial t} \left( \int_V r_\alpha \cdot \rho_\alpha \cdot u_\alpha \, dV \right) + \sum_{ip} \dot{m}_{\alpha ip} \cdot u_{\alpha ip} = -r_{\alpha ip} \cdot \sum_{ip} (n_x \cdot A \cdot p)_{ip} + \\ & \sum_{ip} \left\{ r_\alpha \cdot \mu_\alpha \cdot \left[ 2 \cdot \frac{\partial u_\alpha}{\partial x} \cdot n_x + \left( \frac{\partial u_\alpha}{\partial y} + \frac{\partial v_\alpha}{\partial x} \right) \cdot n_y + \left( \frac{\partial u_\alpha}{\partial z} + \frac{\partial w_\alpha}{\partial x} \right) \cdot n_z \right] \cdot A \right\}_{ip} + \\ & \overline{S_{M\alpha_x}} \cdot V + \overline{M_{\alpha\beta_x}} \cdot V \end{aligned} \quad (86)$$

in y direction:

$$\begin{aligned} & \frac{\partial}{\partial t} \left( \int_V r_\alpha \cdot \rho_\alpha \cdot v_\alpha \, dV \right) + \sum_{ip} \dot{m}_{\alpha,ip} \cdot v_{\alpha,ip} = -r_{\alpha,ip} \cdot \sum_{ip} (n_y \cdot A \cdot p)_{ip} + \\ & \sum_{ip} \left\{ r_\alpha \cdot \mu_\alpha \cdot \left[ \left( \frac{\partial v_\alpha}{\partial x} + \frac{\partial u_\alpha}{\partial y} \right) \cdot n_x + 2 \cdot \frac{\partial v_\alpha}{\partial x} \cdot n_y + \left( \frac{\partial v_\alpha}{\partial z} + \frac{\partial w_\alpha}{\partial y} \right) \cdot n_z \right] \cdot A \right\}_{ip} + \quad (87) \\ & \overline{S_{M\alpha_y}} \cdot V + \overline{M_{\alpha\beta_y}} \cdot V \end{aligned}$$

in z direction:

$$\begin{aligned} & \frac{\partial}{\partial t} \left( \int_V r_\alpha \cdot \rho_\alpha \cdot w_\alpha \, dV \right) + \sum_{ip} \dot{m}_{\alpha,ip} \cdot w_{\alpha,ip} = -r_{\alpha,ip} \cdot \sum_{ip} (n_z \cdot A \cdot p)_{ip} + \\ & \sum_{ip} \left\{ r_\alpha \cdot \mu_\alpha \cdot \left[ \left( \frac{\partial w_\alpha}{\partial x} + \frac{\partial u_\alpha}{\partial z} \right) \cdot n_x + \left( \frac{\partial w_\alpha}{\partial y} + \frac{\partial v_\alpha}{\partial z} \right) \cdot n_y + 2 \cdot \frac{\partial w_\alpha}{\partial z} \cdot n_z \right] \cdot A \right\}_{ip} + \quad (88) \\ & \overline{S_{M\alpha_z}} \cdot V + \overline{M_{\alpha\beta_z}} \cdot V \end{aligned}$$

where  $\dot{m}_{\alpha,ip}$  is the discrete mass flow of phase  $\alpha$  through a face of the finite volume, obtained from the previous iteration as:

$$\dot{m}_{\alpha,ip} = \left( r_\alpha \cdot \rho_\alpha \cdot \overline{U_\alpha} \cdot \vec{n} \cdot A \right)_{ip} \quad (89)$$

The three momentum equations for phase  $\beta$  are analogous to the three momentum equations for phase  $\alpha$  presented above.

As the second order backward Euler scheme is used, the transient term on the momentum equations (86) to (88) is approximated as:

$$\begin{aligned} & \frac{\partial}{\partial t} \left( \int_V r_\alpha \cdot \rho_\alpha \cdot U_{\alpha_i} \, dV \right) \approx \frac{V}{\Delta t} \cdot \left\{ \frac{1}{\theta \cdot (1 + \theta)} \cdot \right. \\ & \left. \left[ (2 + \theta) \cdot \theta \cdot r_\alpha \cdot \rho_\alpha \cdot U_{\alpha_i} - (1 + \theta)^2 \cdot r_\alpha^0 \cdot \rho_\alpha^0 \cdot U_{\alpha_i}^0 + r_\alpha^{00} \cdot \rho_\alpha^{00} \cdot U_{\alpha_i}^{00} \right] \right\} \quad (90) \end{aligned}$$

where  $\theta$  is the quotient between the old and the new time step, as already defined in equation (36). The values of the variables and of the derivatives at the integration points are obtained according to what was previously stated for the homogeneous model.

### 2.2.3 Case study

The case under study is the same one used for the homogeneous model: the filling of a space between two parallel plates with a resin, as represented in Fig. 4. However, now the no-slip condition on the walls is only applied to the equations referring to the resin phase, while the free-slip condition is applied to the equations referring to the air phase.

Consequently, as the wall shear stress is zero for the air phase and, due to this, the velocity profile of the air at the outlet is expected to be flat, the theoretical pressure defined with these boundary conditions,  $P^{\text{inhom}}$ , is slightly different than the one defined with the boundary conditions used in the homogeneous model,  $P^{\text{hom}}$ .

For these boundary conditions:

$$\iint_{\text{cs}} \mathbf{u} \cdot \rho \cdot (\bar{\mathbf{U}} \cdot \bar{\mathbf{n}}) dA = -\bar{U}^2 \cdot H \cdot W \cdot \left( \frac{6}{5} \cdot \rho_{\text{resin}} - \rho_{\text{air}} \right) \quad (91)$$

and:

$$F_w = \iint_{\text{walls}} \tau_w dA = 2 \times \int_0^{L_f} \frac{6 \cdot \mu \cdot \bar{U}}{H} \cdot W dx = \frac{12 \cdot \bar{U} \cdot H \cdot W \cdot \mu_{\text{resin}} \cdot L_f}{H^2} \quad (92)$$

Therefore,  $P^{\text{inhom}}(x)$  is given by:

$$P^{\text{inhom}}(x) = \begin{cases} g \cdot (L_f - x) \cdot (\rho_{\text{resin}} - \rho_{\text{air}}) \\ + \frac{12 \cdot \bar{U} \cdot \mu_{\text{resin}}}{H^2} \cdot (L_f - x) - \frac{1}{5} \cdot \bar{U}^2 \cdot \rho_{\text{resin}} & (\text{for } x < L_f) \\ 0 & (\text{for } x > L_f) \end{cases} \quad (93)$$

As in the analysis done for the homogeneous model, the gravity effect in pressure may be obtained from:

$$P^{\text{inhom}}(\text{grav})(x) = \int_x^L (\rho - \rho_{\text{air}}) \cdot g dx \quad (94)$$

and the pressure due to the viscous effect as:

$$\left( \begin{array}{c} P^{\text{inhom}}(x) - \\ P^{\text{inhom}}(\text{grav})(x) \end{array} \right) = \begin{cases} \frac{12 \cdot \bar{U} \cdot \mu_{\text{resin}}}{H^2} \cdot (L_f - x) - \frac{1}{5} \cdot \bar{U}^2 \cdot \rho_{\text{resin}} & (\text{for } x < L_f) \\ 0 & (\text{for } x > L_f) \end{cases} \quad (95)$$

As mentioned before, CFX requires the definition of the parameters  $C_D$  and  $d_{\alpha\beta}$  to evaluate  $M_{\alpha\beta}$ . But, because of the fact already stated, that what matters is their quotient ( $C_D/d_{\alpha\beta}$ ) and not their individual values,  $d_{\alpha\beta}$  was kept constant with the default CFX value ( $1 \times 10^{-3}$  m), and  $C_D$  was varied between 0.05 and 500.

The simulations were performed with mesh2 (48 by 5 elements) used for the homogeneous model. The time step is  $2 \times 10^{-4}$  s, the residuals convergence target which shall be achieved by all equations, except the volume fraction equations, is  $10^{-5}$ , up to a maximum of 50 iterations within each time step. CFX automatically sets the convergence criterion for the volume fraction equations, as these are usually more difficult to converge, to 10 times the specified convergence target [83, 92, 93].

The positions of the resin-air interface, for  $t = 0.35$  s, obtained with  $C_D$  set to 0.05, 0.5, 5 and 50, are represented in Fig. 11a-11d.

The results obtained with  $C_D$  set to 0.05, 0.5 and 5 are very similar. Unlike in the homogeneous model simulations, now the interface touches the walls and, clearly upstream of the interface there is resin and downstream of it there is air. Considering the interface position the location where the volume fraction is 0.5, it is in very good agreement with its theoretical position.

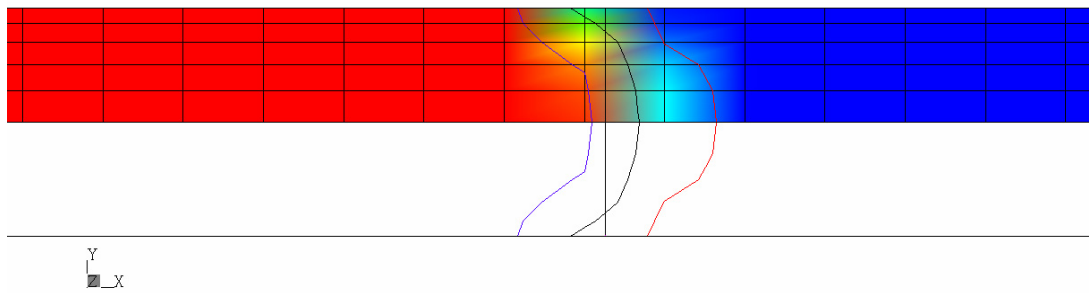
Although, when  $C_D$  is increased to 50, Fig. 11d, the behaviour becomes similar to that of the homogeneous model. The reason for this is that when  $M_{\alpha\beta}$  increases, the phases' flow fields tend to equalize each other. Actually, the homogeneous model may be regarded as a special case of the inhomogeneous model for a very large value of  $M_{\alpha\beta}$ .

For these simulations, the comparison between the pressures obtained from simulation and the theoretical ones is shown in Fig. 12a-12d. As expected, because of the results shown in Fig. 11a-11d, the graphics of Fig. 12a-12c are similar and the results obtained from simulations nearly match the theoretical ones. As also expected, for  $C_D = 50$ , Fig. 12d, the pressure values obtained from simulation become similar to those obtained with the homogeneous model.

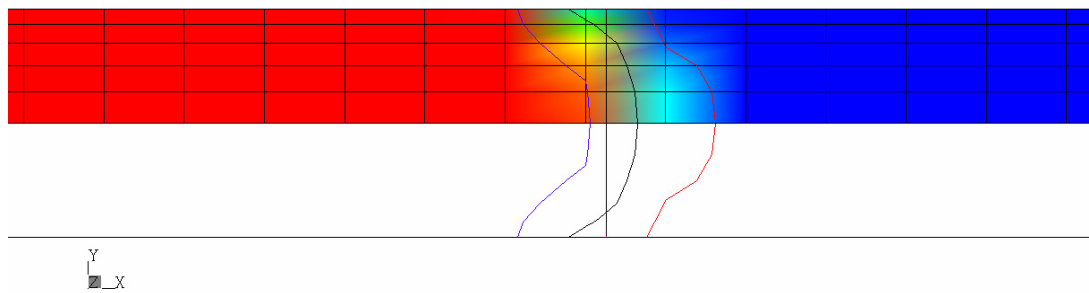
The comparison between the derivative along  $x$  of ( $P^{\text{inhom}}(x) - P^{\text{inhom}}(\text{grav})(x)$ ) and ( $P^{\text{CFX}} - P^{\text{CFX}}(\text{grav})$ ) is shown in Fig. 13a-13d. On the first three graphics, the results from simulations match the theoretical values for the majority of the domain, except for the flow front region. However for the two smallest values of  $C_D$ , the error on this region is greater than for  $C_D = 5$ . For  $C_D = 50$ , the graphic is again similar to the homogeneous model results.

In Table 2, the results and the errors relative to theoretical values, at the inlet, for each value of  $C_D$  are presented. Comparing these results with the ones presented in Table 1, obtained with the homogeneous model, one concludes that, for  $C_D$  equal to 0.05, 0.5 and 5, the errors were considerably reduced. For the same mesh, mesh2, the whole

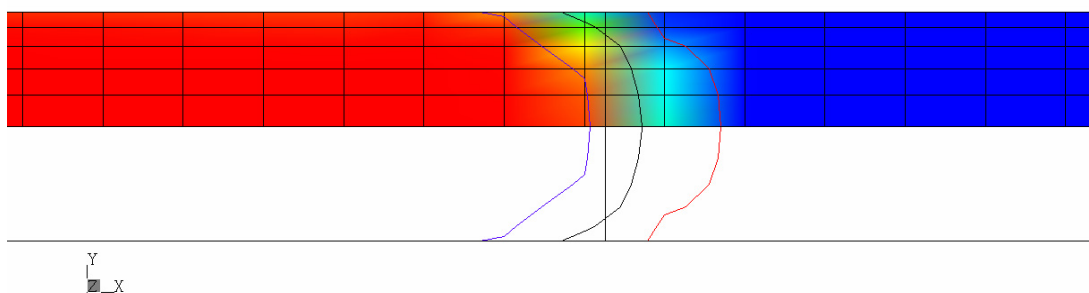




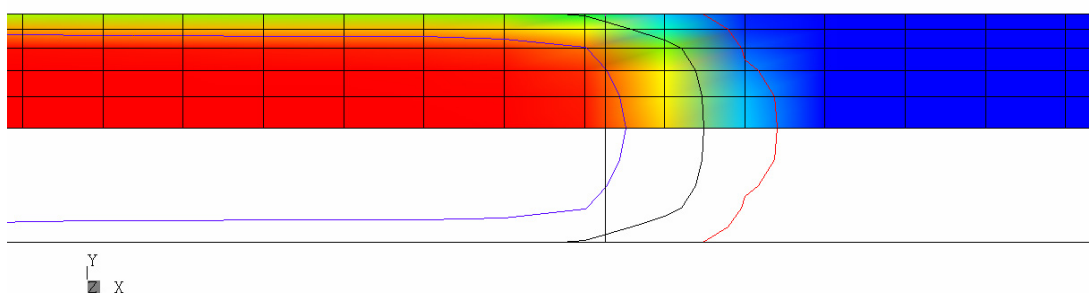
(a)



(b)



(c)



(d)

**Fig. 11: Position of the resin-air interface for  $t = 0.35$  s, obtained using mesh2. Contour lines denote the resin volume fractions 0.9, 0.5 and 0.1. The vertical line represents the theoretical position of the flow front. (a)  $C_D = 0.05$ ; (b)  $C_D = 0.5$ ; (c)  $C_D = 5$ ; (d)  $C_D = 50$ .**

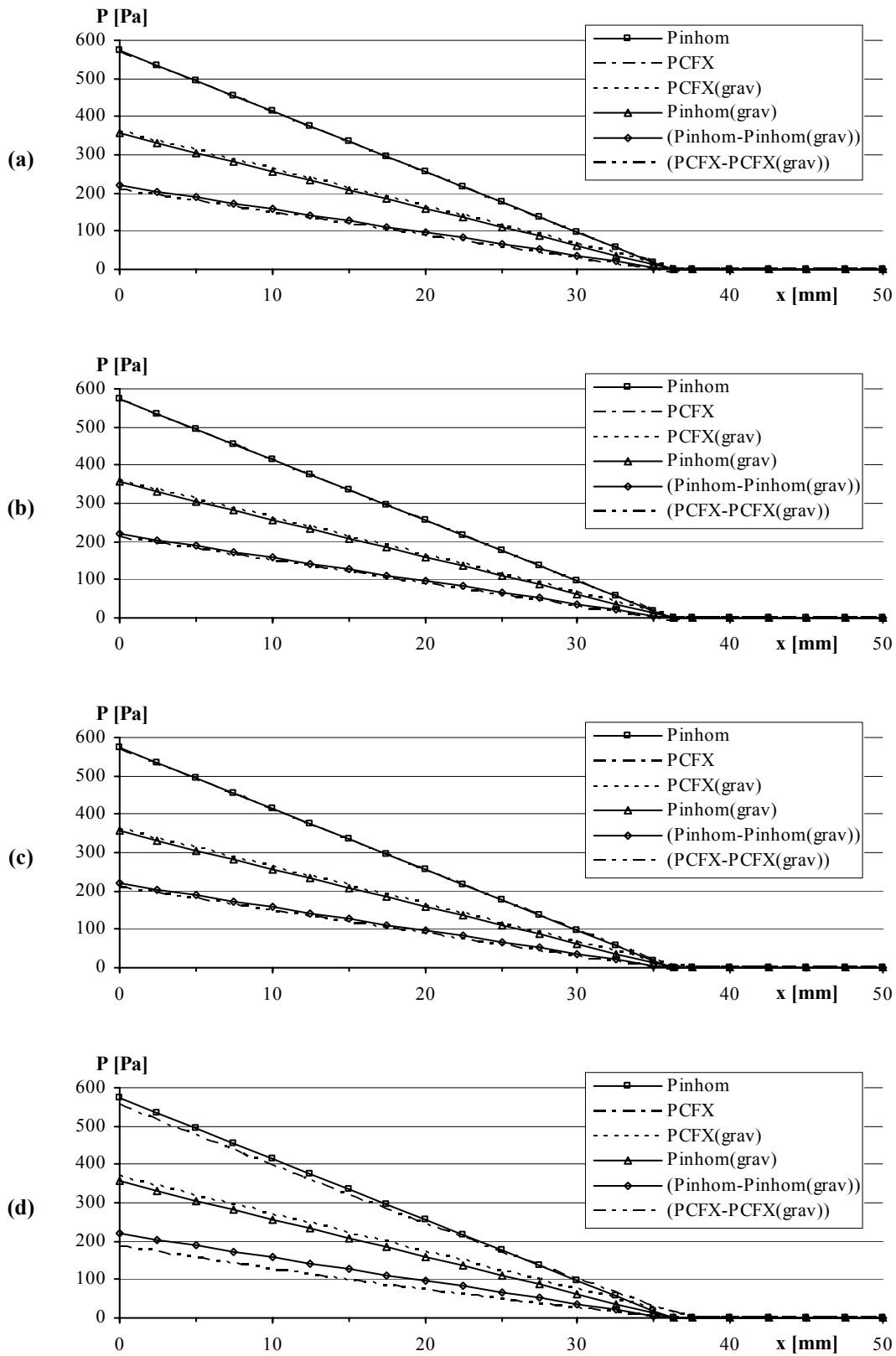


Fig. 12: Comparison between the pressures obtained from simulations, with mesh2, and theoretical values, for  $t = 0.35$  s. (a)  $C_D = 0.05$ ; (b)  $C_D = 0.5$ ; (c)  $C_D = 5$ ; (d)  $C_D = 50$ .

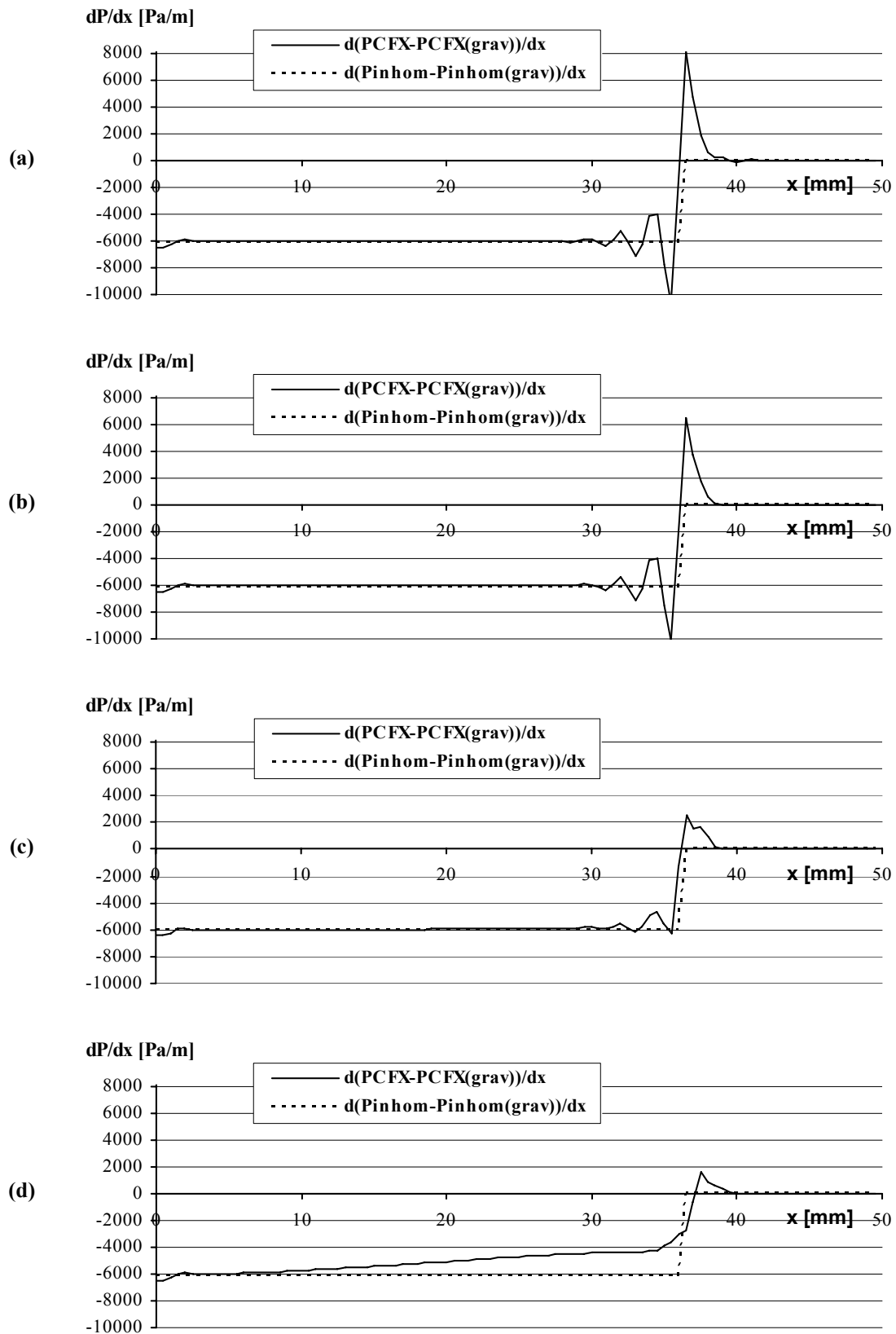


Fig. 13: Comparison between the derivative of ( $P^{CFX}-P^{CFX}(\text{grav})$ ), obtained with mesh2, and theoretical values, for  $t = 0.35$  s. (a)  $C_D = 0.05$ ; (b)  $C_D = 0.5$ ; (c)  $C_D = 5$ ; (d)  $C_D = 50$ .

pressure error was cut down from 6.3 % to around 0.5 %, the error of the gravity contribution from 10.3 % to around 1.5 % and the error of the viscosity contribution from 33.3 % to between 3.5 % and 4.1 %. For  $C_D$  equal to 50 and 500 the errors become higher, for  $C_D = 500$  they are close to the ones obtained with the homogenous model.

**Table 2: Comparison between the theoretical pressures and the pressures obtained from the simulations, at  $x = 0$  (inlet), at  $t = 0.35$  s. The errors relative to the theoretical values are shown inside brackets.**

	$P^{\text{inhom}}$	$P^{\text{inhom}}(\text{grav})$	$P^{\text{inhom}} - P^{\text{inhom}}(\text{grav})$
Theory	573.7	355.3	218.4
	$P^{\text{CFX}}$	$P^{\text{CFX}}(\text{grav})$	$P^{\text{CFX}} - P^{\text{CFX}}(\text{grav})$
$C_D = 0.05$	570.2 (-0.6 %)	360.7 (+1.5 %)	209.5 (-4.1 %)
$C_D = 0.5$	571.1 (-0.4 %)	360.3 (+1.4 %)	210.8 (-3.5 %)
$C_D = 5$	570.6 (-0.5 %)	361.0 (+1.6 %)	209.5 (-4.1 %)
$C_D = 50$	555.4 (-3.2 %)	368.7 (+3.8 %)	186.8 (-14.5 %)
$C_D = 500$	537.4 (-6.3 %)	376.1 (+5.9 %)	161.4 (-26.1 %)

The evolutions with time of the inlet pressure obtained from simulations ( $P^{\text{CFX}}@Inlet$ ) and of its theoretical value ( $P^{\text{inhom}}@Inlet$ ) obtained from equation (93), are shown in Fig. 14a-14d. The error of the theoretical value according to the CFX inhomogeneous model, where the air hydrostatic pressure and the air viscous effects are neglected, relative to the full theoretical value ( $P_{in}$ ) obtained by equation (55), defined as:

$$\text{error1} = \frac{P_{in} - P^{\text{inhom}}@Inlet}{P_{in}} \quad (96)$$

and the error of the inlet pressure obtained from simulation, relative to the inhomogeneous model theoretical value, defined as:

$$\text{error2} = \frac{P^{\text{inhom}}@Inlet - P^{\text{CFX}}@Inlet}{P^{\text{inhom}}@Inlet} \quad (97)$$

are also presented.

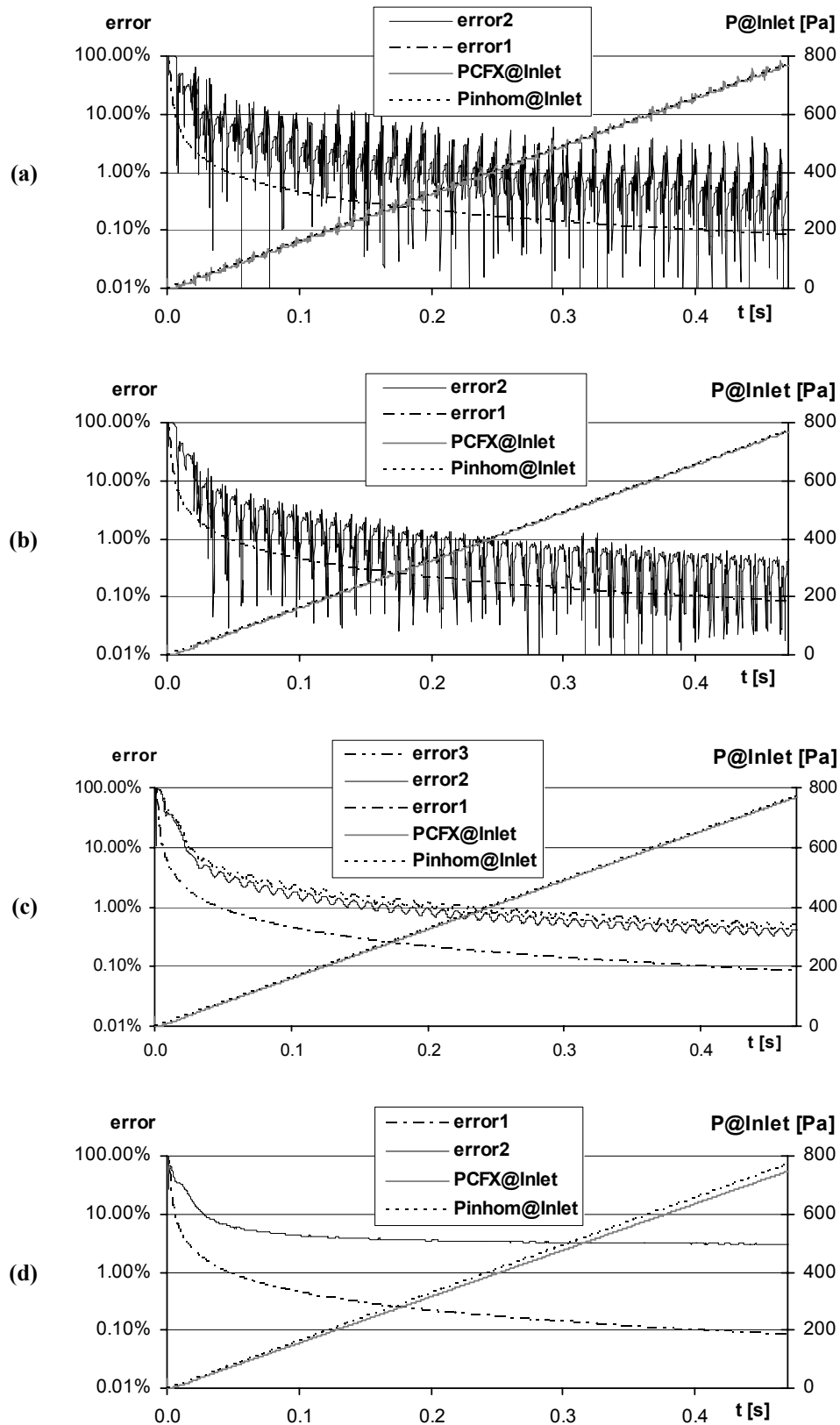


Fig. 14: Evolution with time of the inlet pressure obtained from simulation and of its theoretical value.  
 (a)  $C_D = 0.05$ ; (b)  $C_D = 0.5$ ; (c)  $C_D = 5$ ; (d)  $C_D = 50$ .

For  $C_D = 0.05$  and  $C_D = 0.5$ , it is possible to observe that, although the pressure obtained from CFX follows the theoretical value, it oscillates around the theoretical value. The oscillations of the curve error2 are well visible in Fig. 14a-14b.

These time oscillations are very probably related to the spatial oscillations at the flow front region shown in Fig. 13a-13d. Indeed, lower values of  $C_D$  show higher oscillations both on Fig. 13a-13d and on Fig. 14a-14d.

For  $C_D = 5$ , the pressure obtained from CFX and the theoretical one are nearly superposed. For  $t = 0.032$  s error2 becomes smaller than 5 %, and for  $t = 0.15$  s smaller than 1 %.

In Fig. 14c the error of the inlet pressure obtained from CFX relative to the full theoretical model value:

$$\text{error3} = \frac{P_{\text{in}} - P^{\text{CFX}} @ \text{Inlet}}{P_{\text{in}}} = \text{error1} + \text{error2} - \text{error1} \times \text{error2} \quad (98)$$

is also shown. However, the curve relative to error2 is nearly the same as the one relative to error3, meaning that the error introduced by the inhomogeneous model may be regarded as irrelevant.

For  $C_D = 5$ , the oscillation of the curve error2 is not as evident as for  $C_D = 0.05$  or  $C_D = 0.5$ , but it is still present. And, it is interesting to note that the period of this oscillation,  $T(\text{error2})$ , corresponds to the period at which the flow front crosses the mesh elements.

$$T(\text{error2}) = \frac{\Delta x}{U} \quad (99)$$

where  $\Delta x$  represents the x direction length of the mesh elements.

In Fig. 15, the computation time to complete 0.47 s of simulation, for the four different values of  $C_D$ , is shown:

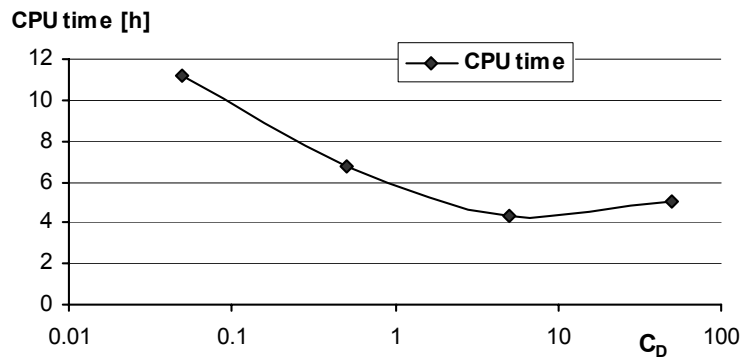


Fig. 15: Computation time for the simulations to complete 0.47 s.

For  $C_D = 0.05$ , the necessary computing time is nearly 2.6 times longer than for  $C_D = 5$ . This occurs because, due to the observed oscillations in pressure for the smallest values of  $C_D$ , the number of iterations to achieve the convergence target within each time step is larger than for  $C_D = 5$ .

From all these presented results, it becomes clear that the value of  $C_D = 5$ , among the five analysed values, is the most suitable for this filling process.

## 2.3 Conclusions

The homogeneous multiphase flow model, which is the appropriate one to simulate free surface flows, would supposedly be the appropriate one to simulate filling processes, where the two phases are completely stratified and the interface is well defined. However, it was shown that it is unable to give acceptable results for the case under analysis, the filling of a thin space, which is the typical situation in any kind of injection moulding process.

The problem was overcome with the implementation of the inhomogeneous model, together with the no-slip boundary condition for the resin phase and the free-slip condition for the air phase. As it was shown, the fact that the air shear stress on the walls is not taken into account causes an insignificant error, as the air is considerably less viscous than the RIM resins.

Five simulations with five different values for the drag coefficient,  $C_D$ , were performed, of which  $C_D = 5$  revealed to be the most suitable one. The error of the obtained inlet pressure with this value, for  $t = 0.35$  s, is merely 0.5 % relatively to theory.

Nevertheless, an important question remains unanswered: would this be also the most suitable drag coefficient value for different meshes (different elements size and different elements aspect ratio), different time steps, different thicknesses, different inlet velocities or different material properties? However a very large amount of work would be necessary to show how this “ideal” value varies with all these variables.





## 3 Simulation of the curing process

---

### 3.1 The cure reaction

The key issue of the RIM process is the chemical reaction between the two or more liquid components, causing the mixture to polymerize. This chemical reaction, the so called cure of the resin, is described by a Kamal-type equation [94]:

$$\frac{dC}{dt} = S_C = \left(k_1 + k_2 \cdot C^m\right) \cdot (1-C)^n \quad (100)$$

where  $k_1$  and  $k_2$  have an Arrhenius dependence on temperature, as follows:

$$k_1 = A_1 \cdot e^{\left(-\frac{E_1}{R \cdot T}\right)} \quad (101)$$

$$k_2 = A_2 \cdot e^{\left(-\frac{E_2}{R \cdot T}\right)} \quad (102)$$

and where  $C$  is the degree of cure,  $T$  the absolute temperature,  $R$  the universal gas constant and  $A_1$ ,  $A_2$ ,  $E_1$ ,  $E_2$ ,  $m$  and  $n$  are model parameters.

The cure reaction leads to an increase of the mixture viscosity, which is expressed by [5, 39]:

$$\mu = A_\mu \cdot e^{\left(\frac{E_\mu}{R \cdot T}\right)} \cdot \left(\frac{C_g}{C_g - C}\right)^{A+B \cdot C} \quad (103)$$

where  $C_g$  is the gel, or solidification, point of the mixture, and  $A_\mu$ ,  $E_\mu$ ,  $A$  and  $B$  are model parameters. Obviously, equation (103) is meaningless for  $C \in [C_g, 1]$ .

The reaction is exothermic, and the heat rate released per unit volume is proportional to the rate of cure, and given by:

$$\dot{Q}_R = Q_t \cdot S_C \quad (104)$$

where  $Q_t$  is total volumetric amount of heat produced by the complete reaction.

The degree and the rate of cure play, therefore, an important role in the whole RIM process, as exemplified in Fig. 16. Consequently, numerical errors involving the degree of cure will give rise to errors involving all the other variables, even if these are numerically obtained with accuracy. CFX is a code designed to deal mainly with fluid flow and heat

transfer, and does not have any implemented model of the cure reaction; the degree of cure has to be implemented as an additional variable.

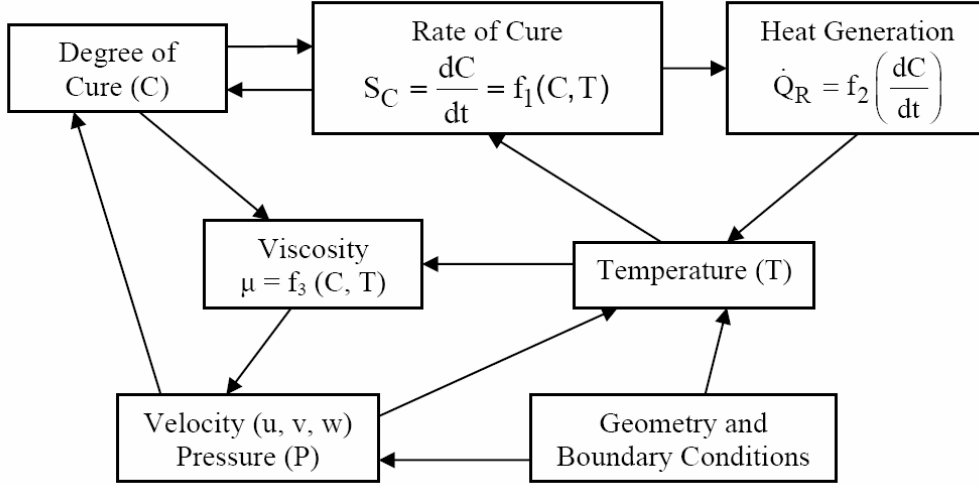


Fig. 16: Influence of the degree and rate of cure in the RIM process.

### 3.2 Physical model

As the molecular diffusion for the RIM materials is very low,  $\sim 10^{-11} \text{ m}^2/\text{s}$  [39], the cure is dominated by the reaction and convection terms:

$$\frac{\partial(r_\alpha \cdot \rho_\alpha \cdot C)}{\partial t} + \nabla \cdot (r_\alpha \cdot \rho_\alpha \cdot C \cdot \vec{U}) = r_\alpha \cdot \rho_\alpha \cdot S_C \quad (105)$$

where  $S_C$  is the rate of cure given by equation (100), and  $\alpha$  refers to the liquid (resin) phase.

### 3.3 Numerical models

Equation (105) is integrated over each control volume, and discretely represented as:

$$\frac{\partial}{\partial t} \left( \int_V r_\alpha \cdot \rho_\alpha \cdot C \, dV \right) + \sum_{ip} \dot{m}_{\alpha ip} \cdot C_{ip} = \overline{r_\alpha \cdot \rho_\alpha \cdot S_C} \cdot V \quad (106)$$

where  $\dot{m}_{\alpha ip}$  is the discrete mass flow of phase  $\alpha$  through a face of the finite volume, given by equation (89).

The transient term may be approximated by the first order Euler transient scheme as:

$$\frac{\partial}{\partial t} \left( \int_V r_\alpha \cdot \rho_\alpha \cdot C \, dV \right) \approx V \cdot \frac{r_\alpha \cdot \rho_\alpha \cdot C - r_\alpha^0 \cdot \rho_\alpha^0 \cdot C^0}{\Delta t} \quad (107)$$

or by the second order Euler transient scheme as:

$$\frac{\partial}{\partial t} \left( \int_V r_\alpha \cdot \rho_\alpha \cdot C \, dV \right) \approx \frac{V}{\Delta t} \cdot \left\{ \frac{1}{\theta \cdot (1 + \theta)} \cdot \left[ (2 + \theta) \cdot \theta \cdot r_\alpha \cdot \rho_\alpha \cdot C - (1 + \theta)^2 \cdot r_\alpha^0 \cdot \rho_\alpha^0 \cdot C^0 + r_\alpha^{00} \cdot \rho_\alpha^{00} \cdot C^{00} \right] \right\} \quad (108)$$

where  $\theta$  is the quotient between the old and the new time step, defined by equation (36).

The degree of cure,  $C$ , at the integration points is obtained by:

$$C_{ip} = C_{up} + \beta \cdot (\nabla C \cdot \bar{R}) \quad (109)$$

where  $C_{up}$  is the value of the degree of cure at the upwind node,  $\nabla C$  is its gradient,  $\bar{R}$  is the vector from the upwind node to ip, and  $\beta$  is a blend factor. The high resolution scheme computes  $\beta$  locally to be as close as possible to 1 without violating boundedness principles [83]. The compressive differencing scheme allows  $\beta$  to be greater than 1, but reducing it as much as necessary to still maintain boundedness [85].

In CFX a source term  $S_\phi$  is linearised as:

$$S_\phi = S_{\phi v} + S_{\phi p} \cdot (\phi - \phi_{n-1}) \quad (110)$$

where  $S_{\phi v}$  is the source value and  $S_{\phi p}$  the linear source coefficient, both obtained from the previous iteration, and  $\phi_{n-1}$  the value of  $\phi$  also from the previous iteration. As convergence is approached,  $(\phi - \phi_{n-1})$  approaches zero and the value of  $S_{\phi p}$  becomes irrelevant and does not affect accuracy of the converged solution. However, it may improve convergence and stability. It should always be less or equal to zero and be set to the value [83]:

$$S_{\phi p} = \frac{\partial S_{\phi v}}{\partial \phi} \quad (111)$$

If this linearization coefficient is positive, even if the neighbour coefficients are positive, the centre point coefficient can become negative. Computationally, it is essential to keep  $S_{\phi p}$  negative so that instabilities and physically unrealistic solutions do not arise. Physically, a positive  $S_{\phi p}$  implies that, as  $\phi$  increases, the source term increases, which, if a removal mechanism is not present, will lead to an increase of  $\phi$ , and so on [95].

### 3.4 Case study

The case under study is the one-dimensional (and isothermal) filling of a space initially filled with air, with “fictitious” water entering with an inlet velocity of 0.1 m/s. The densities of the water and air are  $997 \text{ kg/m}^3$  and  $1.185 \text{ kg/m}^3$ , respectively. The rate of cure is chosen to be given simply by:

$$S_C = k \cdot (1 - C) \quad (112)$$

The geometry, mesh and boundary and initial conditions are shown in Fig. 17.

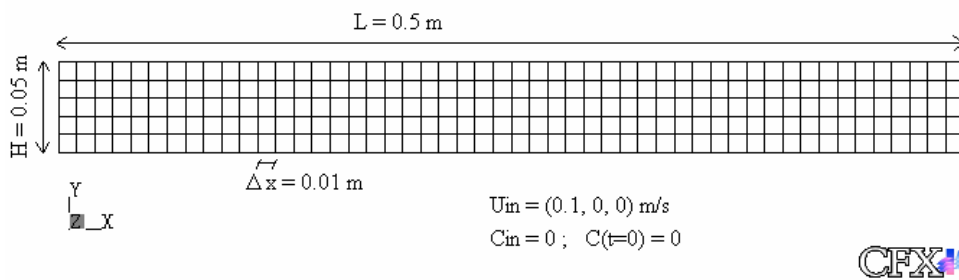


Fig. 17: Geometry, mesh and boundary and initial conditions.

To simulate the one-dimensional filling process, the top and bottom boundaries are set as free-slip walls.

Equation (105) may also be written as:

$$\frac{d(r_\alpha \cdot \rho_\alpha \cdot C)}{dt} = r_\alpha \cdot \rho_\alpha \cdot S_C \quad (113)$$

and taking into account the mass conservation equation, equation (69), leads to:

$$\frac{dC}{S_C} = dt \quad (114)$$

Integrating equation (114) between  $t = 0$  and  $t = t_R$ ,  $t_R$  representing the time of residence, with the condition  $C = 0$  for  $t = 0$ , leads to:

$$C = 1 - e^{(-k \cdot t_R)} \quad (115)$$

The time of residence is given, for the liquid phase, by:

$$t_R = \frac{x}{u} \quad (116)$$

and for the air phase, by:

$$t_R = t \quad (117)$$

The value of  $k$  was chosen to be 0.921, so that when the flow front reaches the position  $x = 0.5$  m, the value of  $C$  is 0.99.

For  $t = 4$  s, the value of  $C$  as function of  $x$ , obtained with equations (115), (116) and (117), is shown in Fig. 18. The vertical dashed line indicates the flow front position.

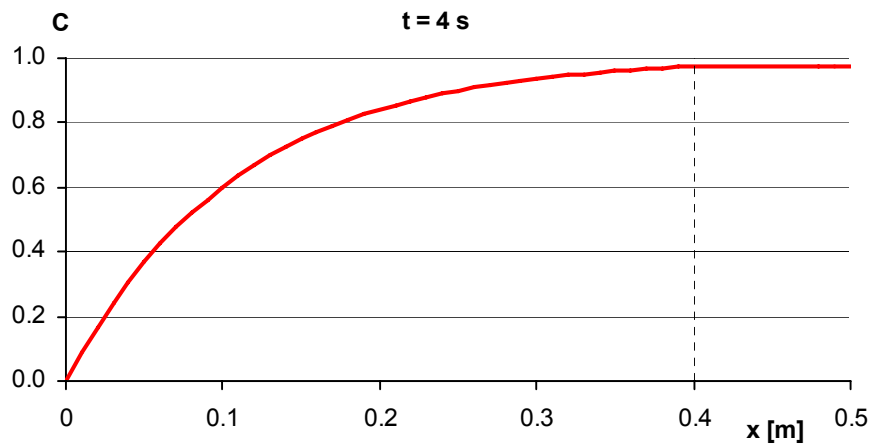


Fig. 18: Analytical value of  $C$  for  $t = 4$  s.

The simulations were performed with three different Courant numbers, which is expressed as:

$$Cr = \frac{u \cdot \Delta t}{\Delta x} \quad (118)$$

and with the combinations of the first order Euler transient scheme (TrSc1) or the second order Euler transient scheme (TrSc2) and the high resolution advection scheme (HR) or the compressive advection scheme (Comp), for the discretization of the cure equation. The definition of the compressive advection scheme for the cure equations has to be done by editing the CFX Command Language (CCL) file.

The residuals convergence target which shall be achieved by all equations is  $10^{-5}$ , up to a maximum of 50 iterations within each time step.

Initially there were problems in obtaining acceptable values of the degree of cure,  $C$ . After consulting the CFX technical services, it was found that the cause was an inconsistency in the discretization of the volume fraction multiplier in the source and the transient terms in the cure equation, in CFX-5.6. The problem was overcome with a *custom solver* provided by the CFX technical services. This problem has been fixed in the most recent versions of the code.

The degree of cure,  $C$ , obtained from simulations is represented, for  $x$  between 0.3 m and 0.5 m, in Fig. 19a-19c.

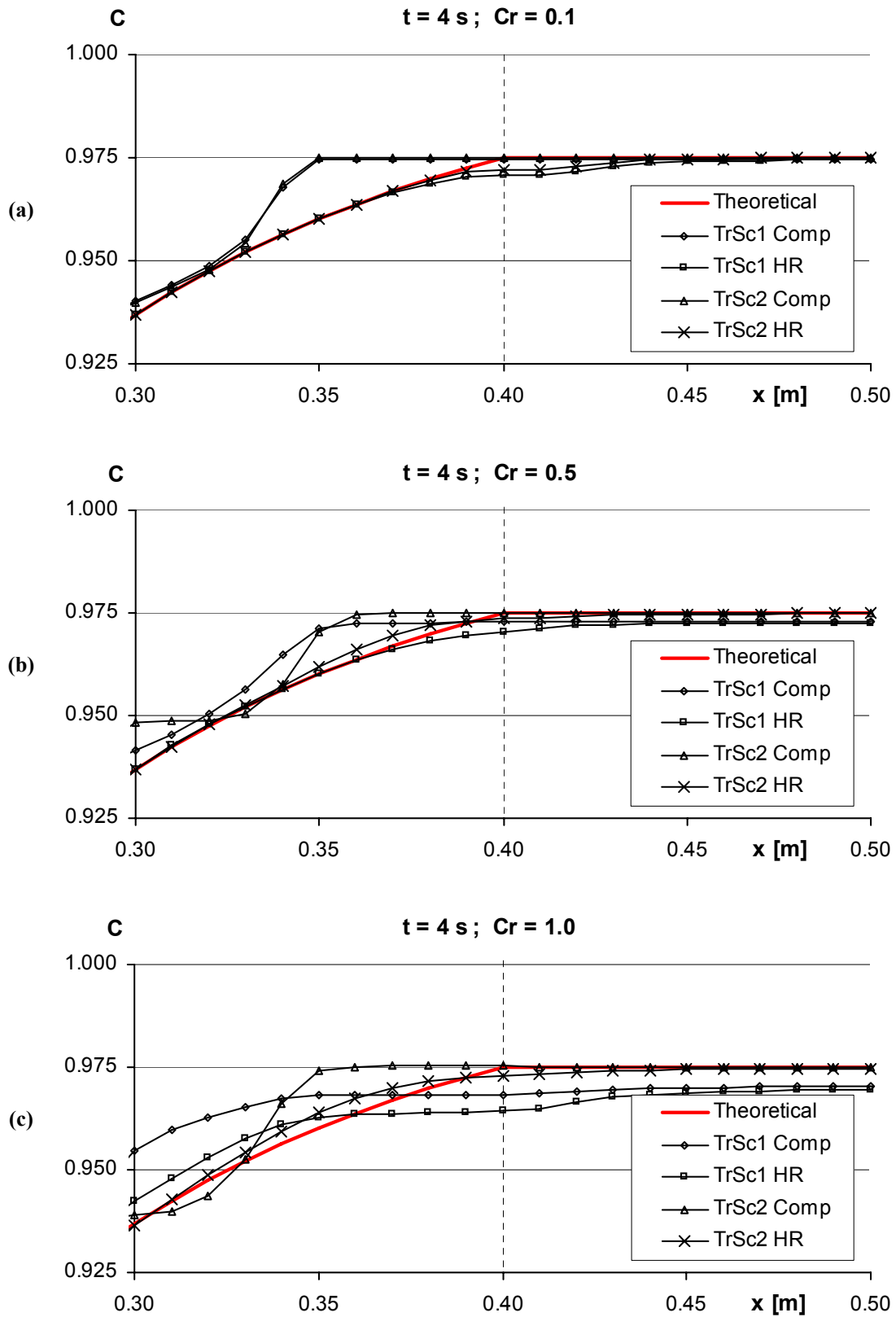


Fig. 19: Values of C, for x between 0.3 and 0.5, obtained from simulations.  
 (a)  $Cr = 0.1$ ; (b)  $Cr = 0.5$ ; (c)  $Cr = 1.0$ .

The error defined as:

$$\text{Error} = \frac{C - C_{\text{theor}}}{C_{\text{theor}_{\text{max}}}} \quad (119)$$

where  $C$  designates the values from numerical simulations,  $C_{\text{theor}}$  the theoretical values obtained with equations (115), (116) and (117), and  $C_{\text{theor}_{\text{max}}}$  the maximum theoretical value of  $C$  at the instant  $t$ , is represented in Fig. 21a-21c.

From these figures, Fig. 21a-21c, one observes that: the compressive advection scheme creates artificial gradients on the values of  $C$ ; for  $Cr = 0.1$  the results obtained with the first and the second order transient schemes become analogous and; for all the three Courant numbers the best results are obtained with the combination of the second order Euler transient scheme with the high resolution advection scheme.

With these discretization schemes, simulations were performed in another mesh, consisting of tetrahedral mesh elements instead of hexahedral elements, as shown in Fig. 20b.

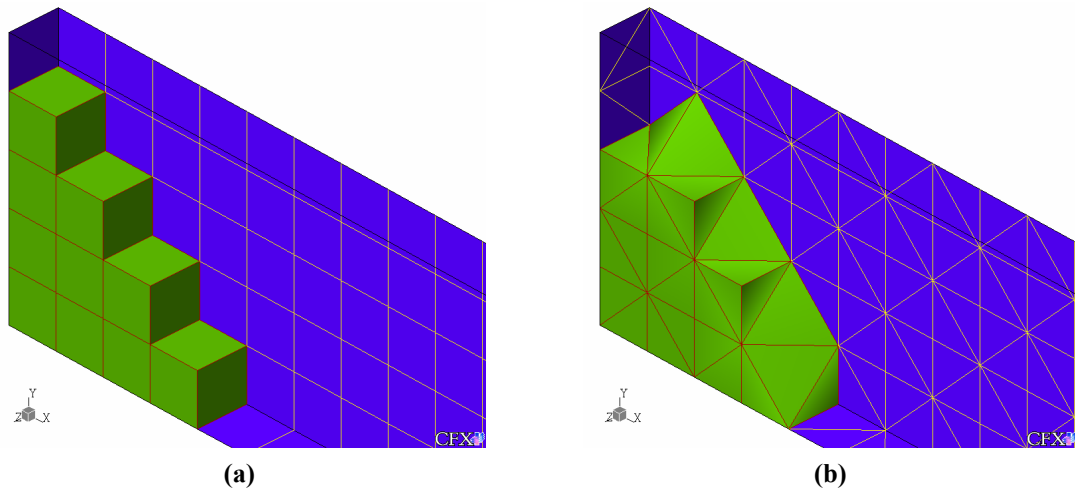


**Fig. 20: Meshes used for simulations.**

(a) meshA, formed by hexahedral elements; (b) meshB, formed by tetrahedral elements.

MeshA is the one used for the previous simulations, and meshB has exactly the same nodes as meshA, but it is formed by tetrahedral elements.

**Table 3: Characteristics of each mesh.**

	Nr. of mesh nodes	Nr. of mesh elements	Type of mesh elements
meshA	612	250	Hexahedral
meshB	612	1250	Tetrahedral

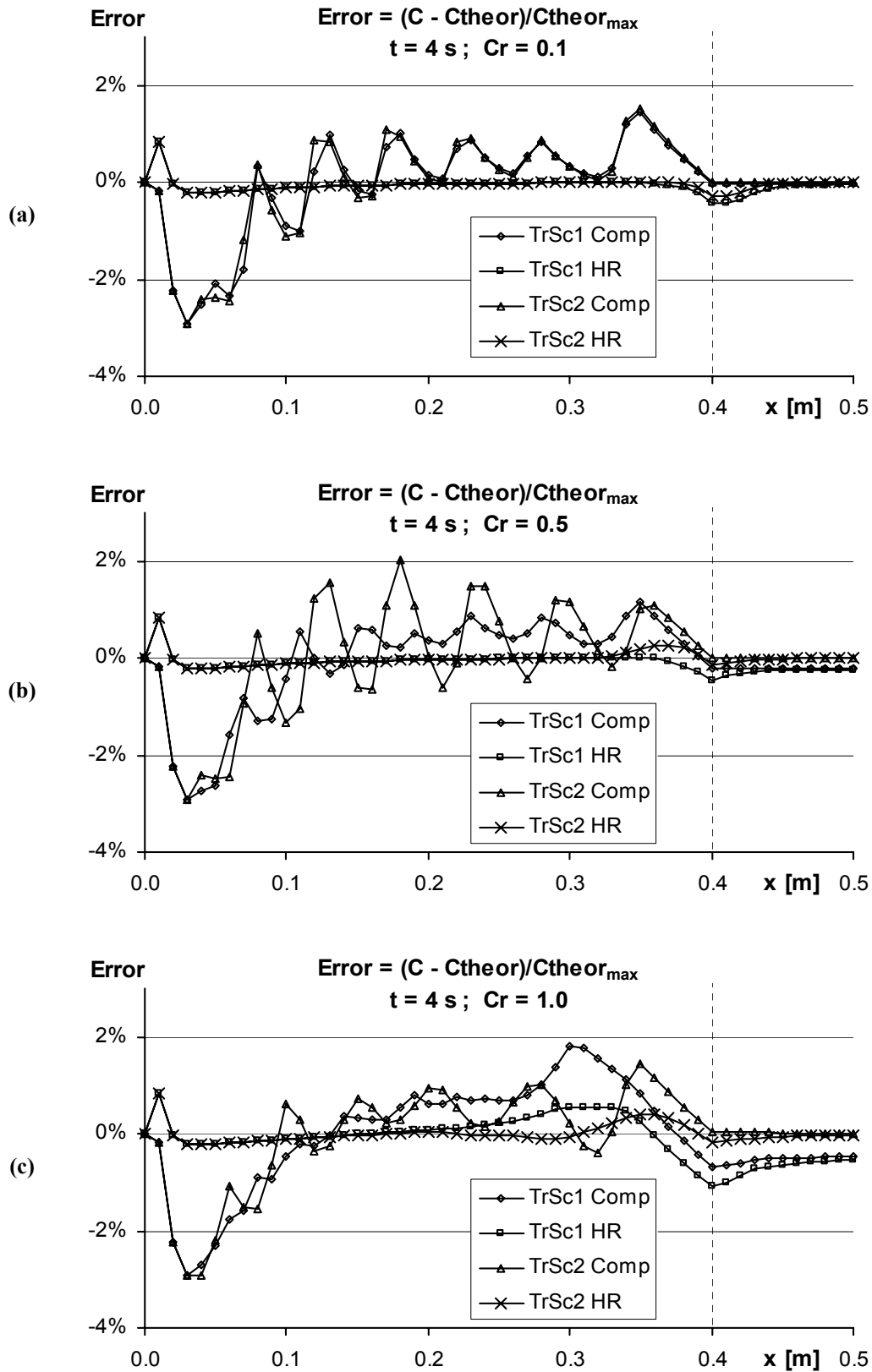


Fig. 21: Error of the values of  $C$  obtained from numerical simulations.

(a)  $Cr = 0.1$ ; (b)  $Cr = 0.5$ ; (c)  $Cr = 1.0$ .



Errors obtained with both meshes and  $Cr = 0.5$ , are represented in Fig. 22. Despite the fact that the two meshes have exactly the same nodes, because the mesh elements are different, the integration points are not the same and therefore the results differ. The error from meshA, where the hexahedral elements are aligned with the velocity vectors, is lower than the error from meshB.

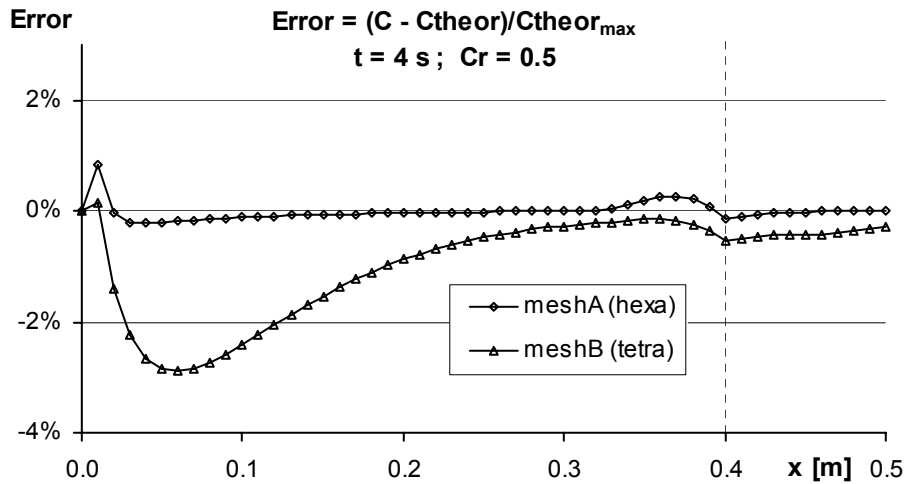


Fig. 22: Errors obtained from both meshes.

### 3.5 Conclusions

CFX does not have any implemented model to solve the cure equation, which may, although, be modelled as a transient convection-source equation for an additional variable representing the degree of cure,  $C$ . However, as it is not a standard equation, various discretization schemes were tested, and the combination of the second order Euler transient scheme with the high resolution advection scheme revealed to be the most accurate to approximate the values of  $C$  at the integration points.

It was also shown that the results obtained with a mesh made up of hexahedral elements aligned with the velocity vector, are considerably more accurate than those obtained with a mesh containing exactly the same nodes but formed by tetrahedral elements.



## 4 Simulation of the RIM filling and curing stages

### 4.1 The energy equation

As mentioned at the end of Section 1, the objective of this work is to simulate the RIM filling and curing stages using the CFX software package. The filling stage is characterized by the simultaneous motion, cure and energy equations, after which, when the injection of resin has stopped and the material velocities inside the mould fall to zero, the pure curing stage, characterized by only the cure and energy equations, takes place.

Up to this point, only the motion and cure equations were focused, but in this section also the energy equation is taken into consideration.

#### 4.1.1 Physical model

It has been shown in this work, that only the inhomogeneous model produces accurate results for the filling of thin spaces. Therefore it will be used to model the filling stage.

The conservation of mass and momentum equations were already described by equations (69) to (76), in Section 2. The cure is described by equation (105), in Section 3. The energy equation for phase  $\alpha$  (resin) may be obtained by applying the First Law of Thermodynamics to an infinitesimal control volume, leading to [92]:

$$\begin{aligned} \frac{\partial(\mathbf{r}_\alpha \cdot \rho_\alpha \cdot \text{htot}_\alpha)}{\partial t} - \mathbf{r}_\alpha \cdot \frac{\partial \mathbf{p}}{\partial t} + \nabla \cdot (\mathbf{r}_\alpha \cdot \rho_\alpha \cdot \text{htot}_\alpha \cdot \overline{\mathbf{U}}_\alpha) = \\ \nabla \cdot (\mathbf{k}_\alpha \cdot \nabla T_\alpha) + W_{v\alpha} + S_{E\alpha} \end{aligned} \quad (120)$$

where  $k_\alpha$  represents the resin thermal conductivity,  $W_{v\alpha}$  the viscous work,  $S_{E\alpha}$  heat sources, and  $\text{htot}_\alpha$  the total enthalpy defined as:

$$\text{htot}_\alpha = h_\alpha + 0.5 \cdot \overline{\mathbf{U}}_\alpha \cdot \overline{\mathbf{U}}_\alpha = u_\alpha + \frac{p}{\rho_\alpha} + 0.5 \cdot \overline{\mathbf{U}}_\alpha \cdot \overline{\mathbf{U}}_\alpha \quad (121)$$

and  $u_\alpha$  is the internal energy.

As for multiphase situations, which is the case, CFX-5.6 does not model the viscous and pressure work neither the kinetic energy effects, the full energy equation becomes simply the thermal energy equation [83]:

$$\frac{\partial(r_\alpha \cdot \rho_\alpha \cdot h_\alpha)}{\partial t} + \nabla \cdot (r_\alpha \cdot \rho_\alpha \cdot h_\alpha \cdot \overline{U_\alpha}) = \nabla \cdot (k_\alpha \cdot \nabla T_\alpha) + S_{E\alpha} \quad (122)$$

For incompressible fluids, the enthalpy is expressed solely in terms of temperature [92]:

$$h_\alpha = h_{\text{ref}} + c_\alpha \cdot (T_\alpha - T_{\text{ref}}) \quad (123)$$

where  $c_\alpha$  is the specific heat, and ref indicates a reference state for enthalpy evaluation (the default reference state in CFX is:  $h_{\text{ref}} = 0$  J/kg for  $T_{\text{ref}} = 0$  K [83, 92]). No distinction is made between  $C_{p\alpha}$  and  $C_{v\alpha}$ , as for incompressible fluids:

$$C_{p\alpha} = C_{v\alpha} = c_\alpha \quad (124)$$

The heat source,  $S_{E\alpha}$ , is given by:

$$S_{E\alpha} = r_\alpha \cdot \dot{Q}_R = r_\alpha \cdot Q_t \cdot S_C \quad (125)$$

An energy equation for phase  $\beta$  (air), similar to equation (122) but without a heat source term, could also be modelled, what would allow the implementation of a symmetric extra term in each energy equation, the interphase heat transfer, representing the heat transfer between the phases at their interface. However, mainly because, except for the first instants, the interface area is significantly small compared to the contact area between the resin and the walls, but also because the air thermal conductivity is typically smaller than that of RIM resins, the heat transfer between the resin and the air will be insignificant compared to the heat transfer between the resin and the walls, and consequently the interphase heat transfer term can be omitted on the energy equation of the resin without a foreseen loss of accuracy. Due to this, and as the air temperature is not an important issue, there is no need to model an energy equation for the air.

In the most recent versions of CFX, CFX-5.7 and ANSYS CFX 10.0, it is already possible to use the full energy equation for multiphase flows [92, 93]. Although, as previously mentioned, for typical RIM situations the viscous work can be neglected [39, 80], and the kinetic energy effects are only important for high speed flows. Therefore equation (122) is perfectly valid to model the energy balance in RIM.

#### 4.1.2 Numerical model

As all the other equations, the energy equation for phase  $\alpha$  is integrated over each control volume. It is then discretely represented as [83, 96]:

$$\begin{aligned} \frac{\partial}{\partial t} \left( \int_V r_\alpha \cdot \rho_\alpha \cdot h_\alpha \, dV \right) + \sum_{ip} \dot{m}_{\alpha ip} \cdot h_{\alpha ip} = \\ \sum_{ip} \left[ k_\alpha \cdot \left( \frac{\partial T}{\partial x} \cdot n_x + \frac{\partial T}{\partial y} \cdot n_y + \frac{\partial T}{\partial z} \cdot n_z \right) \cdot A \right]_{ip} + \overline{r_\alpha} \cdot \dot{Q}_R \cdot V \end{aligned} \quad (126)$$

The transient term, as in all the equations except the volume fraction equations, is approximated by the second order Euler transient scheme as:

$$\begin{aligned} \frac{\partial}{\partial t} \left( \int_V r_\alpha \cdot \rho_\alpha \cdot h_\alpha \, dV \right) \approx \frac{V}{\Delta t} \cdot \left\{ \frac{1}{\theta \cdot (1 + \theta)} \cdot \right. \\ \left. \left[ (2 + \theta) \cdot \theta \cdot r_\alpha \cdot \rho_\alpha \cdot h_\alpha - (1 + \theta)^2 \cdot r_\alpha^0 \cdot \rho_\alpha^0 \cdot h_\alpha^0 + r_\alpha^{00} \cdot \rho_\alpha^{00} \cdot h_\alpha^{00} \right] \right\} \end{aligned} \quad (127)$$

where  $\theta$ , the quotient between the old and the new time steps, is obtained from equation (36).

On the advection term, the discrete mass flow of phase  $\alpha$ ,  $\dot{m}_{\alpha ip}$ , is obtained from equation (89), and  $h_{\alpha ip}$ , from equation (39), being the blend factor  $\beta$  computed according to the high resolution advection scheme. On the diffusion term, the temperature derivatives at the integration points are evaluated making use of shape functions as indicated in equation (38).

## 4.2 Case study 1

### 4.2.1 Case description

The work presented in [39], as already mentioned in Section 1.2, has been considered by many authors as a benchmark solution. It is used also in this work, in this section (Case study 1) and in Section 4.3 (Case study 2), as a benchmark solution to validate the results produced by CFX when simulating the whole RIM model, consisting of the mass, momentum, volume fractions, cure and energy equations.

In this Case study 1, the experimental system 9/21/1 conducted by [39] is used. This system was also numerically modelled in [39, 72].

The mould is a simple rectangularly shaped mould, placed vertically, with a full gate at the bottom, as shown in Fig. 23. Its dimensions, together with the filling conditions, are indicated in Table 4.

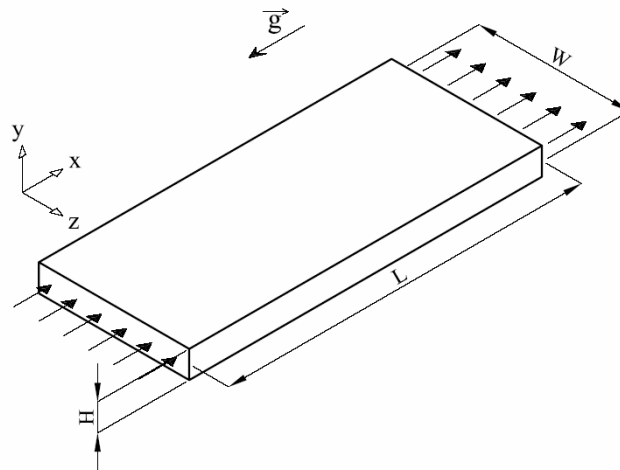


**Fig. 23: Mould geometry.**

**Table 4: Mould dimensions and filling conditions [39].**

L	Length	0.505	[m]
W	Width	0.101	[m]
H	Thickness	$3.2 \times 10^{-3}$	[m]
$Q_{in}$	Inlet flow rate	$3.35 \times 10^{-5}$	[m <sup>3</sup> /s]
$T_{in}$	Inlet temperature	55.3	[°C]
$T_w$	Walls temperature	82.0	[°C]

The chemical system used was a RIM type polyurethane, whose density and thermal properties, assumed being constant, are specified in Table 5.

**Table 5: Density and thermal properties of the chemical system [39].**

$\rho$	Density	1000	[kg/m <sup>3</sup> ]
$C_p$	Specific heat	1880	[J/(kg·K)]
$k$	Thermal conductivity	0.17	[W/(m·K)]

A second order cure kinetics is assumed to describe the chemical reaction. The kinetic parameters are indicated in Table 6.

**Table 6: Kinetic parameters of the chemical system [39].**

$k_o$	Pre-exponential factor in cure equation	$36 \times 10^3$	[m <sup>3</sup> /(mol·s)]
E	Reaction activation energy	$57.8 \times 10^3$	[J/mol]
$C_{OH_0}$	Initial concentration of reactive species	$2.6 \times 10^3$	[mol/m <sup>3</sup> ]
$H_R$	Heat of reaction	$83 \times 10^3$	[J/mol]

Therefore, for this resin the rate of cure,  $S_C$ , is given by:

$$\frac{dC}{dt} = S_C = k_o \cdot C_{OH_0} \cdot e^{\left(\frac{-E}{R \cdot T}\right)} \cdot (1-C)^2 \quad (128)$$

and the released heat rate per unit volume of resin,  $Q_R$ , by:

$$\dot{Q}_R = Q_t \cdot S_C = H_R \cdot C_{OH_0} \cdot S_C = H_R \cdot k_o \cdot C_{OH_0}^2 \cdot e^{\left(\frac{-E}{R \cdot T}\right)} \cdot (1-C)^2 \quad (129)$$

The rheological parameters, necessary for the viscosity equation (103) are given in Table 7.

**Table 7: Rheological parameters of the chemical system [39].**

$A_\mu$	Pre-exponential factor in viscosity equation	$4.1 \times 10^{-8}$	[kg/(m·s)]
$E_\mu$	Viscosity activation energy	$38.3 \times 10^3$	[J/mol]
$C_g$	Solidification (gel) point	0.85	[ ]
A	Constant in viscosity equation	4.0	[ ]
B	Constant in viscosity equation	-2.0	[ ]

The filling time,  $t_f$ , is the mould volume divided by the volumetric inlet flow rate:

$$t_f = \frac{H \cdot W \cdot L}{Q_{in}} = 4.87 \text{ s} \quad (130)$$

#### 4.2.2 Numerical issues

As the mould width is much larger than its thickness ( $W/H \approx 32$ ), the side walls effect may be neglected, and a two-dimensional simulation may be performed without important loss of accuracy.

Due to symmetry, only half of the geometry was modelled. As convergence problems arise when the flow front gets close to the outlet boundary, the calculation domain length was extended to 0.52 m instead of the 0.505 m mould length. The problem was run with two different meshes, both with 208 elements on the longitudinal direction, each 2.5 mm long, by 5 elements on the transverse direction in Mesh 1, Fig. 24a, and 10 elements in Mesh 2, Fig. 24b.

The inhomogeneous model is used, together with the walls no-slip boundary condition for the liquid (resin) phase equations and the free-slip condition for the air phase equations.

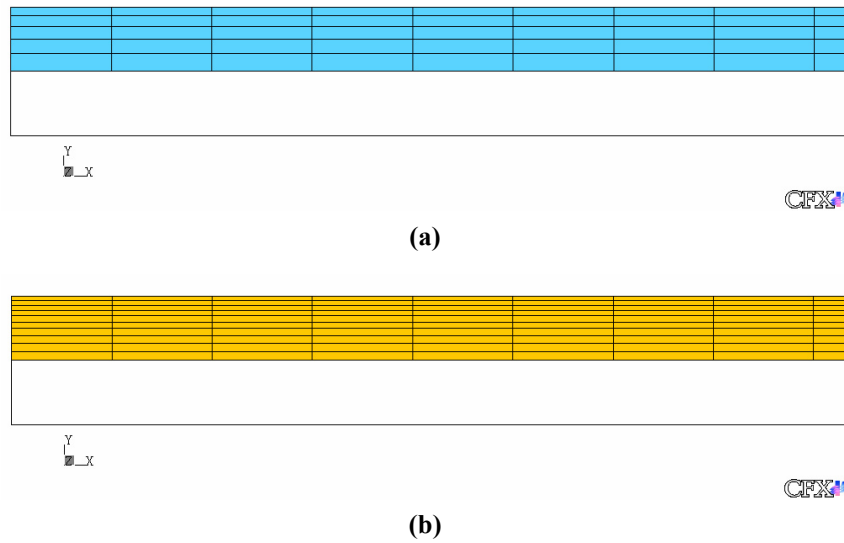


**Fig. 24: Detail of the meshes used to model the process. (a) Mesh 1: five mesh elements on the transverse direction; (b) Mesh 2: ten mesh elements on the transverse direction.**

At the inlet a parabolic velocity profile is imposed, with an average velocity of:

$$U_{\text{in}} = \frac{Q_{\text{in}}}{H \cdot W} \approx 0.1037 \text{ m/s} \quad (131)$$

resulting in a Reynolds number of 13, according to equations (40) and (41) and based on the resin viscosity at the inlet temperature and zero conversion,  $5.05 \times 10^{-2} \text{ kg/(m}\cdot\text{s)}$ . At the outlet, the boundary condition is zero pressure.

The reference density is that of the air,  $1.185 \text{ kg/m}^3$ . The resin volume fraction is 1 at the inlet and zero at the outlet. It is assumed that the mixture has not reacted before it enters the mould, and therefore the condition of zero degree of cure is imposed at the inlet.

For the energy equation, the boundary conditions are the temperatures indicated in Table 4. In CFX, the energy flow by diffusion at an inlet boundary is assumed to be negligible when compared to advection, and equated to zero [83].

The imposed initial conditions all over the domain are fluids at rest, pressure equal to zero, temperature equal to  $T_{\text{in}}$  and, due to the mould being initially filled with air, the initial resin and air volume fractions are 0 and 1, respectively.

At the end of the filling stage the inlet velocity is reduced to zero in a time interval of 0.01 s, corresponding only to 0.2% of the filling time, via a third-order polynomial as represented in Fig. 25. This is more realistic than a sharp step or a ramp function, and guarantees the temporal continuity of the term  $\partial u / \partial t$  in the momentum equations. A lower order polynomial would cause a discontinuity in this term, leading to a discontinuity of  $\partial p / \partial x$  and therefore a discontinuity of the inlet pressure which is physically unrealistic.



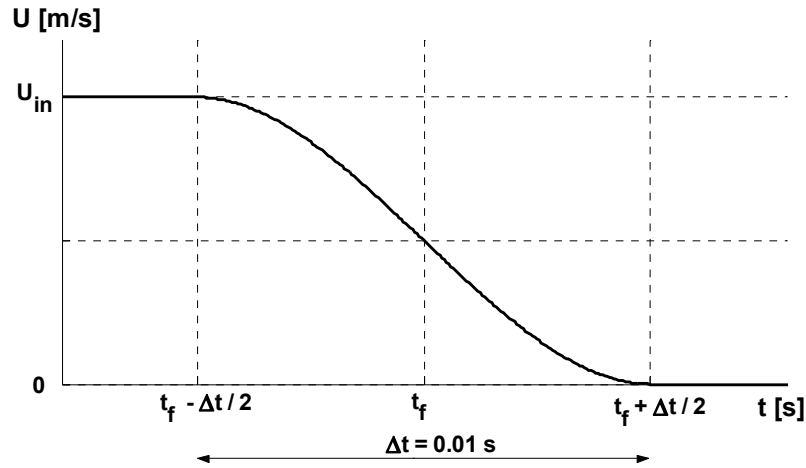


Fig. 25: Inlet velocity reduced to zero, via a third-order polynomial, at the end of the filling stage.

According to equations (110) and (111), the source term in the cure equation was linearised as:

$$S_C = S_{Cv} + S_{Cp} \cdot (C - C_{n-1}) \quad (132)$$

where the source value,  $S_{Cv}$ , was set to:

$$S_{Cv} = k_o \cdot C_{OHo} \cdot e^{\left(\frac{-E}{R \cdot T}\right)} \cdot (1 - C)^2 \quad (133)$$

and the linear source coefficient,  $S_{Cp}$ , which is always negative, to:

$$S_{Cp} = \frac{\partial S_{Cv}}{\partial C} = -2 \cdot k_o \cdot C_{OHo} \cdot e^{\left(\frac{-E}{R \cdot T}\right)} \cdot (1 - C) \quad (134)$$

The source term in the energy equation could also be linearised relatively to temperature in a similar way:

$$S_E = S_{Ev} + S_{Ep} \cdot (T - T_{n-1}) \quad (135)$$

where the source value,  $S_{Ev}$ , would be:

$$S_{Ev} = r_\alpha \cdot H_R \cdot k_o \cdot C_{OHo}^2 \cdot e^{\left(\frac{-E}{R \cdot T}\right)} \cdot (1 - C)^2 \quad (136)$$

and the linear source coefficient,  $S_{Ep}$ :

$$S_{Ep} = \frac{\partial S_{Ev}}{\partial T} = \frac{E}{R \cdot T^2} \cdot r_\alpha \cdot H_R \cdot k_o \cdot C_{OHo}^2 \cdot e^{\left(\frac{-E}{R \cdot T}\right)} \cdot (1 - C)^2 \quad (137)$$

However, as the source coefficient,  $S_{Ep}$ , would always be positive, the source term was not linearised and only the source value,  $S_{Ev}$ , was used.

The time step is  $4 \times 10^{-4}$  s, and the maximum number of iterations within each time step is 50. Three simulations were run with Mesh 1, with the residuals convergence target set to  $10^{-3}$ ,  $10^{-4}$  and  $10^{-5}$ . With Mesh 2 only one simulation was performed, with the residuals convergence target set to  $10^{-5}$ . Note that, as previously mentioned, the convergence criterion for the volume fraction equations is automatically set by CFX to 10 times the specified convergence target.

All the governing equations kept being solved up to  $t = 4.95$  s, and after this instant the fluids are assumed to be completely at rest and only the energy and the cure equations are solved. Note that when the velocity at the inlet boundary is zero, the energy flows by diffusion and by advection are equated to zero, corresponding consequently to an adiabatic boundary.

The computation times, in hours, to perform the four simulations are shown in Fig. 26. The steep lines correspond to the filling stage when all the equations are solved, while the low slope lines correspond to the curing stage when only the cure and the energy equations are solved and the convergence target is achieved in only one or two iterations within each time step.

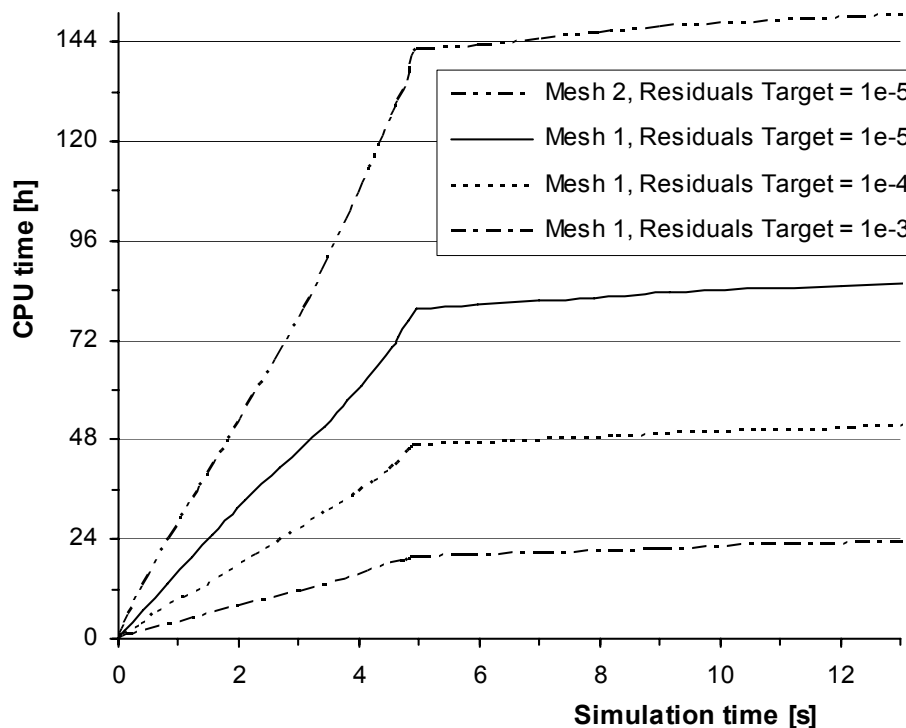
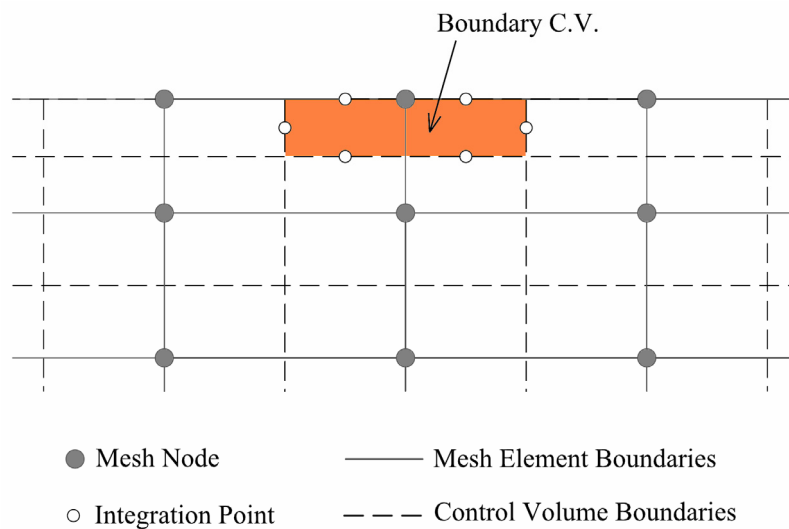


Fig. 26: Computation time versus simulation time.

### 4.2.3 Results

All the presented results, in this and in the next case studies, were obtained with conservative variable values, which are, actually, the results produced by the CFX-Solver. That is, a variable value on a boundary node is not precisely equal to the specified boundary condition (the boundary conditions are imposed on the integration points laying on the boundary), and instead it represents the average variable value in the control volume surrounding that node [83], Fig. 27. This seems to be more correct than using hybrid variable values, obtained by taking the results produced by the CFX-Solver and over-writing them on the boundary nodes with the specified boundary conditions [83].



**Fig. 27: Two-dimensional representation of a boundary control volume.**

All the results, except when the contrary is mentioned, were obtained with Mesh 1 and with the residuals convergence target set to  $10^{-5}$ .

In Fig. 28a-28e the degree of cure, and in Fig. 29a-29e the temperature, are represented at five different instants: at  $t = 3$  s (during the filling stage), at  $t = 4.87$  s (the end of the filling stage), at  $t = 6.8$  s (when the maximum temperature is observed), at  $t = 9$  s and at  $t = 15$  s.

Note that because of the length of the mould being much bigger than its thickness, the longitudinal and transverse directions are represented at different scales in order to be possible to properly visualize the results.

At the end of the filling stage, the maximum value of the degree of cure is 0.79, which is close to the degree of cure at which the resin solidifies (gel or solidification point),  $C_g = 0.85$ , and the highest temperature is  $151.6$  °C. At  $t = 6.8$  s, the maximum temperature during the whole process,  $177.9$  °C, is achieved, and the resin which ended up

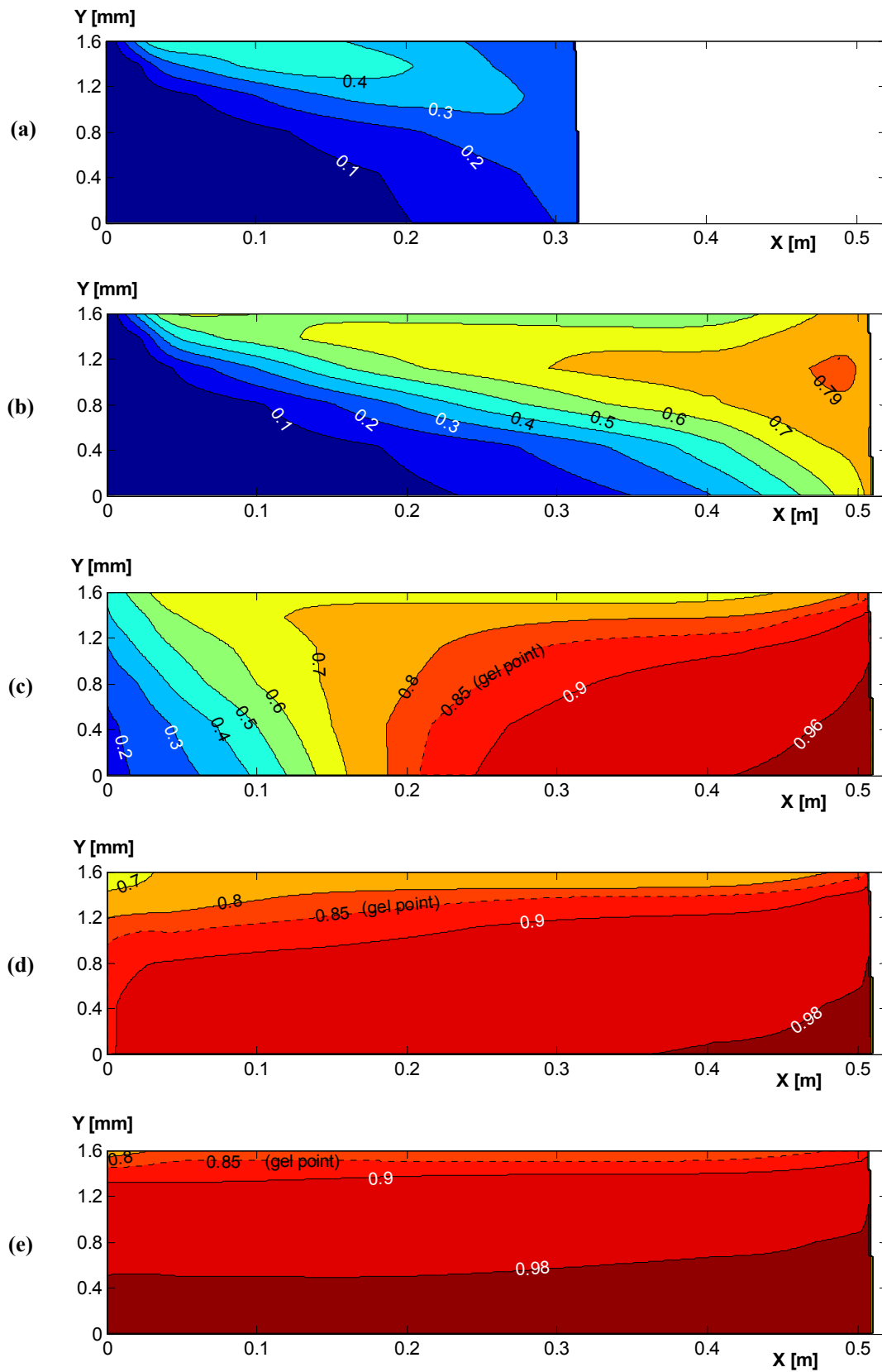


**Fig. 28: Degree of cure. (a)  $t = 3$  s; (b)  $t = 4.87$  s, when the filling stage ends; (c)  $t = 6.8$  s; (d)  $t = 9$  s; (e)  $t = 15$  s. (Figure not to scale).**

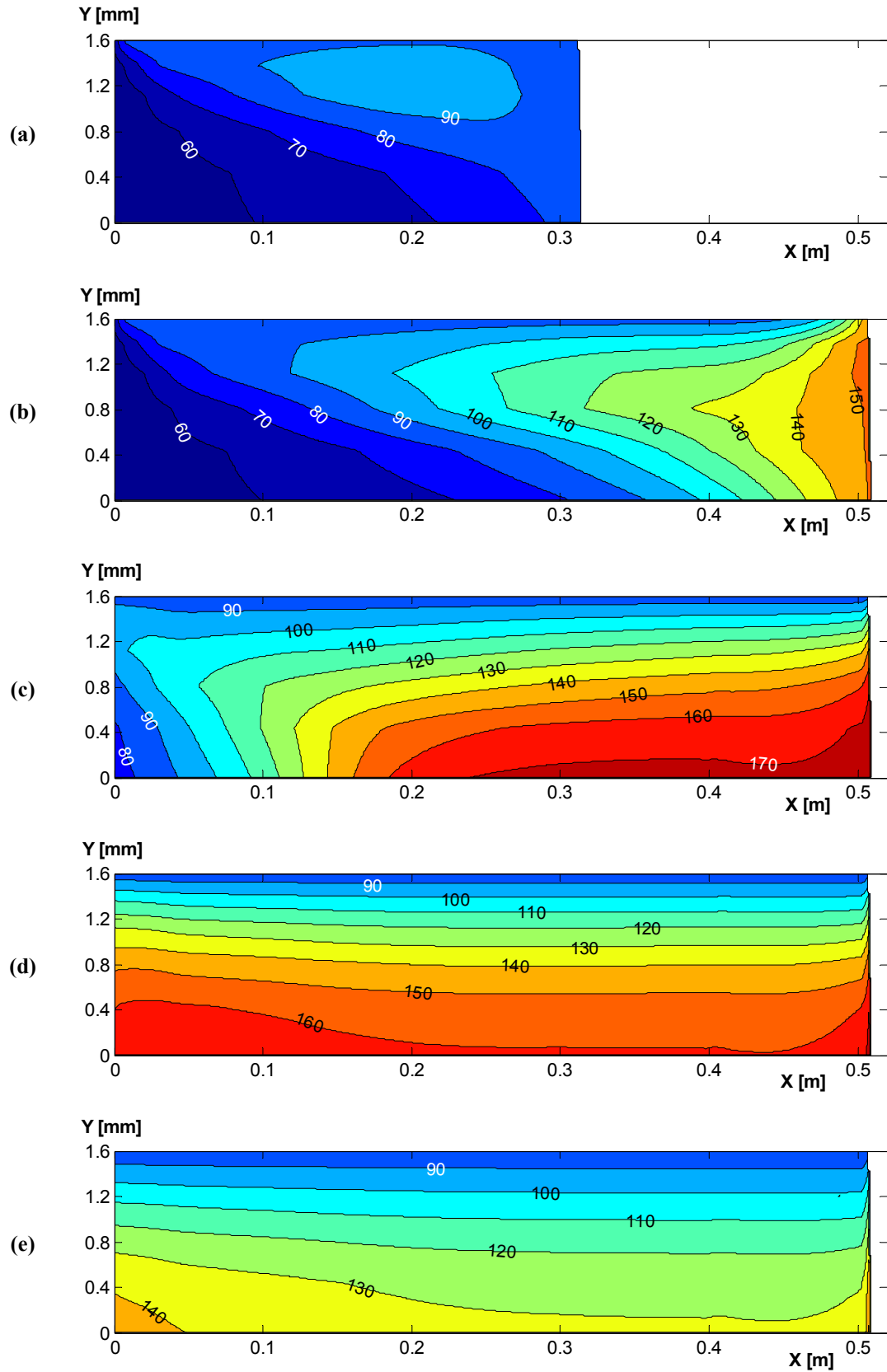


Fig. 29: Temperature [°C]. (a)  $t = 3$  s; (b)  $t = 4.87$  s, when the filling stage ends; (c)  $t = 6.8$  s, when the maximum temperature (177.9 °C) is observed; (d)  $t = 9$  s; (e)  $t = 15$  s. (Figure not to scale).

at the forward centre part of the mould (about 42 %) has already solidified. At  $t = 9$  s and at  $t = 15$  s, the temperature contour lines are nearly parallel to the mould walls, indicating that at these instants the most important energetic process is heat conduction from the mould centre to the walls. About 81 % of the resin has already solidified at  $t = 9$  s, and 93 % at  $t = 15$  s, remaining just a thin layer next to the mould walls yet to solidify.

In Fig. 29b, the use of conservative temperature values is well visible. The resin temperature next to the wall near to the flow front,  $\sim 140$  °C, is quite above the wall temperature, 82 °C. This is due to the fountain flow: at the flow front the fluid on the centre part of the mould at high temperature moves towards the walls. This behaviour is mentioned in [2] as “thermal shock”, and it also happens at the beginning of the filling stage when the resin temperature is lower than the mould walls temperature. It is characteristic of various injection moulding processes, and results in high fluid temperature gradients next to the mould walls.

The minimum value of the degree of cure at each instant is presented in Fig. 30. It corresponds, for  $t$  below 8.1 s to the degree of cure at the centre position of the inlet ( $x, y = 0, 0$  [mm]), and for  $t$  above 8.1 s to the degree of cure at the location of the inlet in contact with the mould walls ( $x, y = 0, 1.6$  [mm]). This can also be observed in Fig. 28b-28d ( $t = 6.8$  s,  $t = 9$  s and  $t = 15$  s), and it occurs because the temperature at the mould walls is always 82 °C and therefore the cure reaction is isothermal, while at the inlet centre the cure reaction is nearly adiabatic and the temperature is 55.3 °C during the filling stage but increasing during the curing stage up to 167 °C at  $t = 9.7$  s.

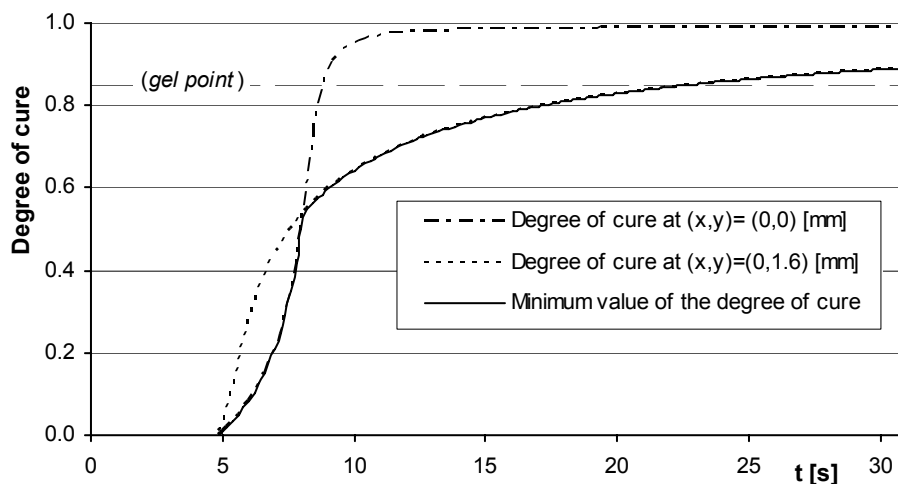
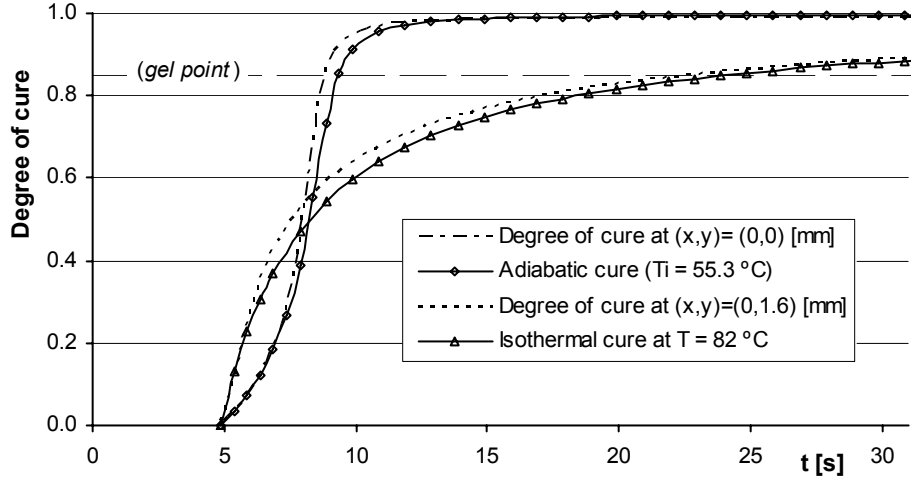


Fig. 30: Minimum value of the degree of cure along the time.

According to the simulation, the totality of the resin has solidified 22.8 s after the injection of resin has started.

In Fig. 31, the degree of cure at those points is compared with the degree of cure obtained by an adiabatic cure reaction with an initial temperature equal to  $T_{in}$ , 55.3 °C, and by an isothermal cure reaction at a temperature equal to  $T_w$ , 82 °C.



**Fig. 31: Comparison of the degree of cure at  $(x, y) = (0, 0)$  [mm] and at  $(x, y) = (0, 1.6)$  [mm] with the degree of cure obtained by an adiabatic cure reaction and by an isothermal cure reaction.**

The curve for the isothermal cure reaction is obtained by integrating equation (128) for a constant temperature, with the initial condition  $C = 0$  for  $t = t_f$ , which leads to:

$$C = 1 - \frac{1}{1 + k_o \cdot C_{OHo} \cdot e^{\left(\frac{-E}{R \cdot T}\right)} \cdot (t - t_f)} \quad (138)$$

where  $T$  is equal to 355.15 K (82 °C), and  $t_f$  is the filling time, 4.87 s.

The curve corresponding to the adiabatic cure reaction is obtained by integrating the energy equation (122) without the convection and diffusion terms, with the initial condition  $T = T_i$  for  $C = 0$ , where  $T_i$  is the initial temperature, which gives:

$$T = \frac{H_r \cdot C_{OHo}}{\rho \cdot C_p} \cdot C + T_i \quad (139)$$

The above expression for  $T$  is introduced in equation (128), leading to:

$$\frac{\partial C}{\partial t} = K_o \cdot C_{OHo} \cdot (1 - C)^2 \cdot e^{\left\{-E / \left[R \cdot \left(T_i + \frac{H_r \cdot C_{OHo}}{\rho \cdot C_p} \cdot C\right)\right]\right\}} \quad (140)$$

and this last equation is numerically integrated, also with the initial condition  $C = 0$  for  $t = t_f$ .  $T_i$  is equal to  $T_{in}$ , 328.45 K (55.3 °C).

The term  $H_r \cdot C_{OH_0} / \rho \cdot C_p$  in equation (139) is known as the adiabatic temperature rise,  $\Delta T_{ad}$  [5, 39], as it corresponds to the temperature rise due to a complete adiabatic cure reaction. For this particular resin,  $\Delta T_{ad} = 114.8$  °C.

It is very interesting to notice that for an initial temperature of 55.3 °C, a complete adiabatic cure reaction would lead to a resin temperature of 170.1 °C (55.3 °C + 114.8 °C), which is below the maximum temperature observed during the whole process, 177.9 °C. This means that, although the walls temperature is significantly below these values, the part of the resin which reached that temperature had to have a positive energy transfer balance with its surroundings along its path. This may be explained partially by the walls temperature being above the resin inlet temperature, and partially by the resin distribution due to the fountain flow effect, as may be seen in Fig. 29b, where there is a gradient of temperature from “older” resin, located between the centre and the wall, to “younger” resin, located at the mould centre.

This clearly demonstrates that the adiabatic temperature rise cannot be taken as an upper limit for estimating the maximum temperature observed during the RIM process, and it attests the importance of the accurate simulation of the fountain flow behaviour and the complexity of the simultaneous flow motion, cure reaction and heat transfer processes.

From equations (138) and (140), one concludes that, for the adiabatic and for the isothermal cure reactions, the time to reach a given degree of cure is determined, besides the resin properties, by the filling time,  $t_f$ , and by the initial temperature for the adiabatic cure, or by the constant temperature for the isothermal cure.

For the resin under analysis, the time ( $t-t_f$ ) to reach the solidification point ( $C = C_g = 0.85$ ) and the time to reach the degree of cure  $C = 0.9$ , for an isothermal cure reaction are represented in Fig. 32a as function of the temperature, and for an adiabatic cure reaction in Fig. 32b as function of the initial temperature.

The curves in Fig. 32a are obtained from:

$$t - t_f = \frac{C}{(1 - C) \cdot K_0 \cdot C_{OH_0} \cdot e^{\left(\frac{-E}{R \cdot T}\right)}} \quad (141)$$

derived from equation (138), while the curves in Fig. 32b are obtained by solving numerically equation (140).

The part can be removed from the mould when the totality of the resin has reached, typically, the degree of cure  $C = 0.9$  [97, 98], such that enough molecular weight or network structure has been built. Therefore the cycle time will be determined by the longest between the isothermal and the adiabatic cure reactions times to reach that degree of cure, which, for common RIM operation temperatures, is very likely to be the one corresponding to the isothermal reaction. That is, unless the mould walls temperature,  $T_w$ , is much higher than the inlet temperature,  $T_{in}$ , the last portion of resin to solidify and to



reach the degree of cure such that the part may be removed, will be that in contact with the inlet and the mould walls.

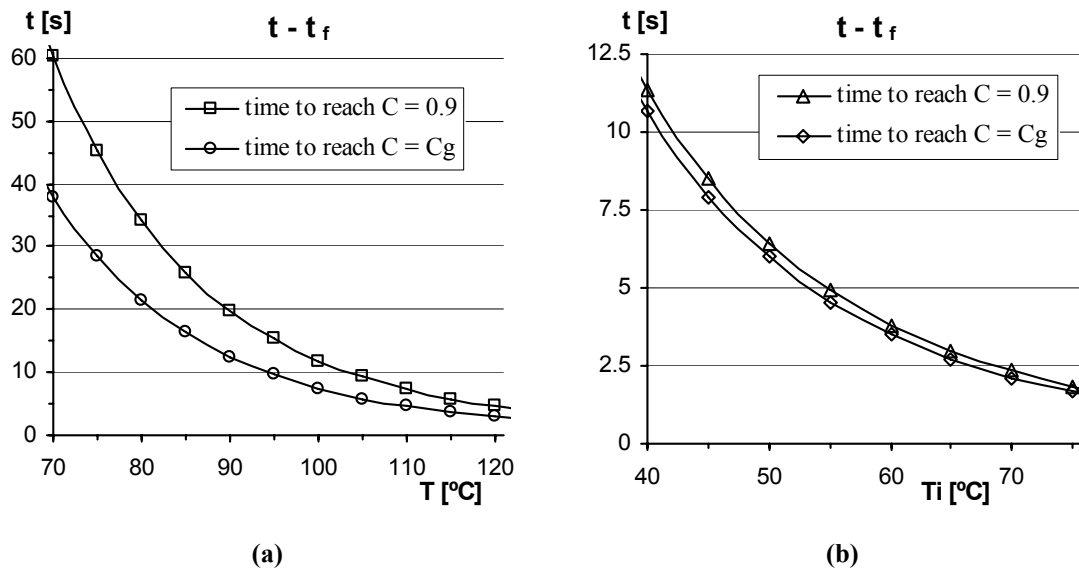


**Fig. 32: Time to reach the solidification (gel) point ( $C = C_g = 0.85$ ) and to reach  $C = 0.9$ .**  
**(a) Isothermal cure reaction at temperature  $T$ ; (b) Adiabatic cure reaction with initial temperature  $T_i$ .**

For the conditions under analysis, the part may be removed from the mould approximately 35 s (4.87 s + 30.47 s) after the injection of resin has started. This time may be considerably reduced, as can be observed in Fig. 32a, by increasing  $T_w$ . However, increasing the mould walls temperature will cause higher temperatures at the part centre, which must not exceed the polymer degradation point. A temperature of 200  $^{\circ}\text{C}$  is probably an upper limit for polyurethanes [5]. The maximum temperature during the process may only be predicted by numerical simulation.

The viscosity at the end of the filling stage is shown in Fig. 33. As the viscosity is solely a function of the degree of cure and of the temperature, as expressed by equation (103), its distribution could be foreseen by analysis of Fig. 28b and Fig. 29b: the highest values of viscosity occur where the degree of cure is higher and the temperature lower.

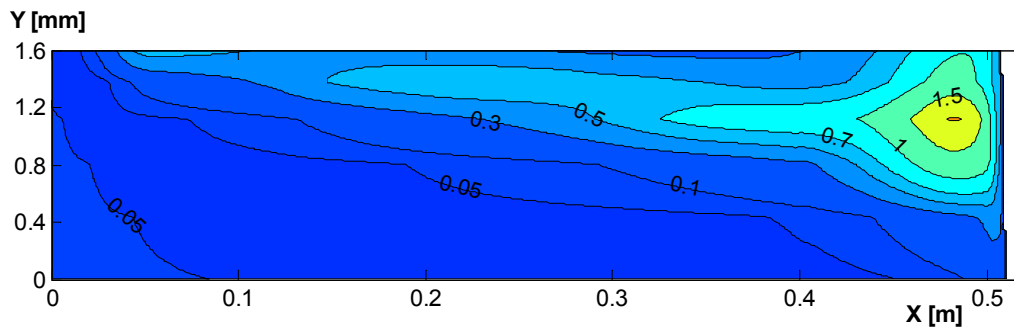


**Fig. 33: Viscosity [kg/(m·s)] at  $t = 4.87$  s, when the filling stage ends. (Figure not to scale).**

This viscosity distribution causes the pressure distribution along the longitudinal direction and its gradient represented in Fig. 34. The highest absolute values of the pressure gradient correspond obviously to the position where the highest values of viscosity are located, dropping to zero after the flow front.

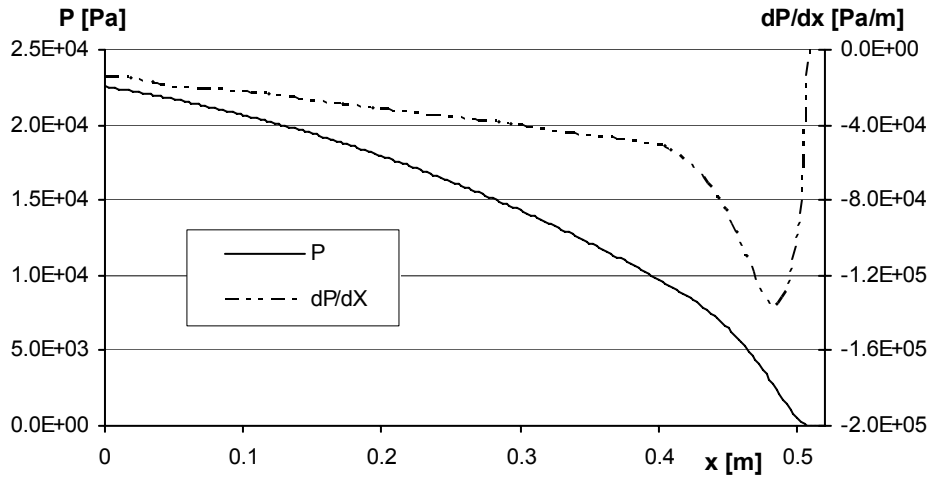


Fig. 34: Pressure distribution along the x direction, just before the end of the filling stage.

The evolution of the inlet pressure with time obtained with CFX, together with the numerical and experimental results obtained by Castro and Macosko [39], and the pressure for the case of constant viscosity, are represented in Fig. 35.

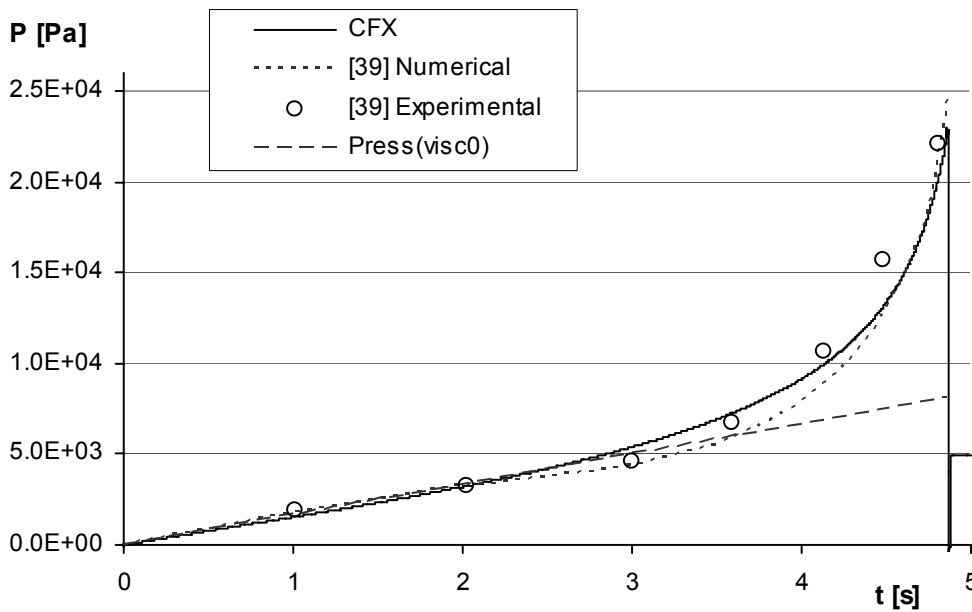


Fig. 35: Evolution of the inlet pressure with time.

The pressure for the case of constant viscosity is given by:

$$P(\text{visc0}) @ \text{inlet} = \frac{12 \cdot U_{\text{in}}^2 \cdot \mu_{\text{in}}}{H^2} \cdot t + \rho \cdot g \cdot U_{\text{in}} \cdot t \quad (142)$$

where  $\mu_{\text{in}}$  indicates the initial mixture viscosity:

$$\mu_{\text{in}} = \mu(C = 0; T = T_{\text{in}}) \approx 5.05 \times 10^{-2} \text{ kg}/(\text{m} \cdot \text{s}) \quad (143)$$

In Fig. 35, the results obtained with CFX are in good agreement with the experimental and numerical results obtained in [39].

The evolution of the inlet pressure obtained with the three residuals target values is shown in Fig. 36. The results obtained with  $10^{-5}$  and  $10^{-4}$  are practically superposed, while the results obtained with  $10^{-3}$  are somewhat different. The error of the inlet pressure obtained with the residuals target set to  $10^{-4}$  relatively to that obtained with  $10^{-5}$  is always below 1 %, and most of the time below 0.1 %, while the error of the inlet pressure obtained with  $10^{-3}$  rises above 40 % near the end of the filling stage

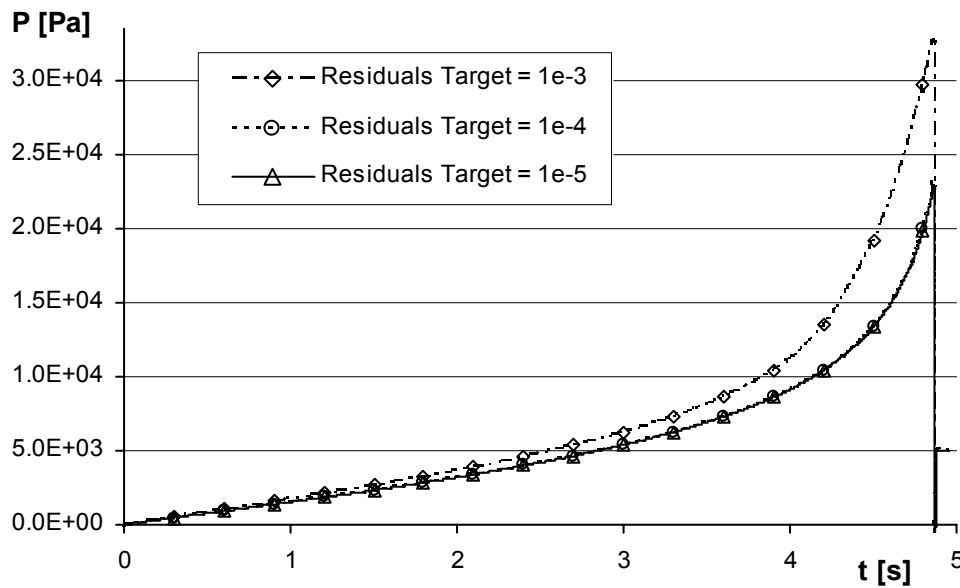


Fig. 36: Inlet pressure obtained with the different residuals target values.

The reason why for the first 3 seconds the inlet pressure follows a straight line, is that as the cure reaction takes place, the degree of cure increases, but due to the released heat also the temperature increases, leading to equilibrium in the viscosity equation. This behaviour can be seen in Fig. 37, where the degree of cure and the viscosity are represented for the case of adiabatic cure reaction with initial temperature equal to  $T_{\text{in}}$ , 55.3 °C.

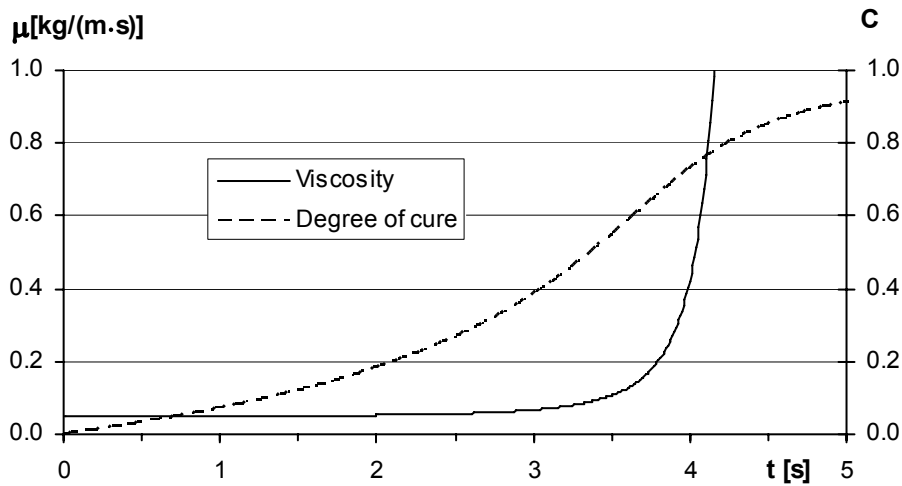


Fig. 37: Viscosity and degree of cure along the time for an adiabatic cure reaction.

The viscosity along the time, for the case of adiabatic cure reaction, with various initial temperatures, is represented in Fig. 38. The curves were obtained from equation (103), together with equation (139) and the numerical integration of equation (140).

The initial viscosity is as lower as higher are the values of  $T_i$ . However, the time when a rapid increase of viscosity is observed is as shorter as higher are the values of  $T_i$ .

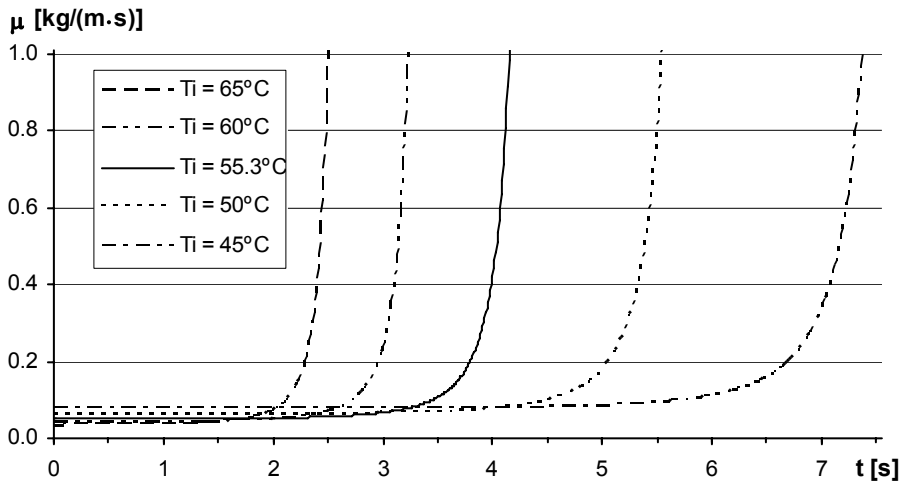
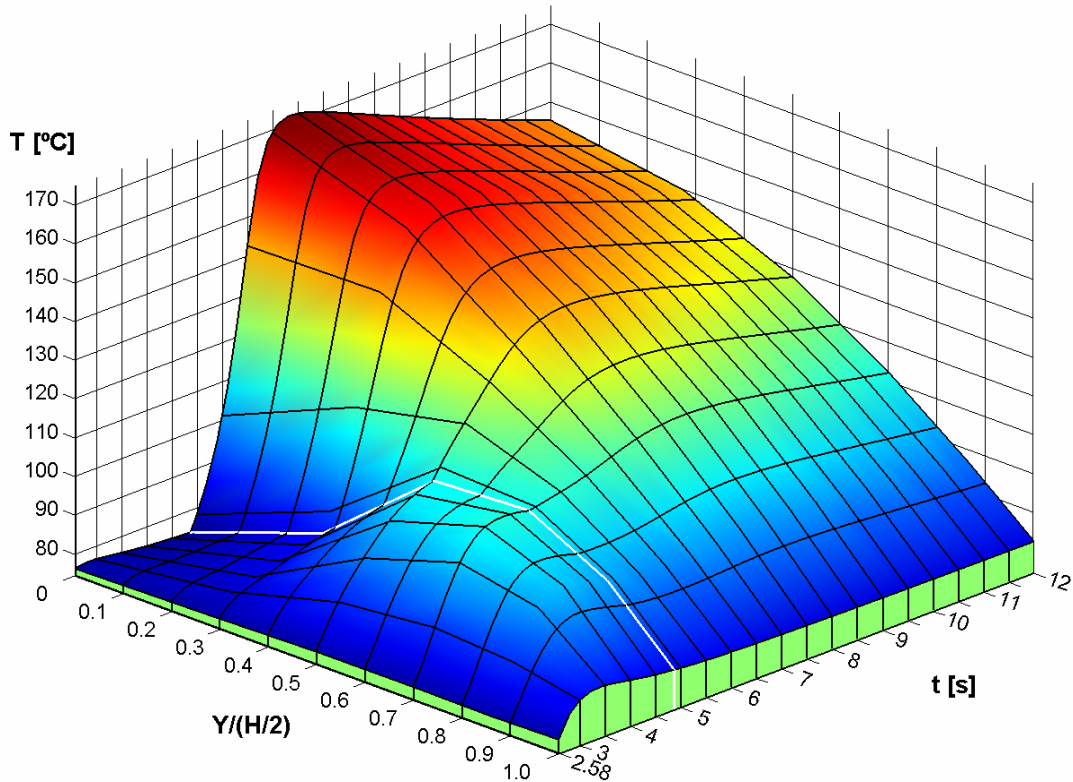


Fig. 38: Viscosity along the time for adiabatic cure reactions with various initial temperatures.

From Fig. 38, and for the mould under analysis, which is filled in 4.87 s, one may expect for an inlet temperature of 50 °C, a nearly constant viscosity ( $\mu_{in} = 6.36 \times 10^{-2}$  kg/(m.s)) during the filling stage, and hence a linear evolution of the inlet pressure along the time resulting in 8.8 KPa at the end of the filling stage, which is almost one third of the predicted inlet pressure for  $T_{in} = 55.3$  °C.

From the numerical integration of equation (140) or from Fig. 32b one concludes that, for  $T_i = 50\text{ }^\circ\text{C}$ , the time  $t-t_f$  for an adiabatic cure reaction to reach  $C = 0.9$  is 6.45 s. From equation (141) or from Fig. 32a one concludes that the necessary temperature for an isothermal cure reaction to reach that degree of cure in approximately the same time is  $112\text{ }^\circ\text{C}$  (for  $T = 112\text{ }^\circ\text{C}$ ,  $t-t_f = 6.63\text{ s}$ ). Therefore it is expected that, if the inlet and the mould walls temperatures were modified to  $50\text{ }^\circ\text{C}$  and to  $112\text{ }^\circ\text{C}$ , respectively, the time for the part may be removed would be reduced from 35 s to 11.1 s ( $4.47\text{ s} + 6.63\text{ s}$ )

Fig. 39 shows the temperature on a line between the mould centre ( $y = 0$ ) and the mould wall ( $y = H/2$ ), at  $x = 0.53L$ , during the filling and curing stages. The grid represents the temperature evolution along the time at points spaced by  $0.1 \times (H/2)$ , and temperature profiles on the  $y$ -direction at every 0.5 s.



**Fig. 39: Temperatures during filling and curing, at  $x = 0.53L \approx 0.268\text{ m}$ . The white line represents the instant when the filling stage ends ( $t = 4.87\text{ s}$ ).**

Due to the fountain flow, the temperature at the flow front is nearly uniform, and therefore when it reaches  $x = 0.53L$ , at  $t = 2.58\text{ s}$ , the temperature is almost constant along the mould thickness. Between this instant and the end of the filling stage (represented by a white line in the figure), the lowest temperature is verified at the point located in the centre plane, where the velocity and hence the energy convection term have their highest values. The maximum temperature is verified at  $y = 0.7 \times (H/2)$ .

The temperature profile at the end of the filling stage shows clearly the difficulty of capturing the temperature curvature with only five mesh elements on the thickness direction.

After the filling stage has ended and the convection terms turned into zero, the temperatures at the centre points rapidly increase, reaching the maximum approximately at  $t = 7$  s. After that, the heat lost by conduction to the mould walls is higher than the heat released by the chemical reaction, and the temperatures start to decrease.

Fig. 40 shows the comparison between the results obtained with CFX, numerical and experimental results obtained by Castro and Macosko [39], and numerical results obtained by Lo [72]. The temperatures obtained with CFX, with Mesh 1, are, for most of the time, slightly higher than all the other results, quite probably due to the five mesh elements in the mould thickness direction being unable to capture very accurately the temperature gradients on that direction, leading to underestimation of the heat conduction from the mould interior to the mould walls. This conclusion may be strengthened by the observed lower temperatures obtained with Mesh 2 (10 mesh elements on the thickness direction), which are closer to the numerical results obtained in [39]. However, as Mesh 2 has twice the mesh elements and 11/6 times the mesh nodes than Mesh 1, the computation time is nearly the double, as could be observed in Fig. 26.

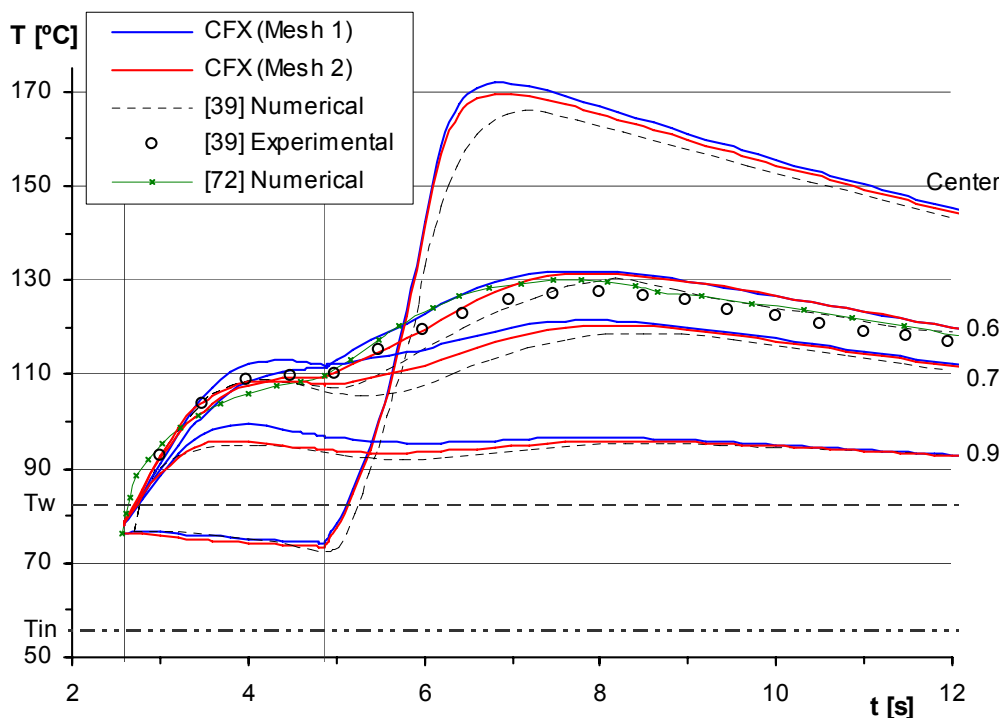


**Fig. 40:** Temperatures at  $x = 0.53L$ . Numerical results obtained with CFX, with Mesh 1 and Mesh 2, at the centre plane, at  $y/(H/2) = 0.6, 0.7$  and  $0.9$ . Numerical results obtained in [39] at the centre plane, at  $y/(H/2) = 0.6, 0.7$  and  $0.9$ . Experimental results obtained in [39] at  $y/(H/2) = 0.6$ . Numerical results obtained in [72] at  $y/(H/2) = 0.6$ .

Nevertheless, from Fig. 40 one may conclude that there is a general good agreement between the results obtained with CFX, even those obtained with Mesh 1, and the other numerical results. When compared with the experimental results at  $y/(H/2) = 0.6$ , the results obtained with CFX seem to be as good as the other numerical results.

The comparison between the temperatures obtained with the three residuals target values is shown in Fig. 41. The temperatures obtained with  $10^{-5}$  and  $10^{-4}$  are nearly superposed, while the ones obtained with  $10^{-3}$  are somewhat different.

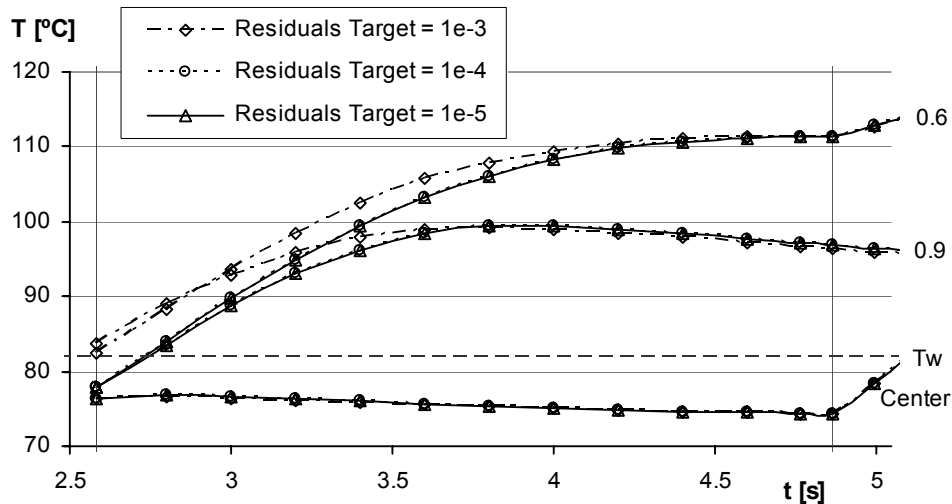


Fig. 41: Temperatures at  $x = 0.53L$ , at the centre plane, at  $y/(H/2) = 0.6$  and at  $y/(H/2) = 0.9$ , obtained with the three different residuals target values.

## 4.3 Case study 2

### 4.3.1 Case description and numerical issues

This case is the experimental system 9/21/2 conducted and numerically modelled by [39]. The mould, as in Case 1, is a simple rectangularly shaped mould with a full gate at the bottom. Its dimensions according to Fig. 23, and filling conditions are indicated in Table 8.

Table 8: Mould dimensions and filling conditions [39].

L	Length	0.487	[m]
W	Width	0.101	[m]
H	Thickness	$3.2 \times 10^{-3}$	[m]
$Q_{in}$	Inlet flow rate	$2.75 \times 10^{-5}$	[m <sup>3</sup> /s]
$T_{in}$	Inlet temperature	54.0	[°C]
$T_w$	Walls temperature	70.0	[°C]

The resin is the same as in Case 1, whose properties were reported in Tables 5-7. The filling time,  $t_f$ , is equal to:

$$t_f = \frac{H \cdot W \cdot L}{Q_{in}} = 5.72 \text{ s} \quad (144)$$

Because of the same reasons reported in Case 1, a two-dimensional simulation is performed and only the top half of the mould is modelled. The calculation mesh is Mesh 1 used in Case 1, with 5 mesh elements on the transverse direction, represented in Fig. 24a.

A parabolic velocity profile, with an average value of:

$$U_{in} = \frac{Q_{in}}{H \cdot W} \approx 0.0851 \text{ m/s} \quad (145)$$

is imposed at the inlet boundary. This results, according to equations (40) and (41), in a Reynolds number of 10, based on the resin viscosity at the inlet temperature and zero conversion,  $5.34 \times 10^{-2} \text{ kg/(m}\cdot\text{s)}$ .

The major differences between this Case 2 and Case 1 are a lower inlet flow rate, leading to a longer filling time, and the 12 °C lower walls temperature.

At  $t = t_f = 5.72 \text{ s}$  the inlet velocity is set to zero via a third-order polynomial, in a time interval of 0.01 s, as in the previous case, but all the equations keep being solved up to  $t = 5.85 \text{ s}$ . After that the fluids are assumed to be at rest and only the energy and the cure equations are solved.

All the other numerical issues, including time step, are the same as employed in Case 1. Furthermore, as in Case 1, three simulations were performed with the residuals convergence target set to  $10^{-3}$ ,  $10^{-4}$  and  $10^{-5}$ .

The computation time to perform the simulation, for each of the residuals target value, is shown in Fig. 42, where the difference between when all the equations are solved and when only the cure and the energy are solved is clear, as in Fig. 26.

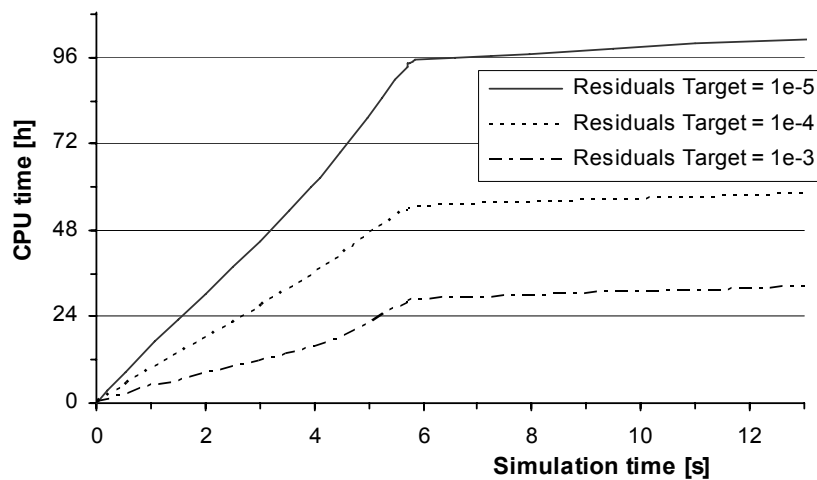


Fig. 42: Computation time versus simulation time.



### 4.3.2 Results

All the following presented results were obtained with the residuals convergence target set to  $10^{-5}$ , except when the contrary is mentioned.

The degree of cure, in Fig. 43a-43e, and the temperature in Fig. 44a-44e, are represented at five different instants: at  $t = 4$  s (during the filling stage), at  $t = 5.72$  s (at the end of the filling stage), at  $t = 7.6$  s (when the maximum temperature is observed), at  $t = 10$  s and at  $t = 15$  s. The longitudinal and transverse directions are represented at different scales in order to allow a proper visualization of the results.

According to the results obtained from the simulation, at the end of the filling stage a small portion ( $\sim 1$  %) of the resin has already solidified (the degree of cure is above 0.85), Fig. 43b. This simulation was only possible to perform by setting the maximum resin viscosity to  $10^3$  kg/(m·s). At this instant, the highest value of temperature is  $159.3$  °C. At  $t = 7.6$  s, the maximum temperature,  $179.0$  °C, is observed, and 29 % of the resin has already solidified. At  $t = 10$  s and  $t = 15$  s, the temperature contour lines are nearly parallel to the mould walls, due to the heat conduction from the mould centre to the walls, and 67 % and 84 %, respectively, of the resin has solidified.

It is curious to notice that, although the inlet and the mould walls temperatures are  $1.3$  °C and  $12$  °C, respectively, lower than in Case 1, the maximum observed temperature is  $1.1$  °C higher. This is probably due to the higher degree of cure and temperature achieved at the end of the filling stage. As in Case 1, but now the difference being bigger, the maximum temperature,  $179$  °C, is above the temperature caused by a complete adiabatic cure reaction,  $168.8$  °C ( $54.0$  °C +  $114.8$  °C).

The inlet pressure along the time obtained with CFX is represented in Fig. 45, and shows a good agreement with the experimental and numerical results obtained in [39] also shown in Fig. 45.

In Fig. 45, the dashed line indicated by *Lengthening Reactor* represents numerical results obtained in [39] neglecting the fountain flow effect, while the other dashed line represents results obtained in [39] with a fountain flow model. As CFX solves the full three-dimensional equations there is no need for any fountain flow model, but it is important to recognize that CFX is capable to model its effect even when the mesh elements longitudinal dimensions are considerably larger than their transverse dimensions as shown in Fig. 24a.

Fig. 46 shows the inlet pressure obtained with the three residuals target values. As in previous comparisons, the results obtained with  $10^{-5}$  and  $10^{-4}$  are practically superposed, while the results obtained with  $10^{-3}$  are different. But in this case the simulation performed with  $10^{-3}$ , after the premature nearly asymptotic increase of pressure, diverged.

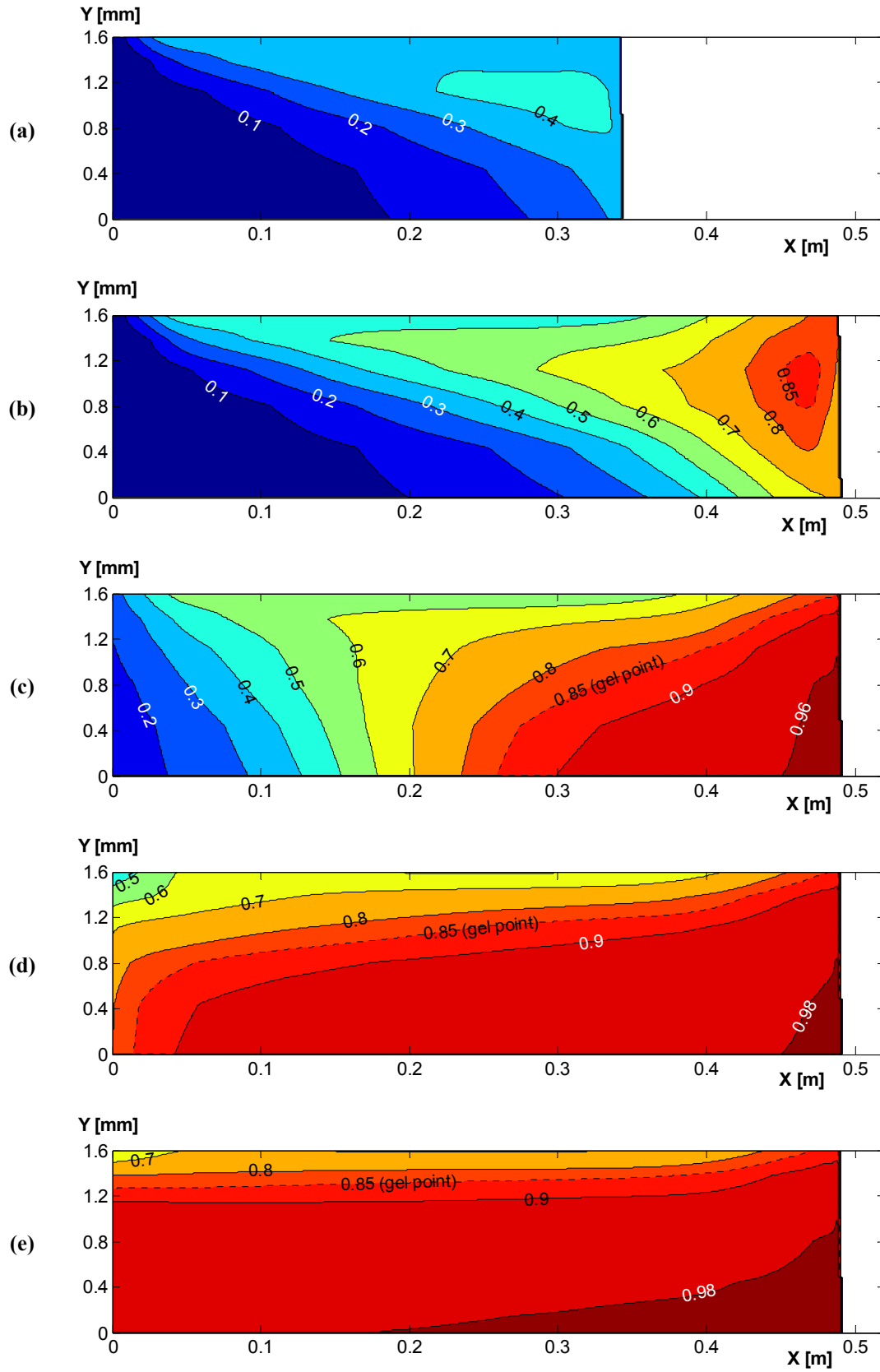


**Fig. 43: Degree of cure. (a)  $t = 4$  s; (b)  $t = 5.72$  s, when the filling stage ends; (c)  $t = 7.6$  s; (d)  $t = 10$  s; (e)  $t = 15$  s. (Figure not to scale).**

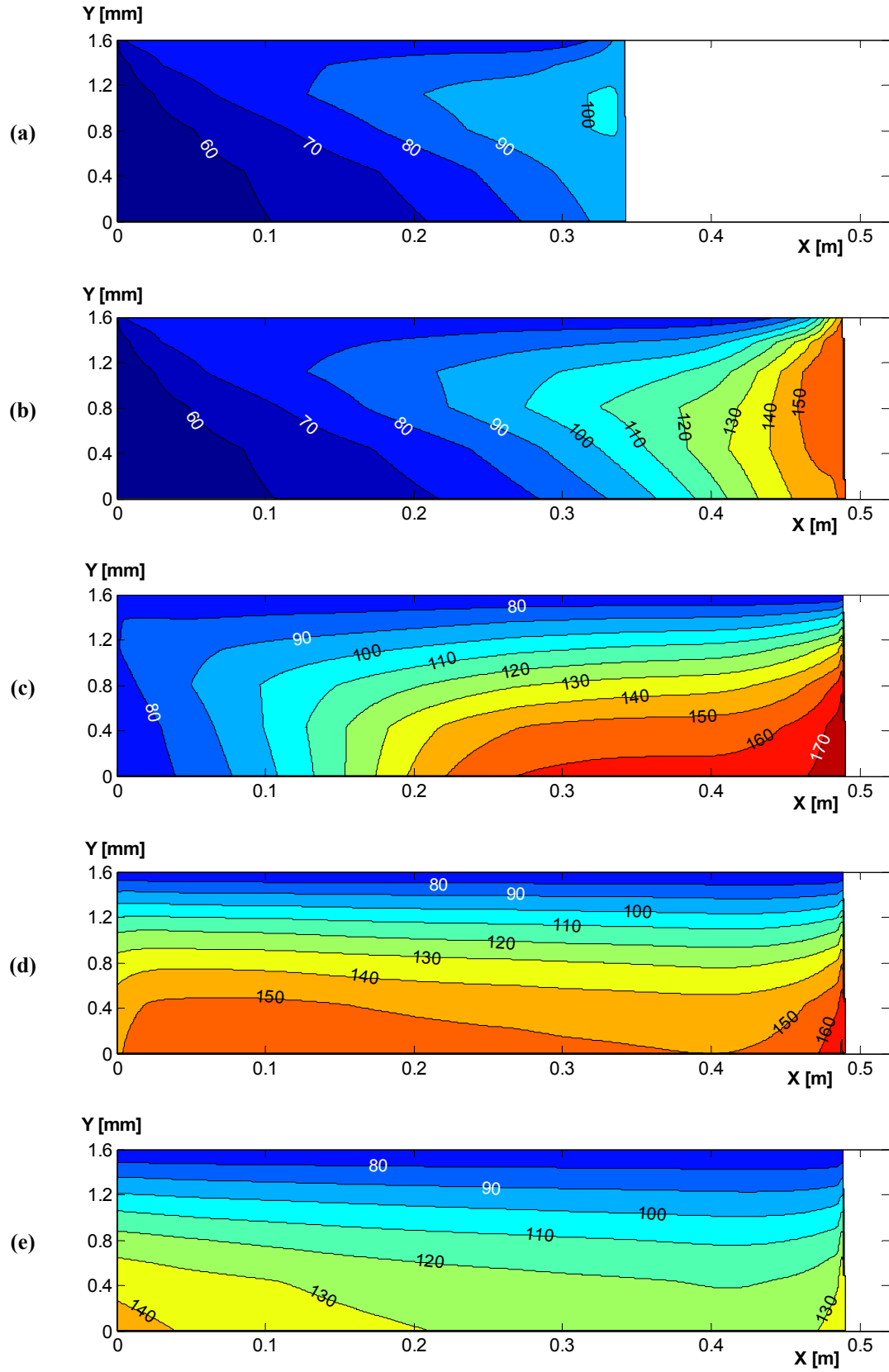


Fig. 44: Temperature [ $^{\circ}\text{C}$ ]. (a)  $t = 4$  s; (b)  $t = 5.72$  s, when the filling stage ends; (c)  $t = 7.6$  s, when the maximum temperature ( $179.0^{\circ}\text{C}$ ) is observed; (d)  $t = 10$  s; (e)  $t = 15$  s. (Figure not to scale).

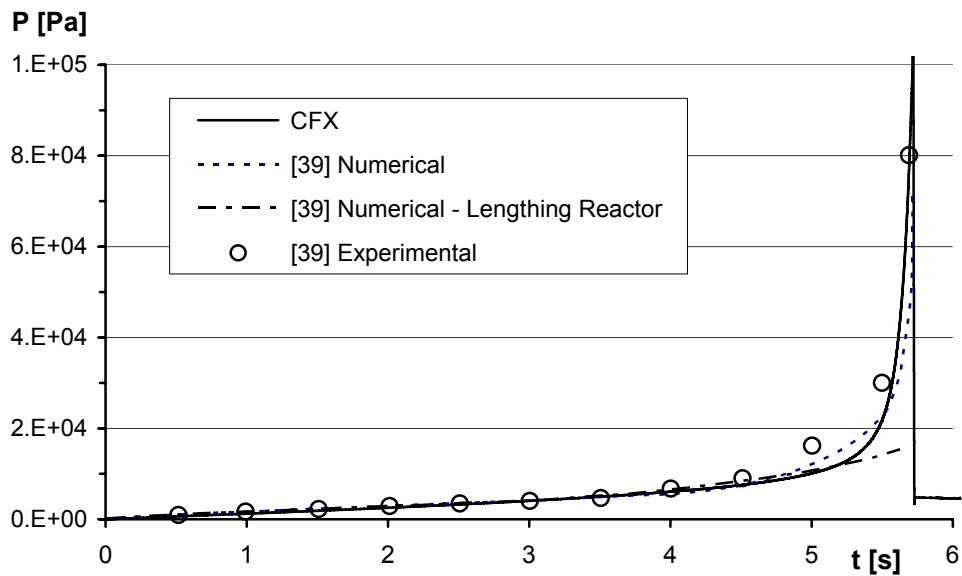


Fig. 45: Inlet pressure along the time.

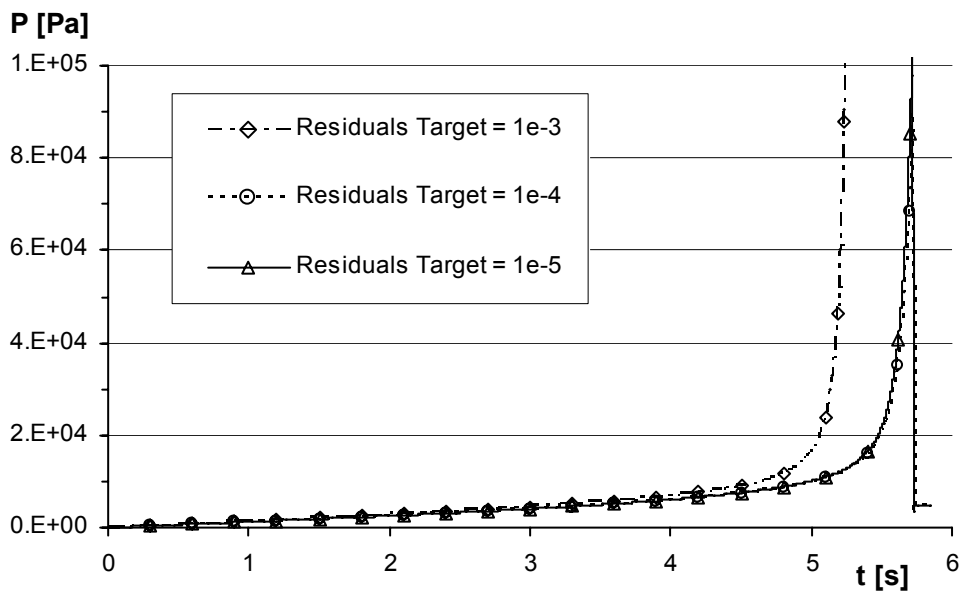


Fig. 46: Inlet pressure obtained with the different residuals target values.

From these comparisons between the results obtained with the three different values of the residuals target, one observes that the results obtained with  $10^{-4}$  are nearly the same as those obtained with  $10^{-5}$  but the computation time is more than 40 % lower. Therefore it seems completely reasonable to accept the value  $10^{-4}$  as good compromise between accuracy and computation time.

Fig. 47 and Fig. 48 show, respectively, the predicted degree of cure and temperature at the end of the filling stage versus the vertical position  $y^* = y/(H/2)$  for some longitudinal positions  $x^* = x/L$ , obtained with CFX and obtained in [39].

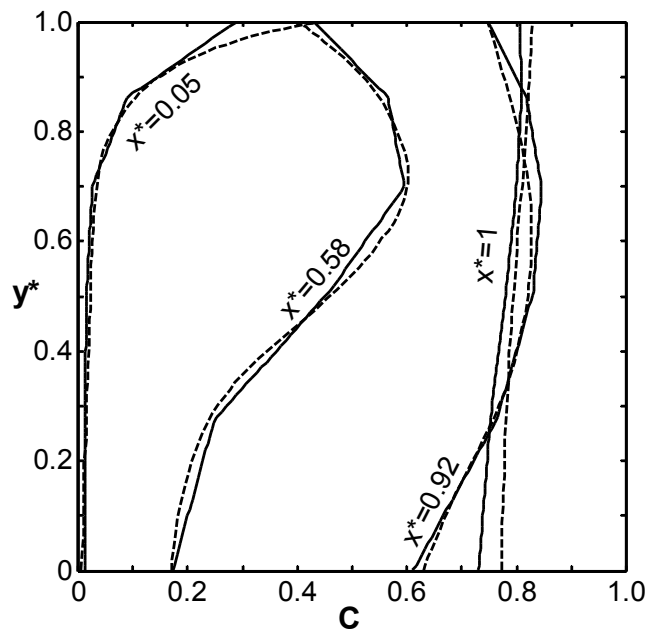


Fig. 47: Degree of cure,  $C$ , at the end of the filling stage.  $x^* = x/L$ ,  $y^* = y/(H/2)$ .  
Solid lines: results obtained with CFX. Dashed lines: numerical results obtained in [39].

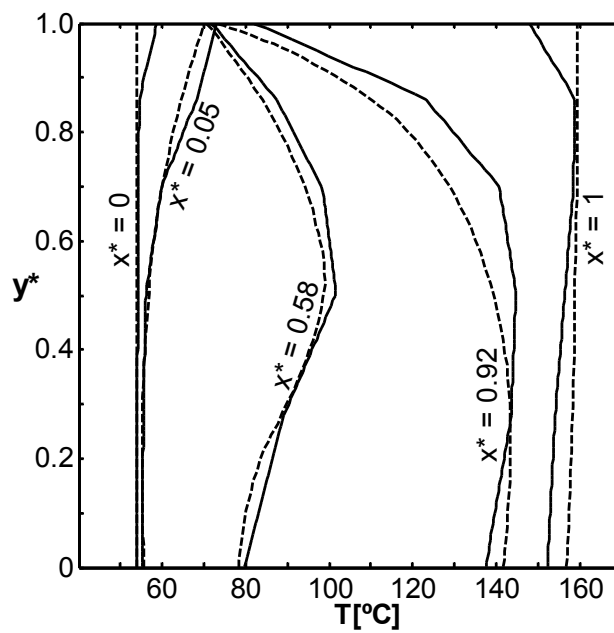


Fig. 48: Temperature [ $^{\circ}\text{C}$ ] at the end of the filling stage.  $x^* = x/L$ ,  $y^* = y/(H/2)$ .  
Solid lines: results obtained with CFX. Dashed lines: numerical results obtained in [39].

The results obtained with CFX are once again in good agreement with the results obtained in [39].

## 4.4 Case studies 3 and 4

### 4.4.1 Cases description

In both previous cases, because of the moulds large ratio width/thickness, two-dimensional simulations could be performed without significant loss of accuracy.

Now, in the next two cases, geometries where all the three dimensions effects are important and where the flow front splits and remerges during the filling stage, were selected with the purpose of testing the ability of the software to model such situations. The geometry used for Case 3, represented in Fig. 49, is the same used in [99] to model the isothermal mould filling with a high viscous polymer melt. The geometry used for Case 4, represented in Fig. 50, is just a slight modification, the rectangular hole was substituted by a circular one.

The resin used in these two cases is again the same RIM type polyurethane used in [39] and in both previous cases, whose properties were described in Tables 5-7. The inlet and walls temperatures are the same as in Case 1, 55.3 °C and 82 °C, respectively.

The filling time,  $t_f$ , was chosen to be the same as in [99], 2 s, corresponding to the inlet flow rates,  $Q_{in}$ , and inlet velocities,  $U_{in}$ , indicated in Table 9.

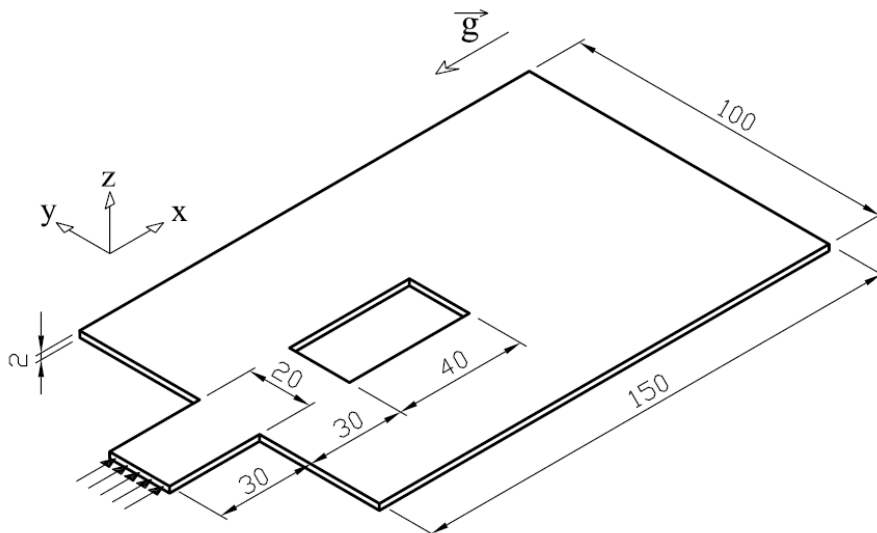


Fig. 49: Mould geometry, and dimensions in millimetres, used for Case 3.

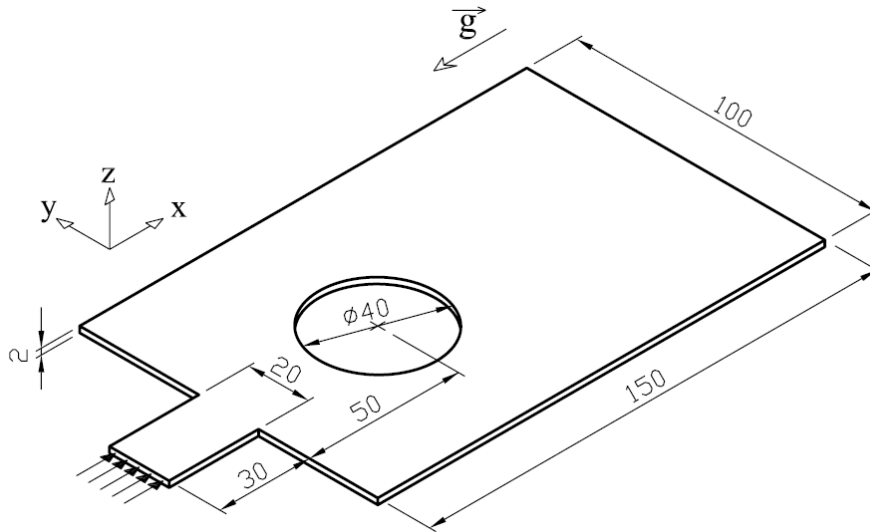


Fig. 50: Mould geometry, and dimensions in millimetres, used for Case 4.

Table 9: Filling conditions for Case 3 and Case 4.

		Case 3	Case 4
V	Mould volume	$2.960 \times 10^{-5} \text{ m}^3$	$2.869 \times 10^{-5} \text{ m}^3$
$t_f$	Filling time	2 s	2 s
$Q_{in} = V / t_f$	Inlet flow rate	$1.480 \times 10^{-5} \text{ m}^3/\text{s}$	$1.434 \times 10^{-5} \text{ m}^3/\text{s}$
$U_{in} = Q_{in} / A_{in}$	Inlet velocity	0.370 m/s	0.359 m/s
$T_{in}$	Inlet temperature	55.3 °C	55.3 °C
$T_w$	Mould temperature	82.0 °C	82.0 °C

#### 4.4.2 Numerical issues

Due to symmetry of the geometries and boundary conditions, only one fourth of the geometries were modelled.

As previously mentioned, convergence difficulties arise when the flow front approximates the outlet boundary. For this reason the calculation domain length was extended from 0.18 m (mould length) to 0.19 m. The calculation meshes used to model these cases are shown in Fig. 51 and Fig. 52. As in the previous cases, the mould half thickness is divided into 5 elements, resulting in 6320 elements and 8190 nodes in Case 3, and 6400 elements and 8304 nodes in Case 4. The extra 0.01 m length corresponds to four rows of mesh elements, which has been shown to be enough to overcome the convergence problems when the resin flow front comes close to the outlet boundary.

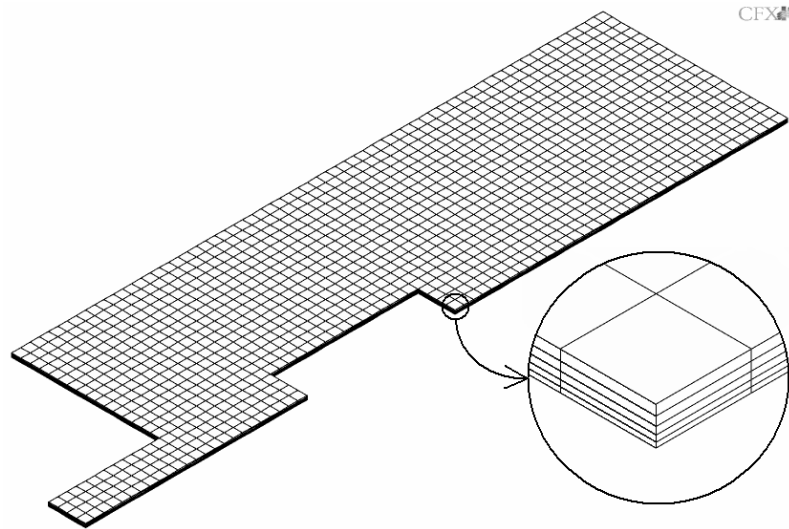


**Fig. 51: Mesh for Case 3 (6320 elements and 8190 nodes).**

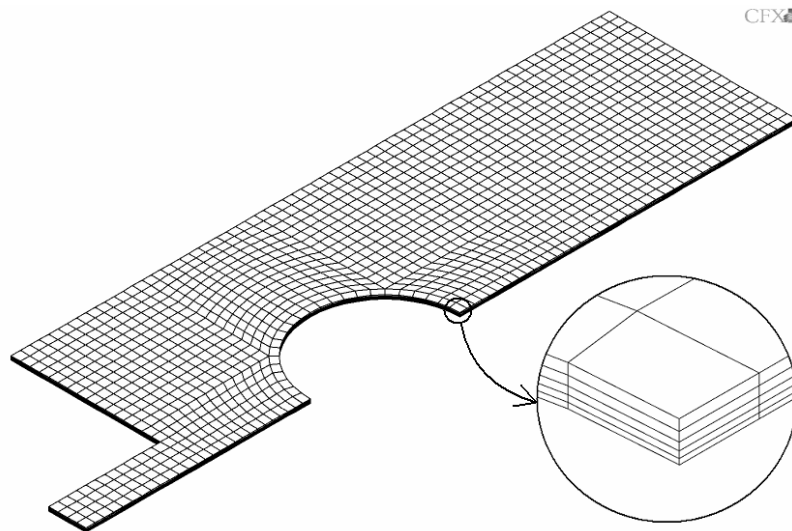


**Fig. 52: Mesh for Case 4 (6400 elements and 8304 nodes).**

The highest values of the Reynolds number are verified at the mould entrance zone, where the cross section area is smaller and consequently the velocity is higher, which for both cases, and based on the resin viscosity at the inlet temperature and zero conversion, have approximately the value of 26.

As in both previous cases, the inlet velocity is set to zero at the end of the filling stage via a third-order polynomial, as it was represented in Fig. 25. All the equations keep being solved until  $t = 2.05$  s, and after that the fluids are assumed to be at rest and only the energy and cure equations are solved.

In these two cases the residuals convergence target was set to  $10^{-4}$ , since in the previous cases it was shown to produce identical results to  $10^{-5}$  and reducing considerably



the computation time, which becomes more and more important as the number of mesh elements and nodes increase.

All the other numerical issues are the same employed in the previous cases. The only exception is the time step in Case 4 after 2.05 s (when only the cure and energy equations are solved), which was increased from  $4 \times 10^{-4}$  s to  $4 \times 10^{-3}$  s. This value is small enough to obtain convergence on this phase of the process simulation and allows reducing slightly the computation time, shown in Fig. 53.

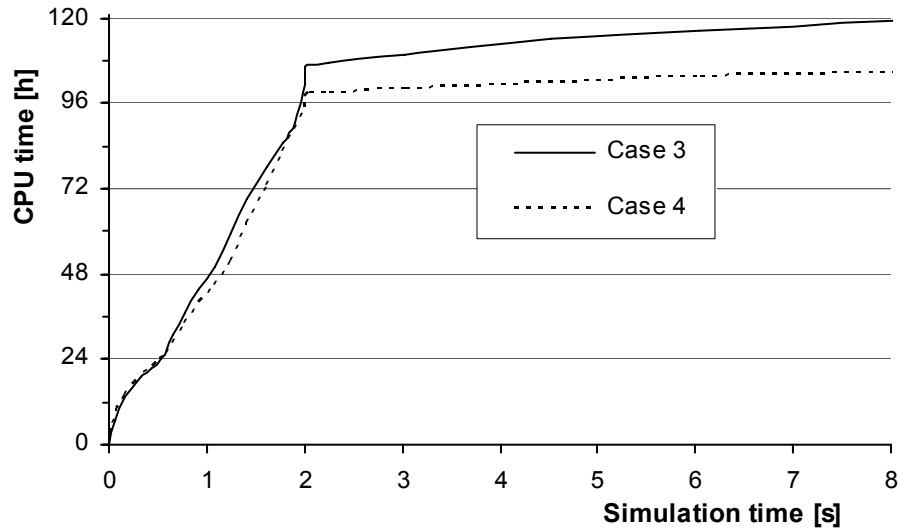
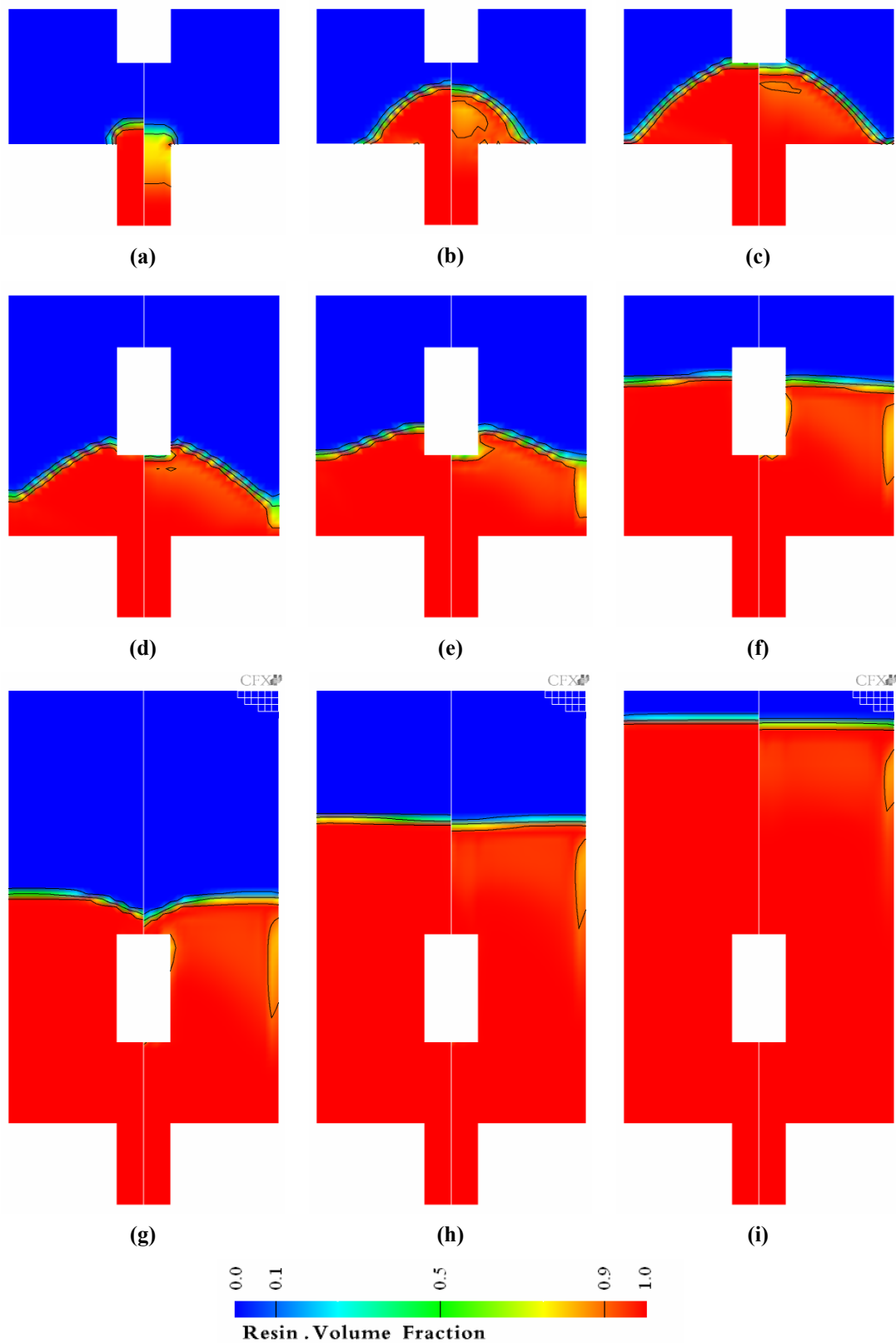


Fig. 53: Computation time versus simulation time.

#### 4.4.3 Results

Fig. 54a-54i and Fig. 55a-55i show, for Case 3 and Case 4, respectively, the obtained resin volume fraction distribution at the midplane (left side of the images) and at the mould wall (right side of the images) during the filling stage.

The flow front is well captured at the midplane at every instant. However, at the mould wall, when the flow front velocity is higher its definition becomes less accurate, Fig. 54a and Fig. 55a, and Fig. 54d-54e and Fig. 55d-55e next to the side wall. This behaviour is due to the value for the drag coefficient obtained in Section 2.2,  $C_D = 5$ , used in the inhomogenous momentum equations, being inadequate for these conditions. This “ideal” value was obtained based on a mould thickness of 3.2 mm and an average velocity of 0.1 m/s, while in these two last cases the mould thickness is 2 mm and in the entrance zone the average velocity is around 0.36 m/s. This shows that the “ideal” value for  $C_D$  is not constant, and it varies at least with the velocity. A lower value should be used, where and when the flow front velocity is higher, in order to decrease the coupling between the phases’ velocities and allow the air to leave the region to be occupied by the resin.



**Fig. 54:** Volume fraction of resin at the midplane (left side) and at the mould wall (right side), during the filling stage, for Case 3. The three contour lines indicate resin volume fractions of 0.1, 0.5 and 0.9.

(a)  $t = 0.1$  s; (b)  $t = 0.2$  s; (c)  $t = 0.35$  s; (d)  $t = 0.45$  s; (e)  $t = 0.55$  s; (f)  $t = 0.8$  s;

(g)  $t = 1.1$ s; (h)  $t = 1.4$  s; (i)  $t = 2$  s (end of the filling stage).

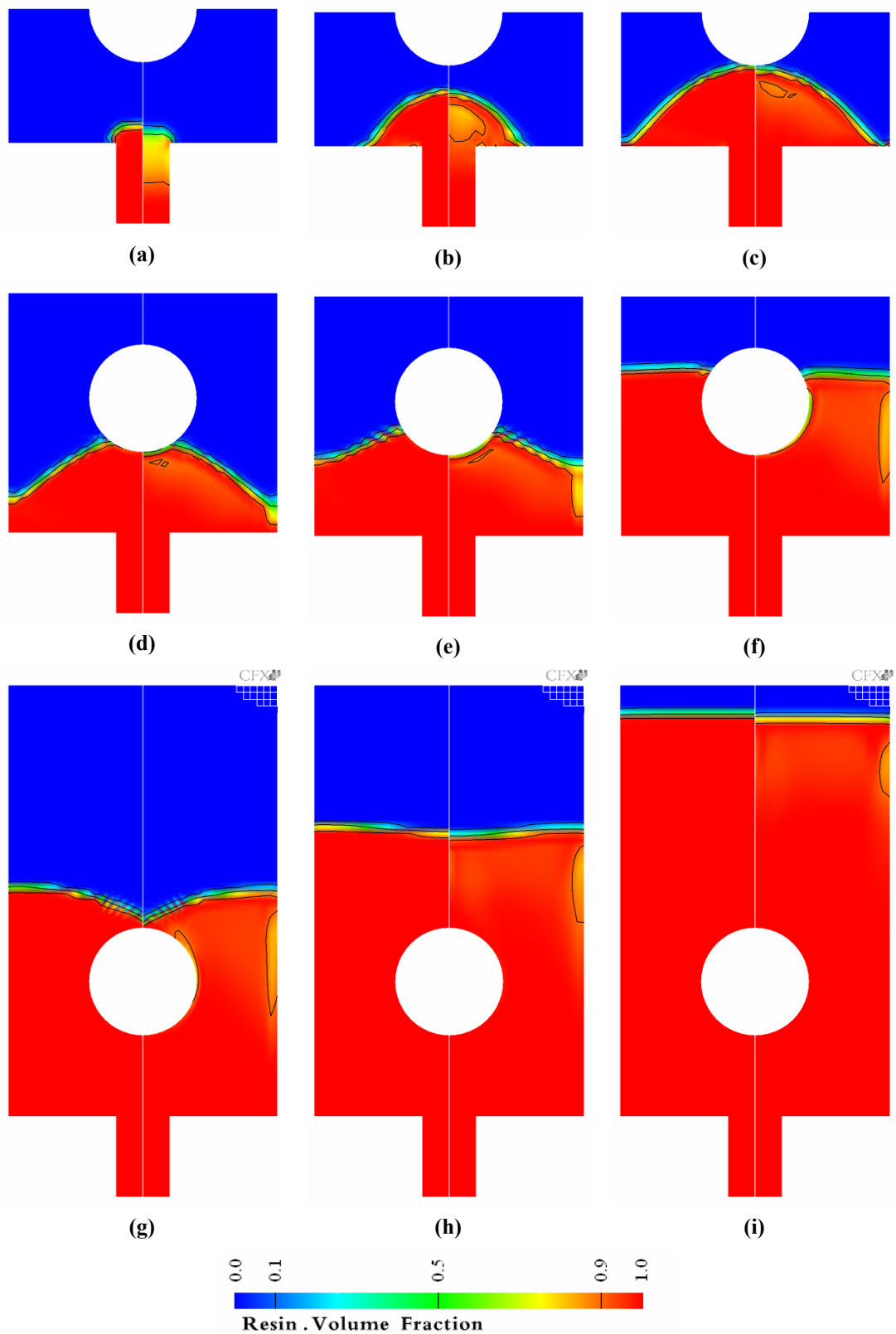


**Fig. 55: Volume fraction of resin at the midplane (left side) and at the mould wall (right side), during the filling stage, for Case 4. The three contour lines indicate resin volume fractions of 0.1, 0.5 and 0.9.**

**(a)  $t = 0.1$  s; (b)  $t = 0.2$  s; (c)  $t = 0.35$  s; (d)  $t = 0.45$  s; (e)  $t = 0.55$  s; (f)  $t = 0.8$  s;**

**(g)  $t = 1.05$  s; (h)  $t = 1.4$  s; (i)  $t = 2$  s (end of the filling stage).**

However, this observed wrong behaviour is not expected to have a significant influence on the solution. As may be seen in the figures, the regions where the resin volume fraction is below 0.9 are small compared to the mould size.

Fig. 56a-56c and Fig. 57a-57c for Case 3, and Fig. 58a-58c and Fig. 59a-59c for Case 4, show the degree of cure and the temperature at the midplane, at the bottom wall, at some longitudinal and transverse planes, at the side walls, and at the flow front (defined as the surface where the resin volume fraction is 0.5), obtained at three instants: at  $t = 1.05$  s (when the flow front reemerges), at  $t = 2$  s (end of the filling stage) and at  $t = 4.2$  s (when the maximum temperature is observed). To allow a better visualization of results, the thickness direction was scaled up 8 times relatively to the other directions.

In both cases, when the flow fronts remerge, at  $t = 1.05$  s, the degree of cure of the streams meeting each other is around 0.05, Fig. 56a and Fig. 58a. If this value is above a critical value, typically 0.40 [5], the material will not interpenetrate and a knit line will be visible and weak. At this instant the highest values of the degree of cure are 0.22, Fig. 56a and Fig. 58a, and the highest temperatures are 84.9 °C, Fig. 57a and Fig. 59a, just slightly above the walls temperature.

At the end of the filling stage,  $t = 2$  s, the resin with higher degree of cure, Fig. 56b and Fig. 58b, and higher temperature, Fig. 57b and Fig. 59b, is located next to the walls, contrasting to the end of the of the filling stage in Case 1 (with the same inlet and wall temperatures, but a longer filling time) where, at the end of the filling stage, the resin with higher degree of cure and temperature was located between the mould centre and the walls, Fig. 28b and Fig. 29b. At this instant, the highest degrees of cure are 0.37, for both cases, and the highest temperatures 92.5 °C and 92.7 °C, for Case 3 and Case 4, respectively.

At  $t = 4.2$  s the situation has inverted, the resin at the mould centre has higher degree of cure, Fig. 56c and Fig. 58c, and its temperature is higher than at the walls, Fig. 57c and Fig. 59c. At this instant the maximum temperatures during the whole process, 155.4 °C, were observed in both cases. This temperature is 22.5 °C below the maximum temperature observed in Case 1, despite the fact that the resin and the inlet and the walls temperatures are the same. This may be explained by the mould thickness being smaller, increasing the heat conduction from the resin to the walls, but also by the shorter filling time, and consequently lower temperatures at its end. At this instant the highest values of the degree of cure are 0.90 and 0.89, for Case 3 and Case 4, respectively, but only 3.0 % and 2.8 % of the resin has solidified, Fig. 56c and Fig. 58c.

At  $t = 5$  s the percentage of resin that has solidified increases to 36 %, and at  $t = 10$  s to 78 %. At  $t = 20.7$  s the last portion of resin reaches the gel point,  $C_g = 0.85$ , and at  $t = 32$  s the totality of the resin has reached the degree of cure of 0.9 and the parts may be safely removed from the moulds.

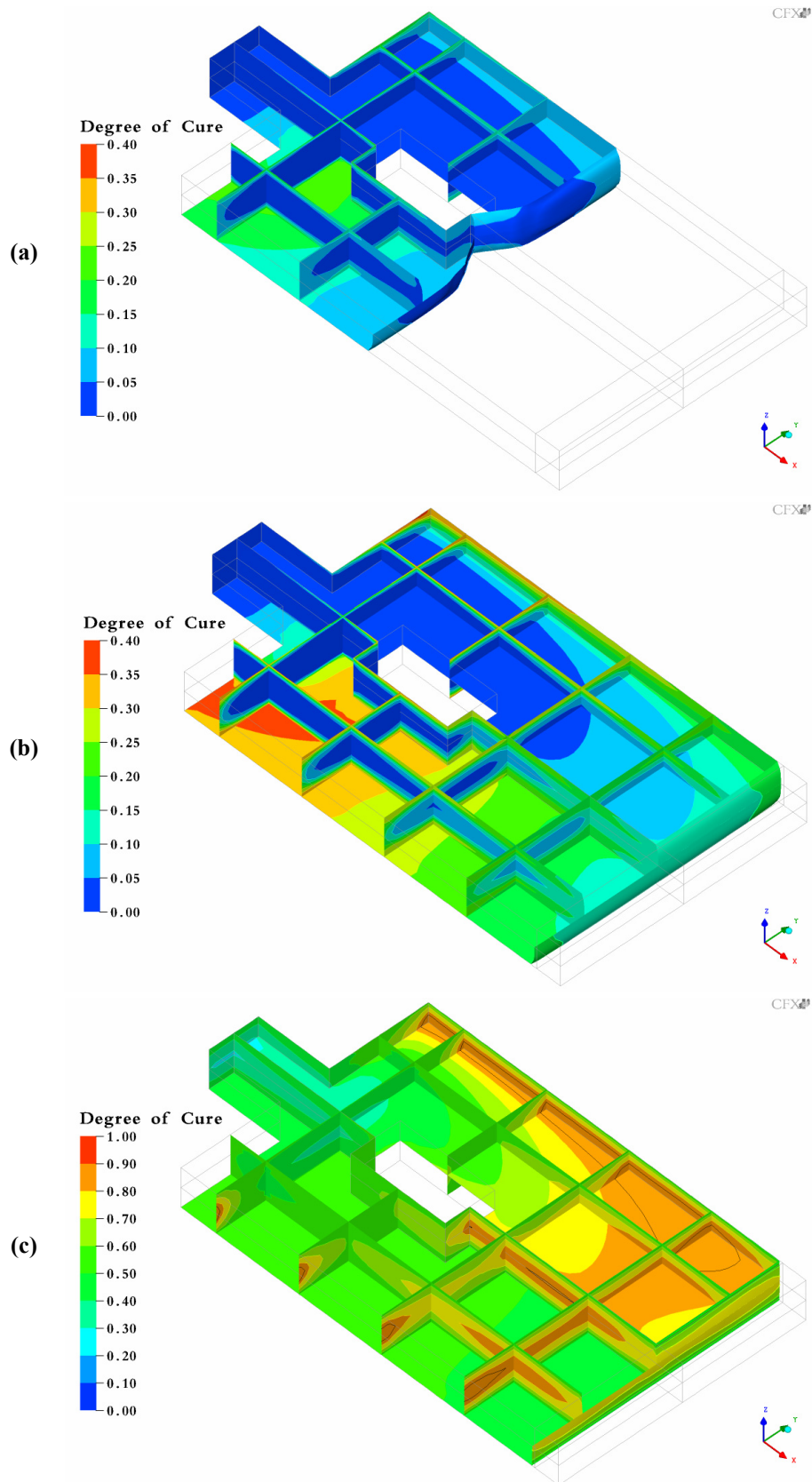


**Fig. 56: Degree of cure for Case 3. (a)  $t = 1.05$  s, when the flow front reemerges; (b)  $t = 2$  s, at the end of the filling stage; (c)  $t = 4.2$  s (the black curves indicate  $C = C_g$ ). (The thickness direction is scaled up 8 times relatively to the other directions).**

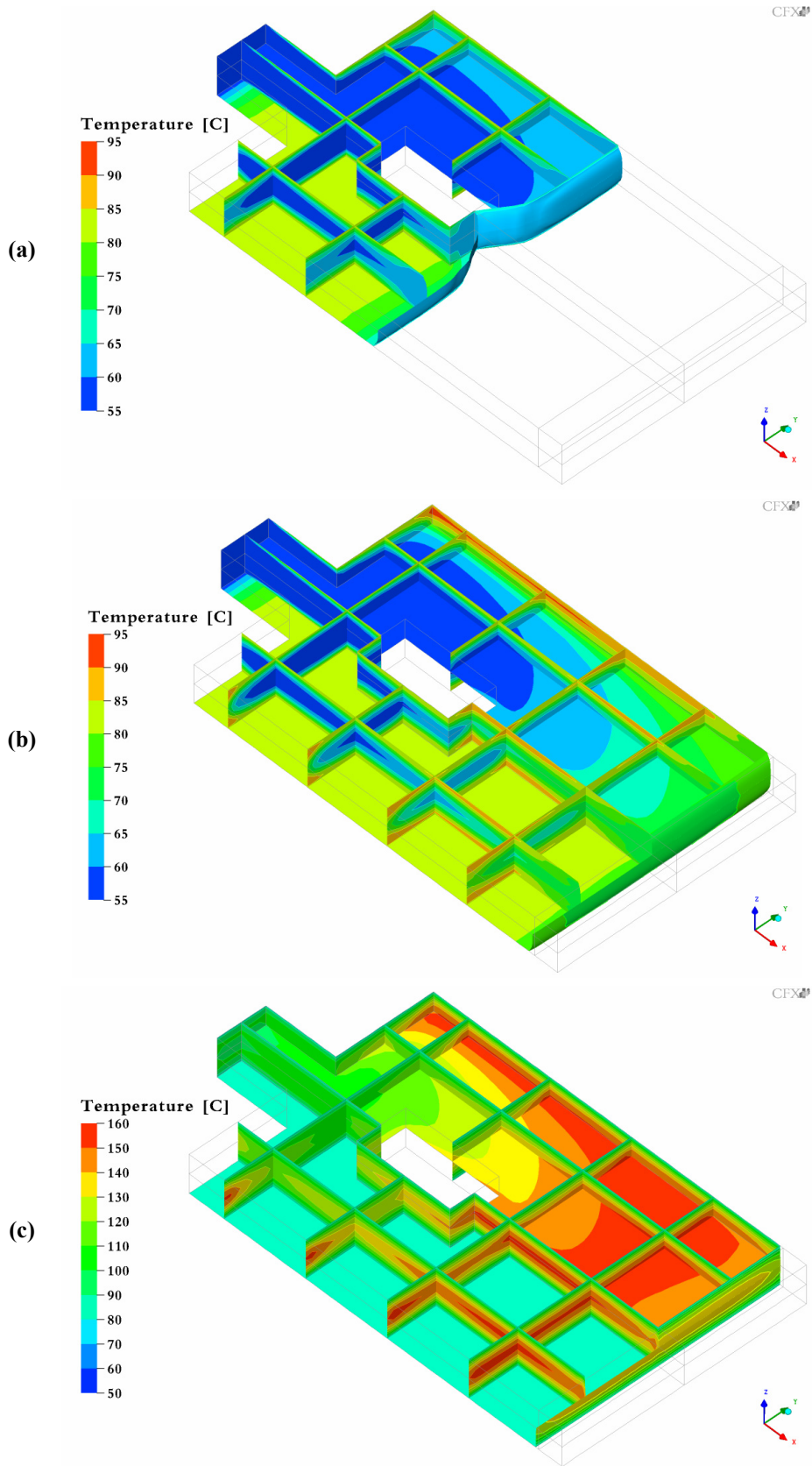


**Fig. 57: Temperature [°C] for Case 3. (a)  $t = 1.05$  s, when the flow front reemerges; (b)  $t = 2$  s, at the end of the filling stage; (c)  $t = 4.2$  s, when the maximum temperature is observed. (The thickness direction is scaled up 8 times relatively to the other directions).**

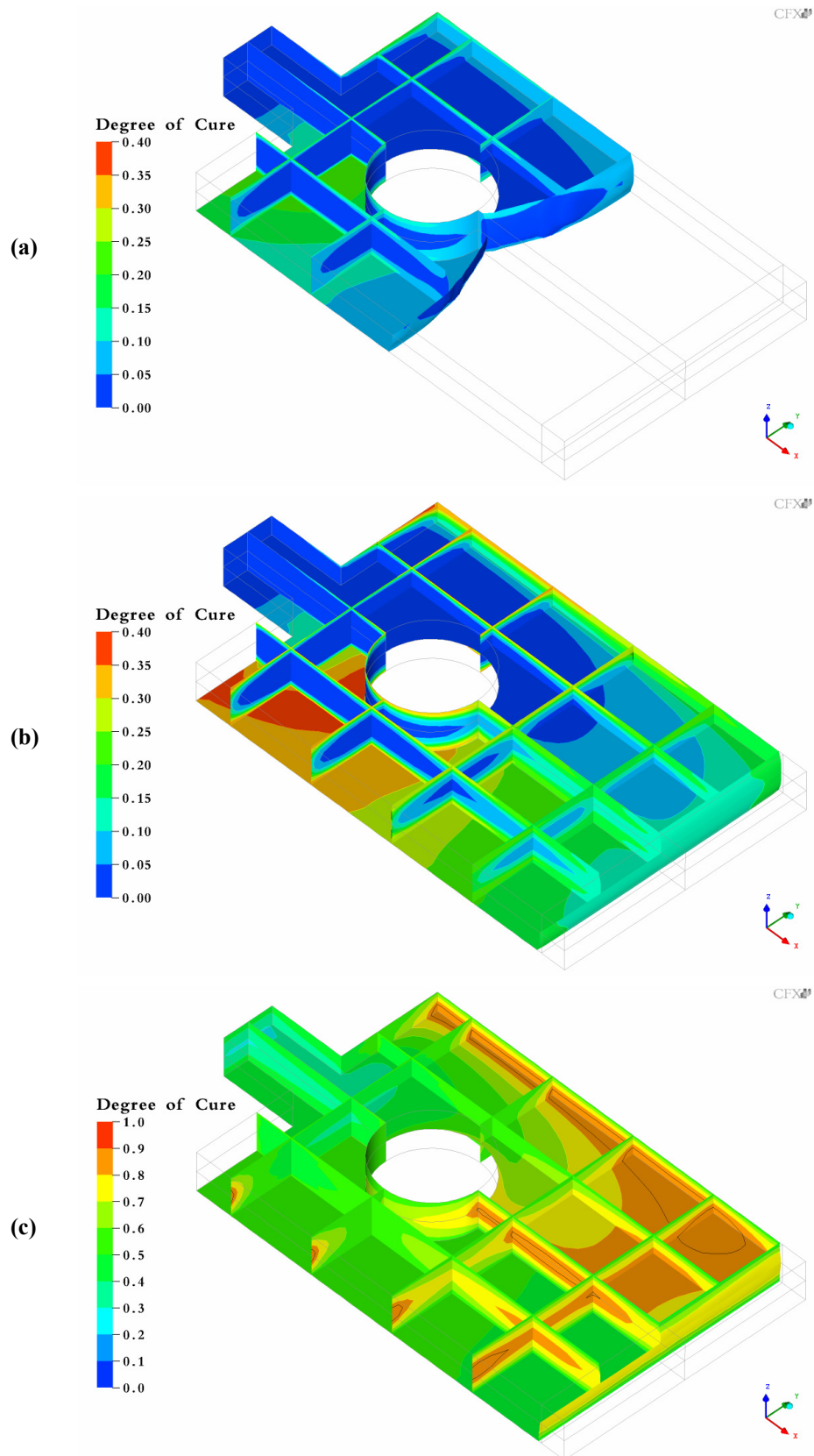


**Fig. 58: Degree of cure for Case 4. (a)  $t = 1.05$  s, when the flow front reemerges; (b)  $t = 2$  s, at the end of the filling stage; (c)  $t = 4.2$  s (the black curves indicate  $C = C_g$ ). (The thickness direction is scaled up 8 times relatively to the other directions).**

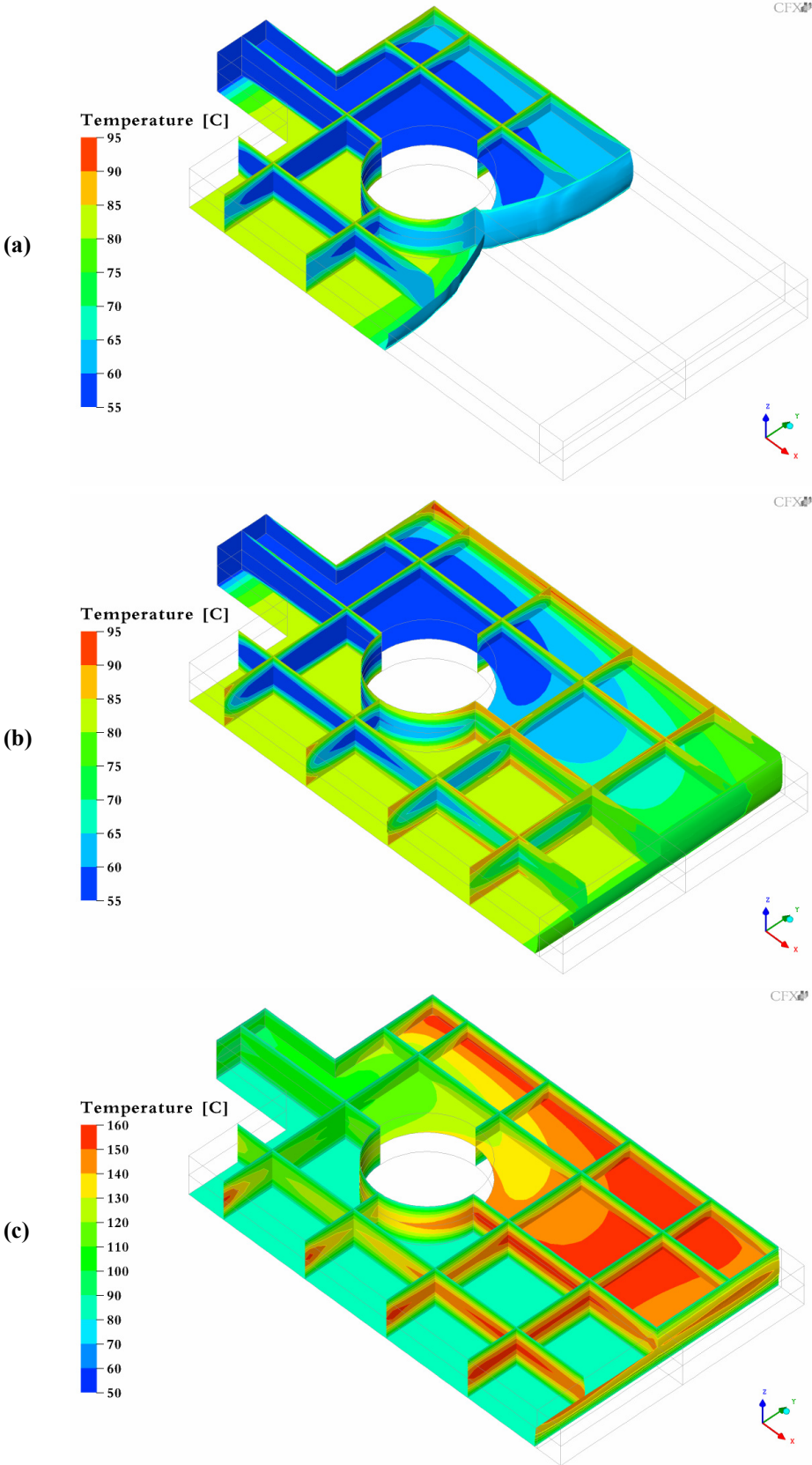


**Fig. 59: Temperature [°C] for Case 4. (a)  $t = 1.05$  s, when the flow front remerges; (b)  $t = 2$  s, at the end of the filling stage; (c)  $t = 4.2$  s, when the maximum temperature is observed. (The thickness direction is scaled up 8 times relatively to the other directions).**



From equation (141), according to the theoretical analysis previously presented in Section 4.2, these times would be 21.2 s and 32.5 s. The differences occur because the last portions of resin to reach  $C = C_g = 0.85$  and  $C = 0.9$  are in contact with the inlet and the walls, and as CFX calculates the source terms based on the nodes values, which, for boundary nodes, as previously mentioned, are not precisely equal to the imposed boundary conditions but represent the average of the boundary control volume, the source term on the cure equation is calculated based in a temperature slightly above the imposed wall temperature. But the differences, being small (2.4 % and 1.5 %), shall not constitute a concern, because in practice it will be impossible to keep the mould walls temperature constant, and this fact will probably cause a higher source of error.

The obtained inlet pressures, for both cases, are shown in Fig. 60. The initial steep parts of the curves, before approximately 0.1 s, correspond to when the flow front is at the entrance zone moving at a higher velocity. Due to the slightly lower inlet velocity, the inlet pressure in Case 3 before 0.65 s is a little lower than in Case 4, but after this instant, because of the smaller cross section around the circular hole, it becomes slightly higher.

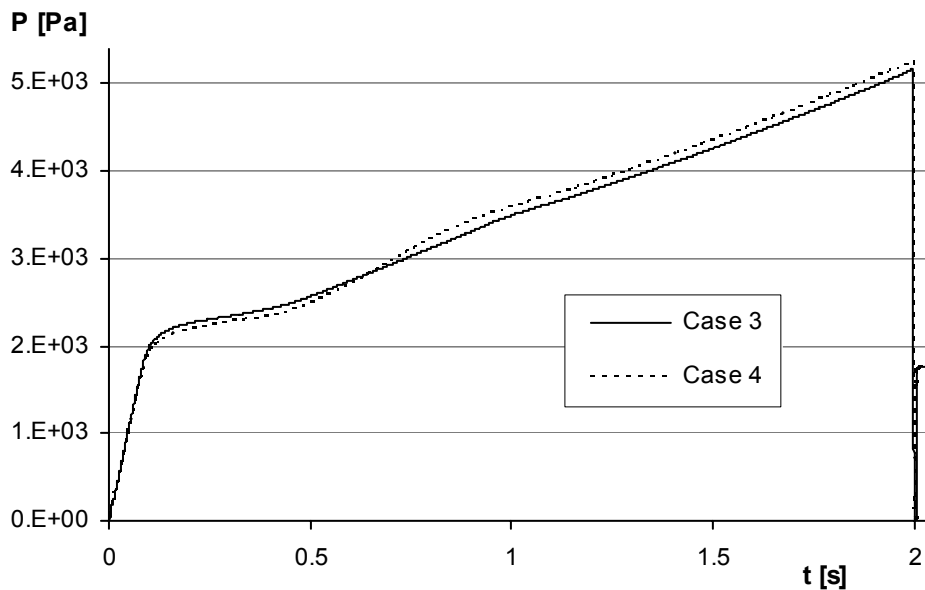


Fig. 60: Inlet pressure along the time.

## 4.5 Conclusions

Ten partial differential equations are necessary to model the RIM simultaneous filling and curing processes. A small time step value and a large number of iterations within each time step are required to achieve convergence, leading to long computing times, even for

two-dimensional analyses and simple geometries with relatively small number of mesh elements.

Nevertheless, two cases were simulated and the results obtained with CFX were compared with available numerical and experimental results, showing a general good agreement with them, what demonstrates that it is possible to simulate the complex RIM simultaneous filling and curing processes using CFX, with a relatively good accuracy, even for situations unlikely to happen in reality, where the gel point is nearly reached in one case, and actually reached in the other, during the filling stage.

Simulations were performed with three different values for the residuals convergence target. The ones performed with  $10^{-4}$  provided analogous results to the ones with  $10^{-5}$ , though requiring a computation time around 40 % shorter, allowing one to consider  $10^{-4}$  as a fair reasonable compromise between accuracy and computation performance.

Two other cases, where all the three-dimensional effects are important and where the flow fronts splits and remerges, were simulated. The flow front was always well captured at the midplane, however, at the wall its definition becomes less accurate when its velocity is higher. This occurs because the drag coefficient value used (previously obtained based on other conditions) is too high for these conditions.

In order to try to reduce the computation time, these cases were run in parallel in two PCs, but the computation times were longer than when run in serial. It is mentioned in the CFX documentation [83, 92, 93] that, typically, a minimum of  $30 \times 10^3$  nodes, for tetrahedral meshes, or  $75 \times 10^3$ , for hexahedral meshes, should be used per partition to see improvements in the computational performance.

## 5 Conclusions

---

Synthetic polymeric materials are nowadays commonly used in all of the major market sectors. They are very attractive from an economical point of view, but also by their aptitude to be manufactured into complex parts and their relatively high weight specific strength and stiffness,

Synthetic polymers can be classified in two major categories: thermoplastics and thermosets. For thermoplastics, by far the largest volume, as the long molecules are not chemically joined, they can be melted, solidified and remelted again. Thermosets upon heating or mixing with appropriate reagents undergo an irreversible chemical reaction, causing the short chain molecules to bound, and leading to the formation of a rigid structure.

Amongst the various polymer processing techniques, injection moulding is one of the most important, representing about one third of all manufactured polymer parts. In TIM, the hot polymer is pushed at high pressure into a cold cavity where it undergoes solidification by cooling. Reactive moulding is quite different, it uses polymerization, instead of cooling, to form the solid part.

RIM is a process for rapid production of complex parts through the mixing and chemical reaction of two or more components. When injection begins, the liquid components, held in separated tanks, flow into a mixing chamber, the streams are intensively mixed, and the mixture begins to polymerize, or cure, as it flows into the mould cavity.

The end use applications for RIM can, at present, be found in a large variety of forms, and although polyurethanes comprise the majority in RIM processing, there are also other types of chemical systems that can be processed.

Due to RIM liquids' low viscosity, large parts can be produced with relatively small machines, complex shapes with multiple inserts can be fabricated, low pressures can be used to fill the moulds, and these may be constructed from light-weight materials often at lower costs than for TIM, and mould clamping forces are much lower requiring lower cost presses, opening up short runs applications and even prototype applications. Low viscosities also open options in the use of reinforcements. RIM's temperatures are typically lower than those for TIM, with less energy demands.

However, handling of reactive, and often hazardous liquids, requires special equipments and procedures, and as some components freeze at room temperature, a temperature controlled environment is required, increasing the costs. Because of the low viscosity, moulds are difficult to seal, increasing flash, and low viscosity liquids penetrate

mould surfaces, requiring the use of release agents. Due to low pressure, it is difficult to remove air from behind inserts and from corners, rendering vent locations extremely important. If flow into the mould is too rapid, air may be entrained and large bubbles appear in the final part, but moulds filled too slowly may lead to short shots.

The first attempts to study the filling stage in injection moulding took place in the beginning of the 1950s with flow visualizations and tracer studies.

Numerical simulations basically started in the early 1970s. The first developments were applied to the filling stage of simple tubular, circular and rectangular geometries, allowing the flow to be assumed as unidirectional. The temperature was considered as two-dimensional, one coordinate in the flow direction and the other in the thickness direction, leading to the so-called 1½D approach, and finite difference techniques were used to solve the set of equations.

The real breakthrough in injection moulding simulations came, in the beginning of the 1980s, with the development of a general 2½D approach, combining finite elements along the midsurface of the cavity with finite differences along the thickness direction. However, based on the Hele-Shaw approximation, this approach was not able to represent the complex flow kinematics of the flow front region, the fountain flow. The description of this phenomenon was addressed by means of experimental, analytical and numeric methods, leading to approximate models able to capture its kinematics without resolving its complex 3D details.

To date, several commercial and research three-dimensional programs for injection moulding simulations have been developed.

Early studies in RIM simulation were dedicated to the static analysis of heat transfer and cure, assuming that the curing stage could be decoupled from the filling stage. More realistic models were obtained by extending the 1½D approach to RIM. Extensions to the 2½D approach were only reported more recently, in the 1990s, and some 3D simulations have already been reported in some works.

Although many commercial codes are able to perform 3D injection moulding simulations, the 2½D Hele-Shaw approach is still the standard numerical framework for simulation of injection moulding. Because typically in injection moulding the part thickness is much smaller than its overall dimensions and the polymer viscosity is high (resulting in low Reynolds numbers), in the 2½D formulation the inertia effect, the velocity component and thermal convection in the thickness direction, and, the velocity gradients and the heat conduction in the flow directions, are neglected. Based on these approximations, the continuity and momentum equations are simplified and merged into a simple two-dimensional equation in terms of pressure and fluidity, and a simplified energy equation is obtained. Due to those assumptions and simplifications, the computation time can be considerably reduced relatively to full three-dimensional formulations. But although its successful applications, the 2½D formulation has its limitations: in some cases the

inertia and three-dimensional effects may become significant enough to influence the flow, for the RIM process, because of resins low viscosity, the inertia and gravity effects cannot be omitted, and due to the importance of the fountain flow in RIM, a three-dimensional formulation is expected to provide more accurate information than simple fountain flow approximations.

A very simple case, the filling of a space between two parallel plates with a liquid with constant density and viscosity, was studied. Applying the Newton's Second Law of motion, the theoretical values of the pressure, and the theoretical values of the pressure according to the CFX Homogenous Model, which omits the air hydrostatic pressure effect, were derived. The case was simulated, with four different meshes, using the CFX Homogeneous Model. This model, which assumes that both liquid and gaseous phases share the same velocity field, should be the appropriate for this type of process, as the two phases are completely stratified and the interface is well defined. In the simulations, the resin-air interface was well captured within two mesh elements, proving the efficiency of the advection and transient compressive discretization schemes. However, the interface is always ahead of its theoretical position, and, much more important, it does not touch the walls (there is always a layer of air between the resin and the walls) what obviously is not in accordance with reality. Moreover, reducing the mesh elements' size, either on the longitudinal direction or on the transverse direction, does not contribute to improvement of this incorrect behaviour. Because of the resin volume fraction next to the walls being close to zero, the computed viscosity is much smaller than its actual value, leading to a wrong velocity profile and to an underestimation of the viscous effect contribution to pressure. This is of major importance, as the injection pressure is one of the key parameters to be predicted from numerical simulations, but also because, when solving the cure and the energy equations, errors on the advection terms may lead to completely wrong final results. The gravity and the viscous effects contribution to pressure, as well as the whole pressure, obtained from the simulations were compared with theoretical values. The error of the inlet pressure due to the viscous effect, obtained with the four different meshes, was comprised between 30 % and 35 %, showing only a tiny decrease with the increase of the number of mesh elements, which does not seem to be a solution for the problem. This behaviour has already been mentioned by some authors, the physically correct no-slip boundary condition applied to the air phase prevents the flow from touching the walls, and they claim that the no-slip condition should be imposed only on the filled portion of the mould.

As CFX does not allow the implementation of conditional boundary conditions, the only way to prescribe the no-slip boundary condition only on the filled portion of the mould, and the free-slip condition on the empty portion, is by employing the inhomogeneous model, which assumes that each phase has its own velocity field and they interact via interphase transfer terms. The no-slip condition was applied to the resin equations and the free-slip condition to the air equations. The interphase momentum

transfer term, which links the two sets of momentum equations, is function of the phases' relative velocities, their density and volume fractions (it tends to zero as the volume fraction of one of the phases tends to zero, being meaningful only at the interface), and two parameters that must be defined by the user: a non-dimensional drag coefficient,  $C_D$ , and an interface length scale,  $d_{\alpha\beta}$ . However, as it was shown, the individual values of these parameters do not matter, but their quotient does. Therefore, the parameter  $d_{\alpha\beta}$  was kept constant (with the CFX default value) and simulations were performed with different values of  $C_D$ , from 0.05 to 500.

Contrasting with the simulations employing the homogenous model, in the simulations performed with  $C_D$  set to 0.05, 0.5 and 5, the resin-air interface touches the walls and is in very good agreement with its theoretical position. But when  $C_D$  increases to 50, the behaviour becomes similar to that of the homogenous model, what is explained by the increase of the interphase momentum transfer term causing the phases' flow fields to equalize. As it was done for the simulations employing the homogeneous model, the results obtained from the simulations employing the inhomogeneous model were compared with theoretical values. For  $C_D$  equal to 0.05, 0.5 and 5, the errors were considerably reduced relatively to the ones obtained with the homogenous model (the error of the viscous contribution to pressure decreased from 33 % to 4 %). The evolution of the obtained inlet pressures with time was compared with theory and, despite following very closely the theoretical pressure, the pressures obtained with the three lowest values of  $C_D$  exhibit oscillations with the same period at which the interface crosses the mesh elements. The amplitudes of these oscillations are bigger as smaller is the value of  $C_D$ , and for  $C_D = 5$ , although still present, the oscillations nearly vanish. The shortest computation time was obtained with  $C_D$  equal to 5, what together with the presented results, allows one to conclude that, among the five different analyzed values,  $C_D = 5$  is the most suitable for the studied case. However, this leaves an unanswered question: would this value also be the most suitable one for other physical and/or numerical conditions?

The cure of the resin can be modelled in CFX as a transient convection-source equation for an additional variable, the degree of cure. But, as this is not a standard equation in CFX, and as errors involving the degree of cure will give rise to errors involving the other variables, various schemes for the discretization of the transient and advection terms of the cure equation were tested. A one-dimensional filling case with a first order rate of cure (allowing one to obtain the analytical solution) was studied. Simulations were performed with combinations of the first or the second order Euler transient schemes and the high resolution or the compressive advection schemes. The results were compared with theory, showing that the most accurate ones were obtained with the combination of the second-order Euler transient scheme with the high resolution advection scheme.

As CFX-5.6, for multiphase flows, does not model the viscous and pressure works neither the kinetic energy effects, the energy equation solved for the resin is simply the thermal energy equation. Although in the most recent versions of CFX it is possible to use the full energy equation for multiphase flows, because the viscous work is neglectable for typical RIM situations and because the kinetic energy effects are only important for high speed flows, the thermal energy equation is perfectly valid to model the energy balance in RIM.

Two case studies, experimentally conducted by [39], were used to validate the whole model in CFX, consisting of the mass, momentum, volume fraction, energy and cure equations. Both moulds are simple rectangularly shaped cavities and filled with a RIM type polyurethane. In both cases, as the mould width is considerably larger than the thickness, two-dimensional simulations were performed, and due to symmetry only half of the geometry was modelled.

Both cases were run on a mesh with 5 elements on the transverse direction, and one of them also on a mesh with 10 elements on the transverse direction. The inhomogeneous model was employed, together with the walls no-slip boundary condition for the resin equations and the free-slip condition for the air equations. All the governing equations kept being solved slightly longer ( $\sim 2\%$ ) than the filling time, and after that the fluids were assumed to be completely at rest and only the energy and the cure equations were solved. Because of the very small time step required to obtain convergence, the computation times were considerable. In both cases high degrees of cure were achieved at the end of the filling stage, resulting in a significant raise of viscosity and consequently the increase of the inlet pressure. The highest temperature observed during the whole process was, in both cases, above the temperature resulting from a complete adiabatic cure reaction, meaning that, although the walls temperature are significantly lower than those highest temperature values, the part of the resin that reached that temperature had to have a positive energy balance, along its path, with its surroundings. This clearly shows that the adiabatic temperature rise cannot be used directly as an upper limit for the maximum resin temperature during the RIM process, and attests the complexity of the simultaneous flow motion, cure reaction and heat transfer processes. Some results obtained from the simulations, such as the evolution of the inlet pressure and of temperatures with time, and the degree of cure and the temperature distributions at the end of the filling stage, were compared with available numerical and experimental results from [39] and numerical results from [72], showing a general good agreement with those.

Two other cases, where all the three dimensions effects are important and where the flow front splits and reemerges, were simulated. At the midplane the flow front was always well captured, but at the wall its definition becomes less accurate when its velocity is higher. The times, obtained from the simulations, for the resin to have completely

solidified and to have reached the degree of cure such that the parts may be removed from the mould, showed only a small difference relatively to the theoretical analysis presented.

It was demonstrated that CFX is capable to simulate the complexities of the RIM simultaneous three dimensional filling and curing processes with good accuracy. However, even for simple geometries and meshes with very few number of elements (in the context of what is nowadays common in CFD), due to the very small time steps necessary to obtain convergence, the computation times are considerably long. More complex geometries, because of details, will require finer meshes and very probably also smaller time steps, which will drive the computation times to some impractical values. Even taking cases 3 and 4 as a reference, which took around 5 days of CPU time to complete 8 s of simulation, if the parts were slightly different and did not have the two planes of symmetry and the whole geometry had to be modelled, the computation time, making a rough extrapolation, would rise to 20 days. But, in order to increase accuracy, if one wanted to double, from 5 to 10, the number of elements on the thickness direction (in the 2½D approach the thickness direction is typically divided in 8-20 layers [14]), keeping the same aspect ratio of the mesh elements, the computation time would jump to 160 days ( $20 \text{ days} \times 2^3$ ).

In all the simulated cases, the moulds and the 2D geometries were filled upwards and they had a full outlet at the top, placed at least 4 mesh elements ahead of the final position of the flow front. In RIM, because of the resins low viscosities, the moulds are commonly filled upwards to facilitate the exit of the air and to avoid the formation of air pockets (in TIM, because of the polymers high viscosity, the gravity effect, and therefore the mould orientation, are irrelevant), but surely real moulds do not have full outlets. Instead, they contain vents, which shall be ideally located so that the totality of the air can leave the mould. But, because of their tiny dimensions, vents cannot be meshed. In fact they could, but that would require the mould to be meshed with elements with the same order of size as the vents, what would mean a completely unrealistic computation effort. However, and leaving a suggestion for future work, the parts of the mould walls containing vents may possibly be modelled as regions resistant to the advance of the resin but free to the passage of the air, that is, as subdomains with resistive source terms on the resin momentum equations.



## References

---

- [1] D. V. Rosato, D. V. Rosato and M. G. Rosato, *Injection Molding Handbook – 3<sup>rd</sup> Ed.*, Kluwer Academic Publishers, Boston, 2000.
- [2] O. Mal, *Modelling and Numerical Simulation of Reaction Injection Moulding Processes*, PhD Thesis, Université catholique de Louvain, Louvain-la-Neuve, March 1999.
- [3] J. J. van der Werf and A. H. M. Boshouwers, *INJECT-3, A Simulation Code for the Filling Stage of the Injection Moulding Process of Thermoplastics*, PhD Thesis, Technische Universiteit Eindhoven, Eindhoven, May 1988.
- [4] J. Vlachopoulos and D. Strutt, Polymer processing, *Materials Science Technology*, Vol. 19, No. 9, 2003, p. 1161-1169.
- [5] C. W. Macosko, *RIM - Fundamentals of Reaction Injection Molding*, Hanser Publishers, Munich, 1989.
- [6] Bayer Polymers LLC. (2003 <http://www.rimmolding.com>)
- [7] C. D. Snyder, Materials for Reaction Injection Molding (RIM) Processing, 2001 Annual Conference of the Composites Fabricators Association (COMPOSITES 2001), Tampa, Florida, USA, October 2001.
- [8] Kawin International, Inc. (2003 <http://www.kawincomposites.com>)
- [9] F. T. Wickis Jr., Reaction injection molding, *Medical Device & Diagnostic Industry Magazine*, April 1996.  
(2003 <http://www.devicelink.com/mddi/archive/96/04/014.html>)
- [10] I. Barros, *Modelação do Comportamento Térmico de Moldes de Injecção*, PhD Thesis, Universidade do Minho, Guimarães, June 2004.
- [11] R. S. Spencer and G. D. Gilmore, Some flow phenomenon in the injection moulding of polystyrene, *Journal of Colloid Science*, Vol. 6, No. 2, 1951, p. 118-132.

- [12] R. L. Ballman, T. Shusman and H. L. Toot, Injection molding: flow of a molten polymer into a cold cavity, *Industrial and Engineering Chemistry*, Vol. 51, No. 7, 1959, p. 847-850.
- [13] F. J. Rielly and W. F. Price, Plastic flow in injection molds, *Society of Plastic Engineers Journal*, 1961, p. 1097-1101.
- [14] S.-W. Kim and L.-S. Turng, Developments of three-dimensional computer-aided engineering simulations for injection moulding, *Modelling and Simulations in Materials Science and Engineering*, Vol. 12, No. 3, 2004, p. S151-S173.
- [15] D. H. Harry and R. G. Parrot, Numerical simulation of injection mold filling, *Polymer Engineering and Science*, Vol. 10, No. 4, 1970, p. 209-214.
- [16] M. R. Kamal and R. Kening, The injection molding of thermoplastics. Part I: Theoretical model, *Polymer Engineering and Science*, Vol. 12, No. 4, 1972, p. 294-301.
- [17] M. R. Kamal and R. Kening, The injection molding of thermoplastics. Part II: Experimental test of the model, *Polymer Engineering and Science*, Vol. 12, No. 4, 1972, p. 302-308.
- [18] J. L Berger and C. G. Gogos, A numerical simulation of the cavity filling process with PVC in injection molding, *Polymer Engineering and Science*, Vol. 13, No. 2, 1973, p. 102-112.
- [19] P.-C. Wu, C. F. Huang, C. G. Gogos, Simulation of the mold filling process, *Polymer Engineering and Science*, Vol. 14, No. 3, 1974, p. 223-230.
- [20] C. Gutfinger, E. Broyer and Z. Tadmor, Melt solidification in polymer processing, *Polymer Engineering and Science*, Vol. 15, No. 7, 1975, p. 515-524.
- [21] G. Williams and H. A. Lord, Mold-filling studies for the injection molding of thermoplastic materials. Part I: The flow of plastic materials in hot and cold walled circular chanel, *Polymer Engineering and Science*, Vol. 15, No. 8, 1975, p. 553-568.

- 
- [22] H. A. Lord and G. Williams, Mold-filling studies for the injection molding of thermoplastic materials. Part II: The transient flow of plastic materials in the cavities of injection-molding dies, *Polymer Engineering and Science*, Vol. 15, No. 8, 1975, p. 569-582.
- [23] J. R. A. Pearson, *Mechanics of Polymer Processing*, Elsevier, Amsterdam, 1985.
- [24] S. Richardson, Hele-Shaw flow with a free boundary produced by the injection of fluid into a narrow channel, *Journal of Fluid Mechanics*, Vol. 56, No. 4, 1972, p. 609-618.
- [25] Y. Kuo and M. R. Kamal, The fluid mechanics and heat transfer of injection mold filling of thermoplastic materials, *AIChE Journal*, Vol. 22, No. 4, 1976, p. 661-669.
- [26] M. E. Ryan and T.-S. Chung, Conformal mapping analysis of injection mold filling, *Polymer Engineering and Science*, Vol. 20, No. 9, 1980, p. 642-651.
- [27] S. M. Richardson, H. J. Pearson and J. R. A. Pearson, Simulation of injection moulding, *Journal of Fluid Mechanics*, Vol. 56, No. 4, 1980, p. 609-618.
- [28] S. M. Richardson, Simplified geometry models, in *Fundamentals of Computer Modeling for Polymer Processing*, Hanser Publishers, Munich, Chapter 4, 1989.
- [29] C. A. Hieber and S. F. Shen, A finite element / finite difference simulation of the injection molding filling process, *Journal of Non-Newtonian Fluid Mechanics*, Vol. 7, No. 1, 1980, p. 1-32.
- [30] A. C. B. Bogaerds, *Stability Analysis of Viscoelastic Flows*, PhD Thesis, Technische Universiteit Eindhoven, Eindhoven, December 2002.
- [31] W. Rose, Fluid-fluid interfaces in steady motion, *Nature*, Vol. 191, No. 4785, 1961, p. 242-243.
- [32] L. R. Schmidt, A special mold and tracer technique for studying shear and extension flows in a mold cavity during injection molding, *Polymer Engineering and Science*, Vol. 14, No. 11, 1974, p. 797-800.

- [33] C. G. Gogos, C.-F. Huang and L. R. Schmidt, The process of cavity filling including the fountain flow in injection molding, *Polymer Engineering and Science*, Vol. 26, No. 20, 1986, p. 1457-1466.
- [34] D. J. Coyle, J. W. Blake and C. W. Macosko, The kinematics of fountain flow in mold-filling, *AIChE Journal*, Vol. 33, No. 7, 1987, p. 1168-1177.
- [35] E. Vos, H. E. H. Meijer and G. W. Peters, Multilayer injection molding, *International Polymer Processing*, Vol. 6, No. 1, 1991, p. 42-50.
- [36] W. Zoetelief, *Multi-component Injection Moulding*, PhD Thesis, Technische Universiteit Eindhoven, Eindhoven, April 1995.
- [37] S. Bhattacharji and P. Savic, Real and apparent non-Newtonian behaviour in viscous pipe flow of suspensions driven by a fluid piston, *Proceedings of the 1965 Heat Transfer and Fluid Mechanics Institute*, Stanford University Press, 1965, p. 248-262.
- [38] Z. Tadmor, Molecular orientation in injection molding, *Journal of Applied Polymer Science*, Vol. 18, No. 6, 1974, p. 1753-1772.
- [39] J. M. Castro and C. W. Macosko, Studies of mold filling and curing in the reaction injection molding process, *AIChE Journal*, Vol. 28, No. 2, 1982, p. 250-260.
- [40] M. R. Kamal, E. Chu, P. G. Lafleur and M. E. Ryan, Computer simulation of injection mold filling for viscoelastic melts with fountain flow, *Polymer Engineering and Science*, Vol. 26, No. 3, 1986, p. 190-196.
- [41] H. Mavridis, A. N. Hrymak and J. Vlachopoulos, Finite element simulation of fountain flow in injection molding, *Polymer Engineering and Science*, Vol. 26, No. 7, 1986, p. 449-454.
- [42] R. A. Behrens, M. J. Crochet, C. D. Denson and A. B. Metzner, Transient free surface flows: Motion of a fluid advancing in a tube, *AIChE Journal*, Vol. 33, No. 7, 1987, p. 1178-1186.
- [43] M. R. Kamal, S. K. Goyal and E. Chu, Simulation of injection mold filling of viscoelastic polymer with fountain flow, *AIChE Journal*, Vol. 34, No. 1, 1988, p. 94-106.

- 
- [44] H. Mavridis, A. N. Hrymak and J. Vlachopoulos, The effect of fountain flow on molecular orientation in injection molding, *Journal of Rheology*, Vol. 32, No. 6, 1988, p. 639-663.
- [45] H. Mavridis, A. N. Hrymak and J. Vlachopoulos, Transient free surface flows in injection mold filling, *AIChE Journal*, Vol. 34, No. 3, 1988, p. 403-410.
- [46] K. K. Wang and V. W. Wang, Computer aided mold design and manufacturing, in *Injection and Compression Molding Fundamentals*, Marcel Dekker, Inc., New York, Chapter 9, 1987, p. 607-669.
- [47] H. P. Wang and H. S. Lee, Numerical techniques for free and moving boundary problems, in *Fundamentals of Computer Modeling for Polymer Processing*, Hanser Publishers, Munich, Chapter 8, 1989, p. 340-401.
- [48] P. Kennedy, *Flow Analysis of Injection Molds*, Hanser Publishers, Munich, 1995.
- [49] S. I. Güçeri, Finite difference solution of field problem, in *Fundamentals of Computer Modeling for Polymer Processing*, Hanser Publishers, Munich, Chapter 5, 1989, p. 141-236.
- [50] S. Subbiah, D. L. Trafford and S. I. Güçeri, Non-isothermal flow of polymers into two-dimensional, thin cavity molds: A numerical grid generation approach, *International Journal of Heat and Mass Transfer*, Vol. 32, No. 3, 1989, p. 415-434.
- [51] A. Couniot and M. J. Crochet, Finite elements for the numerical simulation of injection molding, *Proceedings of The 2<sup>nd</sup> International Conference on Numerical Methods in Industrial Forming Processes (Numiform'86)*, Balkema Publishers, Rotterdam, 1986, p. 165-170.
- [52] A. Couniot, *Développement d'un Algorithme de Remaillage Automatique pour la Simulation du Moulage par Injection*, PhD Thesis, Université catholique de Louvain, Louvain-la-Neuve, 1991.
- [53] F. Dupret, A. Couniot, O. Mal, L. Vanderschuren and O. Verhoyen, Modeling and simulation of injection molding, in *Advances in the Flow and Rheology of Non-Newtonian Fluids*, Elsevier, Amsterdam, Chapter 7, 1999, p. 939-1010.

- [54] J. F. Hétu, D. M. Gao, A. Garcia-Rejon and G. Salloum, 3D finite element method for the simulation of the filling stage in injection molding, *Polymer Engineering and Science*, Vol. 38, No. 2, 1998, p.223-236.
- [55] E. Pichelin and T. Coupez, Finite element solution of the 3D mold filling problem for viscous incompressible fluid, *Computer Methods in Applied Mechanics and Engineering*, Vol. 163, No. 1, 1998, p. 359-371.
- [56] G. A. A. V. Haagh and F. N. van de Vosse, Simulation of three-dimensional polymer mould filling process using a pseudo-concentration method, *International Journal for Numerical Methods in Fluids*, Vol. 28, No. 9, 1998, p. 1355-1369.
- [57] G. A. A. V. Haagh, G. W. M. Peters, F. N. van de Vosse and H. E. H. Meijer, A 3-D finite element model for gas-assisted injection molding: Simulations and experiments, *Polymer Engineering and Science*, Vol. 41, No. 3, 2001, p. 449-465.
- [58] E. Broyer and C. W. Macosko, Heat transfer and curing in polymer reaction molding, *AIChE Journal*, Vol. 22, No. 2, 1976, p. 268-276.
- [59] L. J. Lee and C. W. Macosko, Heat transfer in polymer reaction injection molding, *International Journal of Heat and Mass Transfer*, Vol. 23, No. 11, 1980, p. 1479-1492.
- [60] Z. Tadmor, C. G. Gogos, *Principles of Polymer Processing*, John Wiley & Sons, Ltd., New York, 1979.
- [61] J. D. Domine and C. G. Gogos, Simulation of reactive injection molding, *Polymer Engineering and Science*, Vol. 20, No. 13, 1987, p. 847-858.
- [62] C. N. Lekakou and S. M. Richardson, Simulation of reacting flow during filling in reaction injection moulding (RIM), *Polymer Engineering and Science*, Vol. 26, No. 18, 1986, p. 1264-1275.
- [63] I. Manas-Zloczower, J. W. Blake and C. W. Macosko, Space-time distribution in filling a mold, *Polymer Engineering and Science*, Vol. 27, No. 16, 1987, p. 1229-1235.

- [64] M. R. Kamal and M. E. Ryan, Thermoset Injection Molding, in *Injection and Compression Molding Fundamentals*, Marcel Dekker, Inc., New York, Chapter 9, 1987, p. 329-376.
- [65] C. D. Lack and C. A. Silebi, Numerical simulation of reactive injection molding in a radial flow geometry, *Polymer Engineering and Science*, Vol. 28, No. 7, 1988, p. 434-443.
- [66] D. S. Kim and S. C. Kim, Rubber modified resin. III: Reaction injection molding process, *Polymer Engineering and Science*, Vol. 35, No. 7, 1995, p. 564-576.
- [67] M. A. Garcia, C. W. Macosko, S. Subbiah and S. I. Güçeri, Modelling of reactive filling in complex cavities, *International Polymer Processing*, Vol. 6, No. 1, 1991, p. 73-82.
- [68] R. E. Hayes, H. H. Dannelongue and P. A. Tanguy, Numerical simulation of mold filling in reaction injection molding, *Polymer Engineering and Science*, Vol. 31, No. 11, 1991, p. 842-848.
- [69] R.-Y. Chang and C.-H. Chen, Simulation of filling and curing processes in epoxy reactive molding, *Journal of the Chinese Institute of Chemical Engineers*, Vol. 26, No. 3, 1995, p. 183-194.
- [70] G. A. A. V. Haagh, G. W. M. Peters and H. E. H. Meijer, Reaction injection molding: Analyzing the filling stage of a complex product with a highly viscous thermoset, *Polymer Engineering and Science*, Vol. 26, No. 20, 1996, p. 2579-2588.
- [71] D. Seo, J. R. Youn and C. L. Tucker, Numerical simulation of mold filling in foam reaction injection molding, *International Journal for Numerical Methods in Fluids*, Vol. 42, No. 10, 2003, p. 1105-1134.
- [72] Y.-W. Lo, D. D. Reible, J. R. Collier and C.-H. Chen, Three-dimensional modeling of reaction injection molding. I, *Polymer Engineering and Science*, Vol. 34, No. 18, 1994, p. 1393-1400.
- [73] Y.-W. Lo, D. D. Reible, J. R. Collier and C.-H. Chen, Three-dimensional modeling of reaction injection molding. II: Application, *Polymer Engineering and Science*, Vol. 34, No. 18, 1994, p. 1401-1405.

- [74] R.-Y. Chang, C.-C. Hung and W.-H. Yang, Three-dimensional CAE Analysis of underfill flow of flip-chips, *ANTEC 2002 Proceedings*, May 2002, p. 588-592.
- [75] R. Sekula, P. Saj, T. Nowak, K. Kaczmarek, K. Forsman, A. Rautiainen and J. Grindling, 3-D modeling reactive molding processes: From tool development to industrial application, *Advances in Polymer Technology*, Vol. 22, No. 1, 2003, p. 42-55.
- [76] D. Seo and J. R. Youn, Numerical analysis on reaction injection molding of polyurethane foam by using a finite volume method, *Polymer*, Vol. 46, No. 17, 2005, p. 6482-6493.
- [77] Y. K. Shen, S. H. Chen and H. C. Lee, Analysis of the mold filling process on flip chip package, *Journal of Reinforced Plastics and Composites*, Vol. 23, No. 4, 2004, p. 407-428.
- [78] R.-Y. Chang, W.-H. Yang, S.-J. Hwang and F. Su, Three-dimensional modeling of mold filling in microelectronics encapsulation process, *IEEE Transactions on Components and Packaging Technologies*, Vol. 27, No. 1, 2004, p. 200-209.
- [79] C. v. L. Kietzmann, J. P. Van Der Walt and Y. S. Morsi, A free-front tracking algorithm for a control-volume-based Hele-Shaw method, *International Journal for Numerical Methods in Engineering*, Vol. 41, No. 2, 1998, p. 253-269.
- [80] J. M. Castro, M. Cabrera Ríos and C. A. Mount-Campbell, Modelling and simulation in reactive polymer processing, *Modelling and Simulations in Materials Science and Engineering*, Vol. 12, No. 3, 2004, p. S121-S149.
- [81] A. H. Haidari and B. Matthews, Future trends for computational fluid dynamics in the process industry, Third International Conference on CFD in the Minerals and Process Industries, Melbourne, Australia, December 2003, p. 331-338.
- [82] Wikipedia contributors, Moore's Law, *Wikipedia, The Free Encyclopedia*, October 7<sup>th</sup> 2006.  
([http://en.wikipedia.org/w/index.php?title=Moore%27s\\_Law&oldid=80010669](http://en.wikipedia.org/w/index.php?title=Moore%27s_Law&oldid=80010669))
- [83] ANSYS, Inc., *CFX-5 Version 5.6 Documentation*, 2003.



- 
- [84] O. Ubbink, *Numerical Prediction of Two Fluid Systems with Sharp Interfaces*, PhD Thesis, Dep. of Mech. Engineering, Imperial College of Science, Technology and Medicine, London, January 1997.
- [85] P. J. Zwart, M. Scheuerer and M. Bogner, Free surface flow modelling of an impinging jet, ASTAR International Workshop on Advanced Numerical Methods for Multidimensional Simulation of Two-Phase Flow, Garching, Germany, September 2003, p. 1-12.
- [86] ANSYS Canada Ltd, *CFX-5 Supplementary Theory*, 2004.
- [87] AEA Technology Engineering Software, Ltd., *CFX-TASCFlow Computational Fluid Dynamics Software Version 2.12 Theory Documentation*, 2002.
- [88] T. J. Barth and D. C. Jespersen, The design and application of upwind schemes on unstructured meshes, *AIAA Paper* 89-0366, 1989.
- [89] F. M. White, *Fluid Mechanics – 2<sup>nd</sup> Ed.*, McGraw-Hill International Editions, Singapore, 1988.
- [90] T. Franck, Advances in computational fluid dynamics (CFD) of 3-dimensional gas-liquid multiphase flows, NAFEMS Seminar: Simulation of Complex Flows (CFD) – Applications and Trends, Wiesbaden, Germany, April 2005, p. 1-18.
- [91] A. Burns, A. Splawski, S. Lo and C. Guetari, Application of coupled solver technology to CFD modelling of multiphase flows with CFX, First International Conference on Computational Methods in Multiphase Flow, Orlando, U.S.A, March 2001.
- [92] ANSYS, Inc., *CFX-5 Version 5.7 Documentation*, 2004.
- [93] ANSYS, Inc., *ANSYS CFX Release 10.0 Documentation*, 2005.
- [94] M. R. Kamal, S. Sourour and M. Ryan, Integrated thermo-rheological analysis of the cure of thermosets, *SPE Technical Paper*, 19, 1973, p. 187-191.
- [95] S. V. Patankar, *Numerical Heat Transfer and Fluid Flow*, Taylor & Francis, Philadelphia, 1980.

- [96] F. R. Menter, P. F. Galpin, T. Esch, M. Kuntz and C. Berner, CFD simulations of aerodynamic flows with a pressure-based method, 24<sup>th</sup> International Congress of the Aeronautical Sciences (ICAS 2004), Yokohama, Japan, August-September 2004.
- [97] S. R. Estevez and J. M. Castro, Applications of a reaction injection molding process in the analysis of premature gelling, demold time and maximum temperature rise, *Polymer Engineering and Science*, Vol. 24, No. 6, 1984, p. 428-434.
- [98] J. M. Castro and C. W. Macosko, Reaction injection molding, in *Encyclopedia of Materials Science and Engineering*, Vol. 6, Pergamon Press, Oxford, 1986, p. 4085-4090.
- [99] R.-Y. Chang and W.-H. Yang, Numerical simulation of mold filling in injection molding using a three-dimension finite volume approach, *International Journal for Numerical Methods in Fluids*, Vol. 37, No. 2, 2001, p. 125-148.